Numerical Study of Current Collection by an Orbiting Bare Tether

by

Tatsuo Onishi

Submitted to the Department of Aeronautics and Astronautics
in partial fulfillment of the requirements for the degree of
Doctor of Philosophy in Aeronautics and Astronautics
at the
MASSACHUSETTS INSTITUTE OF TECHNOLOGY
August 2002

Author .....
Department of Aeronautics and Astronautics
August, 2002

Certified by ..
Professor Manuel Martínez-Sánchez, Thesis Supervisor
Department of Aeronautics and Astronautics

Certified by .....
Professor Daniel E. Hastings, Thesis Committee Member
Department of Aeronautics and Astronautics

Certified by .....
Dr. David L. Cooke, Thesis Committee Member
Air Force Research Laboratory

Certified by ...
Professor Karen K. Gleason, Thesis Committee Member
Department of Chemical Engineering

Accepted by ...
Edward M. Greitzer
Professor of Aeronautics and Astronautics
Chairman, Department Committee on Graduate Students

Numerical Study of Current Collection by an Orbiting Bare Tether

by

Tatsuo Onishi

Submitted to the Department of Aeronautics and Astronautics
on August, 2002, in partial fulfillment of the
requirements for the degree of
Doctor of Philosophy in Aeronautics and Astronautics

Abstract

An electrodynamic (ED) Tether is a long thin conductive string deployed from a spacecraft. A part of the ED tether near one end is rendered positive with respect to the ambient plasma. This positive potential is maintained by the motion-induced Electromotive Force (EMF) or by the power supply, depending on the application of the ED tether. Some part of the positively biased tether is uninsulated and exposed to the ambient plasma, collecting ionospheric electrons. Collected electrons are driven as a current inside the tether and emitted from the other end. The current interacts with the geomagnetic field and produces Lorentz force (forward or backward). Drag force is obtained by deploying the tether upwards and collecting electrons through the part near the top end. Thrust is instead obtained by deploying downwards, applying a power supply to reverse the current and collecting electrons at the bottom end.

An ED tether travels in LEO under mesothermal conditions, meaning that the electron thermal velocity is much faster than the tether's orbital speed whereas the ion thermal velocity is much slower. In the frame of reference moving with the tether, ions approach the tether at hypersonic speed, get deflected by the very large positive potential on the tether and create a wake behind it. Due to the asymmetry of the plasma distribution, the conventional probe theory becomes almost inapplicable. The asymmetric and non-stable plasma conditions entail the necessity of computational work for the prediction of current collection.

A numerical code using a Particle-In-Cell (PIC) method is developed to calculate the electron current collection to a positively charged electrodynamic bare tether. In order to improve the quantitative accuracy, a new treatment of boundary condition, which utilizes the quasi-neutrality condition of plasma, has been introduced. This condition has been tested and shown elsewhere to give a good quantitative approximation to a current collection calculation to a cylindrical probe in a quiescent unmagnetized plasma. In this thesis, the flowing and magnetic effects as seen in the actual plasma environment are incorporated.

Calculations for a list of cases with different plasma parameters are performed and compiled so as to provide the pre-flight prediction of the NASA space experiment

called ProSEDS, which is planned to be launched Fall 2002. There is an existing theory called the Orbital-Motion-Limit (OML) theory, which gives the upper limit of the current collection in steady state. The results show that the current collection is higher in some cases than the 2D OML current by a factor of 2 - 3. We discuss the applicability of the 3D OML theory, which gives a higher limit, to the geometrically 2D problem. The justification is given by the detailed examination of individual particle trajectories.

Thesis Supervisor: Manuel Martínez-Sánchez
Title: Professor of Aeronautics and Astronautics

Acknowledgments

I can not think of my 6-year stay at MIT without thinking of so many precious faces. When I stepped out of the international flight from Japan, there was nobody I knew. I was totally alone. I could not even speak a decent English.

I would like to thank, first of all, H. Sanith Wijesinghe who took away the solitude out of my life. His support and friendship literally define the words. My survival at MIT would not have been possible without him. I also would like to thank, Sean George and Alex Budge, for giving a warm welcome to this lonely quiet japanese student. Also I could not talk about my first year without mentioning Salma Qarnain who kindly helped me get around the lab. explained me about computers with the never-fading smile. Ryoji Hayashi is my big brother in the first year. I appreciated and enjoyed his company in the life of Tang Hall.

After my first year at MIT, I started to realize that I was in the middle of so many wonderful people. I would like to thank Tolulope Okusanya for creating a social life at MIT and making me realize the beauty of my own language. He is also my sensei of UNIX. Whenever I had a problem, he was always willing to help me. I can not talk about my computer life without thanking Andjelka Kelic who always gave me a solution. Cyrus Jilla always talked with me in a comfortable and relaxing way. I remember that he is actually the very first person I talked with in the Aero/Astro department. He was very nice to this strange japanese guy.

It is not an exaggeration to say that my life at MIT started in pool. I would like to thank my personal mentor and swimming buddy, Richard Garnar, for the daily conversation of plasma physics at the pool side and in the shower. He gave me a lot of insight to the subject and showed me how to swim a life. I also thank Markus Palenberg for introducing me into an european life. He not only introduced me a better life but also gave me a chance to enjoy the Wednesday Night Dinner. I really enjoyed The Wednesday Night Dinner and loved all the "core members". I have learned a new life at the Wednesday Night Dinner.

Working on such an interesting but complicate problem of an electrodynamic

tether, many people have helped me and guided me toward the right path. I would like to thank Prof. Juan Sanmartín for guiding me through the bellezza of probe theory. I would also like to thank Dr. David Cooke for supporting me all through six years. I would like to thank Prof. Karen Gleason and Prof. Daniel Hastings for their valuable discussion and guidance of my research.

My working environment could not have been better. I was very fortune to have really great officemates and colleaques. I would like to thank Oleg Batishchev for his personal support and knowlegdes on plasma physics that he shared with us, Anne Pacros for creating a chearful atmosphere in the lab., Luis Fernando Velasques for his not-so-obvious but considerable supports, Shannon Cheng for a lovely existence herself, Murat Çelik for heated good conversations, Núria Margarit for bringing a smile everywhere she goes, Mark Santi for showing me the italian spirit in the american way, and Jean-Benoît Ferry for giving me a lot of help in my research when I needed them most.

I believe that the last few years, my office 37-438 was the nicest, most friendly and brightest windowless office at MIT. I was extremely lucky to get Jorge Carretero, Vincent Blateau and Paulo Lozano as my officemates. And of course Marcela Shulz. I would like to thank Jorge Carretero for creating the lab. so comfy. It was always a great pleasure to find him in the office and to have a lot of "fun" created by him. I would like to thank Vincent Blateau for getting everybody together. He really helped our group be united. He also helped me very patiently in writing in french. Paulo Lozano and Marcela Shulz are really my big brother and sister. We did so many things together. We always laughed together. Paulo is really the man of SPL.

I would like here to thank my supervisor, Prof. Martínez-Sánchez, for everything he did to me. He gave a great chance to work on a very interesting but still untouched problem. He was very patient with me even when I did not make any progress at all for a long time. He supported me in a every single possible way. I believe that if he was not my advisor, I could not be here writing this thesis. My respect to him is eternal and my appreciation to him is astronomical.

My coming to USA was really hard for my parents. Born and grown up in Kyoto,

Japan, they could not understand why their son wanted to leave home and go to the other side of the Earth. I know that they did not want me to go. However, instead of talking me out of it, they smiled at me and told me to pursue my dream. I am a very happy son. I wish I could make them feel in the same way. Honmani Arigato, Oto-chan, Oka-chan.

Finalmente, vorrei ringrazare a mia moglie, Maria Carla Parrini. Tu mi hai trovato quando ero da solo. Tu mi hai portato una vita. Tu mi hai dato la ragione della vita. Non sono da solo di piú. Tu sei sempre con me. Io sono sempre con te. Non capiamoci ancora bene, pero ce la facciamo perché abiamo tanto tanto tempo insieme. Grazie tanto per essere accanto a me. La vita é proprio bella con te.

Contents

1 Background **21**

1.1 Electrodynamic Tether 21

1.1.1 Tether 21

1.1.2 Electrodynamic Tether (EDT) 21

1.2 How The Electrodynamic Tether Works 22

1.3 Real EDT in Space : TSS-1/R & ProSEDS 26

1.4 Current Collection in OML Regime 29

1.4.1 Langmuir and Mott-Smith 30

1.4.2 Laframboise and Parker 32

1.5 Engineering Problems and Scientific Significance 34

1.6 Conclusions of Background Section 36

2 Previous Research **39**

2.1 Introduction 39

2.2 Theoretical Works 39

2.2.1 Mott-Smith & Langmuir (1926)
Orbital Motion Limited (OML) current : Unmagnetized plasma 40

2.2.2 Laframboise & Parker (1973)
OML current without the conservation of angular momentum 40

2.2.3 Sanmartín and Estes (1999) 42

2.2.4 Parker-Murphy theory (1967): Magnetized Plasma 45

2.2.5 Laframboise & Rubinstein (1976,1978,1983)
Infinite cylindrical and spherical probes in magnetoplasma . . 48

2.2.6 Laframboise (1997)
After TSS-1/R : Magnetic presheath 50
2.2.7 Cooke & Katz (1994,1998):
Plasma heating in the presheath 53
2.3 Experimental Works 54
2.3.1 Gilchrist and Bilén:
Electron current collection by Bare EDT (Ground Experiment) 55
2.3.2 Tether Space Experiments 56
2.4 Computational Works 58
2.4.1 Laframboise (1966) 58
2.4.2 Godard & Laframboise (1975,1983) 60
2.4.3 Usui (1993) 60
2.4.4 Onishi (1998) 60
2.5 Conclusions on Previous Works 62

3 Computations **65**
3.1 Particle-In-Cell (PIC) method 65
3.2 Specifications of our models 68
3.2.1 Structured cylindrical grid 69
3.2.2 Large Square grid 70
3.2.3 Plasma parameters 70
3.2.4 Quasi-neutrality Condition 72
3.2.5 Application of the quasi-neutrality condition 73
3.2.6 Meso-thermal Condition 74
3.2.7 Incoming Electron Density, $n_e^{in}(\phi)$ 75
3.2.8 2D. vs 3D. 78
3.2.9 Criterion to use 3D injection at boundary 83
3.2.10 Transition between 2D and 3D 84
3.2.11 Incoming ion density 85
3.2.12 Outgoing particle density 86

3.2.13 Incoming Particle Fluxes 89
3.2.14 Trapped Electrons outside the Computational Domain 91
3.2.15 Analytical Move 92
3.2.16 Sub-Cycling 95

4 Results and Pre-Flight Predictions **97**

4.1 Quiescent Unmagnetized Plasma : Code Verification 97
4.2 Quiescent Magnetized Plasma 101
4.3 Flowing Unmagnetized Plasma 103
4.4 Flowing Magnetized Plasma 105
4.5 Results from Computations 108
4.5.1 Ion density 108
4.5.2 Electron density 110
4.5.3 Electric Charge Density 111
4.5.4 Electric Potential 113
4.5.5 Trapped Electrons and Non-trapped Electrons 114
4.5.6 Current Collection 116
4.5.7 Particle Motions 122
4.5.8 Plasma Oscillations 127
4.5.9 Frozen Case 130

5 Results and Pre-Flight Predictions II **135**

5.1 Current Collections 136
5.2 Case 1 : Magnetic Field ($B = 0.1(G)$) 137
5.3 Case 2 : Magnetic Field ($B = 0.6(G)$) 138
5.4 Case 3 : Tether Potential ($\phi_p = 10(V)$) 142
5.5 Case 4 : Tether Potential ($\phi_p = 100(V)$) 143
5.6 Case 5 : $\frac{\text{Tether Radius}}{\text{Debye Length}}$ ($\frac{d}{d_D} = 0.3$) 144
5.7 Case 6 : $\frac{\text{Tether Radius}}{\text{Debye Length}}$ ($\frac{d}{d_D} = 3$) 146
5.8 Case 7 : $\frac{\text{Tether Radius}}{\text{Debye Length}}$ ($\frac{d}{d_D} = 10$) 146
5.9 Case 8 : Electron Temperature ($T_e = 0.05(eV)$) 146

5.10 Case 9 : Electron Temperature ($T_e = 0.2(eV)$) 148
5.11 Case 10 : Ion Temperature ($T_i = 0.05(eV)$) 150
5.12 Case 11 : Ion Temperature ($T_i = 0.2(eV)$) 152
5.13 Case 12 : Tilted Tether ($\theta = 60(\text{deg})$) 153
5.14 Case 13 : Electron Temperature ($T_e = 0.05(eV)$) & Tether Potential ($\phi_p = 10(V)$) 155
5.15 Case 14 : Electron Temperature ($T_e = 0.2(eV)$) & Tether Potential ($\phi_p = 10(V)$) 156
5.16 Case 15 : $\frac{\text{Tether Radius}}{\text{Debye Length}}$ ($\frac{d}{d_D} = 0.1$) & Tether Potential ($\phi_p = 100(V)$) 157

6 Conclusions and Recommendations **165**
6.1 Summary and contributions 165
6.2 Recommendations 169

A Mott-Smith & Langmuir (1926) **173**

B Time-averaged Outside Boundary Conditions **179**

List of Figures

1-1 Spacecraft with an EDT 22

1-2 EMF on EDT 22

1-3 Potential different 23

1-4 Current on EDT 23

1-5 Power Generation 23

1-6 Potential diagram in the generator mode 24

1-7 Lorentz drag force 24

1-8 EDT in thruster mode 25

1-9 Reverse Current and Thrust 25

1-10 Potential diagram in the thruster mode 26

1-11 TSS-1/R vs. ProSEDS 27

1-12 Electron trajectories in Orbit-Motion-Limit (large sheath and/or small tether radius) and Langmuir Limit (small tether and/or large tether) 30

1-13 Effective potential and electron trajectories in and out of OML regime 32

1-14 Current density to the cylindrical probe as a function of Debye ratio. Solid line is the "exact solution" by *Laframboise* and dotted line is the OML current density. The bars represent PIC computational results [33]. 35

2-1 Region of integration for the calculation of current collection in (J, E) space. 43

2-2 Graphical criterion of potential profile for the OML current collection 44

2-3 Current $i = I/[r_p n_\infty \sqrt{2\pi\kappa T_e/m}]$ vs probe potential $\phi_p = e\phi_p/\kappa T_e$ for various values of $\beta = r_p/\bar{a} = r_p eB(2/\pi mkT)^{1/2}$ ($\bar{a}$ =mean gyroradius, r_p =probe radius) 49

2-4 Comparison of the *Rubinstein and Laframboise* [1982] (solid line) and *Parker and Murphy* [1967] canonical upper-bound values for dimensionless attracted-particle current I as a function of dimensionless probe potential ϕ_p, for various values of the dimensionless magnetic field strength β. The curve for $\beta = 0$ is the *Mott-Smith and Langmuir* [1926] orbit-limited current result [21]. 51

2-5 Magnetic presheath proposed by *Laframboise* [1997] 52

2-6 Plasma heating in the presheath due to the Bohm instability [2] . . . 53

2-7 Parker-Murphy current collection with heated presheath 54

2-8 Experimental Data and OML of Bare EDT's 56

2-9 Electron current collection to a cylindrical probe inside and outside of OML regime. Solid lines are Laframboise results for $T_e/T_i = 0$, 0.5 & 1.0. 59

2-10 Electron and Ion Flows 61

3-1 Momentum and total energy conserving algorithms 67

3-2 A typical cycle of PIC 68

3-3 Cylindrical structured computational grid for a quiescent unmagnetized plasma 69

3-4 Computational Grid. In the small window, an enlarged view of the grid near the tether is shown 71

3-5 Electrons in velocity space. Electrons with velocities inside indicated regions, cylinder (2D,left) and sphere (3D,right), are excluded in the calculation of the OML current. 77

3-6 Incoming electron density in 2D calculation 78

3-7 Incoming electron density in 3D calculation 79

3-8 Cylindrical tether, magnetic field and potential hump 80

3-9 Electron motion in a potential hump with magnetic field 81
3-10 Fixed potential hump and electron density 82
3-11 Conceptual picture at a boundary cell surface and outbound particles 87
3-12 Incoming electron flux in a nonmagnetized plasma (2-D) 90
3-13 Incoming electron flux in a magnetized plasma (3-D) 91
3-14 Numerical error near an ED tether 92
3-15 Error within one timestep 96

4-1 Current Collections in a quiescent unmagnetized plasma, Laframboise solutions (solid) and OML (dash) [33] 98
4-2 Current Collections in a quiescent unmagnetized plasma, Laframboise solutions (solid) and OML (dash) 99
4-3 Potential maps in and out of the OML regime in a quiescent unmagnetized plasma. r_p is the tether radius and d_D is the Debye length. All figures are shown to the same scale. $T_e = 100$ and $\phi_p = 25T_e$. 100
4-4 Potential Profiles with the abscissa as $(r_p/r)^2\phi_p$, where ϕ_p is a probe potential. Potential $\phi(r)$ should be over the diagonal line over all r. In a smaller window, an enlarged plot near the origin is shown. 101
4-5 Instantaneous field quantities in a flowing unmagnetized plasma: (Top Left) Trapped electron density, (Top Right) Free electron density, (Middle Left) Electron density, (Middle Right) Ion Density, (Bottom Left) Net Charge Density and (Bottom Right) Potential. 104
4-6 Current collection observed in computation. Trapped electrons contribute the excess current over the 2D OML. 105
4-7 Nominal Case : Ion density 109
4-8 Nominal Case : Electron density 110
4-9 Nominal Case : Net charge density 112
4-10 Nominal Case : Potential Field (V) 113
4-11 Trapped and Non-trapped Electron Density (Normalized by density at infinity n_∞) 114

4-12 Error in total energy 116
4-13 Nominal Case : Current Collection and 2D OML 117
4-14 Electrons in velocity space. Electrons with velocities inside indicated regions, cylinder (2D,left) and sphere (3D,right), are excluded in the calculation of the OML current. 118
4-15 Electrons in velocity space. Electrons with velocities inside indicated regions, cylinder (2D,left) and sphere (3D,right), are excluded in the calculation of the OML current. 120
4-16 OML current density with a transient potential $\Phi = \frac{e\phi_{2\sim3}}{\kappa T_e}$ for the nominal case, $\Phi_p = \frac{e\phi_p}{\kappa T_e} = 250$ $(T_e = 0.1(eV))$ 121
4-17 Typical "contained" electron trajectory and its variables history . . . 123
4-18 Gyrating electron approaches a potential hump 124
4-19 Electron "trapping" in a potential hump 125
4-20 Typical "non-trapped" electron trajectory and its variable history . . 126
4-21 Fast Fourier Analysis (FFT) of potential oscillations near the tether . 127
4-22 Typical "contained" electron trajectory and its variables history . . . 128
4-23 Magnitude of Electric Field 129
4-24 Current Collection with a frozen potential field 131
4-25 Typical "contained" electron trajectory and its variables history in a frozen case 132
4-26 Field quantities in the frozen case 133

5-1 Instantaneous maps of field quantities in Case 1 $(B = 0.1(G))$ 138
5-2 Electron trajectories and current collection in Case 1 $(B = 0.1(G))$ . . 139
5-3 Electron trajectories and current collection in Case 2 $(B = 0.6(G))$ . . 140
5-4 Instantaneous maps of field quantities in Case 2 $(B = 0.6(G))$ 141
5-5 Instantaneous maps of field quantities in Case 3 $(\phi_p = 10(V))$ 142
5-6 Electron trajectories and current collection in Case 3 $(\phi_p = 10(V))$ . . 143
5-7 Electron trajectory and current collection in Case 4 $(\phi_p = 100(V))$ . . 144
5-8 Instantaneous maps of field quantities in Case 4 145

5-9 Electron trajectories and current collection in Case 5 ($\frac{d}{d_D} = 0.3$) . . . 146
5-10 Instantaneous maps of field quantities in Case 5 ($\frac{d}{d_D} = 0.3$) 147
5-11 Instantaneous maps of field quantities in Case 6 ($\frac{d}{d_D} = 3$) 148
5-12 Current Collection in Case 6 ($\frac{d}{d_D} = 3$) 149
5-13 Instantaneous maps of field quantities in Case 8 ($T_e = 0.05(eV)$) . . . 150
5-14 Electron trajectories and current collection in Case 8 ($T_e = 0.05(eV)$) 151
5-15 Instantaneous maps of field quantities in Case 9 ($T_e = 0.2(eV)$) . . . 152
5-16 Electron trajectories and current collection in Case 9 ($T_e = 0.2(eV)$) . 153
5-17 Electron trajectories and current collection in Case 10 ($T_i = 0.05(eV)$) 153
5-18 Instantaneous maps of field quantities in Case 10 ($T_i = 0.05(eV)$) . . 154
5-19 Electron trajectories and current collection in Case 11 ($T_i = 0.2(eV)$) 155
5-20 Instantaneous maps of field quantities in Case 11 ($T_i = 0.2(eV)$) . . . 156
5-21 Electron trajectories and current collection in Case 12 ($\theta = 60(\text{deg})$) . 157
5-22 Instantaneous maps of field quantities in Case 12 ($\theta = 60(\text{deg})$) . . . 158
5-23 Electron trajectories and current collection in Case 13 ($T_e = 0.05(eV)$ & $\phi_p = 10(V)$) 159
5-24 Instantaneous maps of field quantities in Case 13 ($T_e = 0.05(eV)$ & $\phi_p = 10(V)$) 159
5-25 Electron trajectories and current collection in Case 14 ($T_e = 0.2(eV)\&\phi_p = 10(V)$) 160
5-26 Instantaneous maps of field quantities in Case 14 ($T_e = 0.2(eV)\&\phi_p = 10(V)$) 160
5-27 Instantaneous maps of field quantities in Case 15 ($\frac{d}{d_D} = 0.1\&\phi_p = 100(V)$) 161
5-28 Instantaneous maps of field quantities in later time in Case 15 ($\frac{d}{d_D} = 0.1\&\phi_p = 100(V)$) 162
5-29 Current collection in Case 15 ($\frac{d}{d_D} = 0.1\&\phi_p = 100(V)$) 163

List of Tables

1.1 Comparison between ProSEDS and TSS-1/R 29

2.1 Summary of known space tether missions [32] 57

3.1 Parameters 72

3.2 Numerical Parameters : a hat (ˆ) indicates a numerical parameter used in a computation 73

4.1 Plasma parameters for the nominal case 106

4.2 Other cases: plasma parameters to change from the nominal case . . 106

4.3 Combined cases 107

4.4 Parametric comparison : d is tether radius, d_D Debye length, r_L Larmor radius, ϕ_p tether potential, U_{tether} ion ram speed. 107

5.1 Current Collection in the comparison cases 136

Chapter 1

Background

1.1 Electrodynamic Tether

1.1.1 Tether

> teth.er \'teth-*r\ n 1: something (as a rope or chain) by which an animal is fastened so that it can range only within a set radius 2: the limit of one's strength or resources

A tether may look like a rope attached to a spacecraft. There may be a small satellite at the other end of the tether just like a leashed dog. There are many new ideas and applications of conducting- and non-conducting tethers proposed [1] in the research categories such as aerodynamics, transport system, controlled gravity, electrodynamics etc. In this thesis, we focus on electrodynamic tethers (EDTs) in an attempt to understand the interactions between EDTs and space plasmas.

1.1.2 Electrodynamic Tether (EDT)

When the tether is made of conducting material, it is called Electrodynamic Tether (EDT). Driving a current inside itself and traveling across the Geomagnetic field, EDT may be used to reboost/deboost a spacecraft to which the EDT is attached. This is made possible by the Lorentz force acting on the EDT. The mode of reboosting

a spacecraft is called "Thruster Mode" and the mode of deboosting is called "Power Generator Mode". In the latter mode, EDT is converting the spacecraft's orbiting kinetic energy into electric energy, that is, driving a current through the EDT. By placing a rechargeable battery at the end of the EDT, one can store electric energy in the battery while the spacecraft is being deboosted. More detailed accounts of the mechanism of an EDT is given in Section 1.2. In "Thruster Mode", a power supply is included in the system in order to reverse the current direction, thus redirecting the Lorentz force in the forward direction.

1.2 How The Electrodynamic Tether Works

The mechanism of the ED Tether is quite simple, but usually hard to understand at first sight. Let us see how an ED Tether works. An ED Tether has two modes of operation: power generation mode and thruster mode.

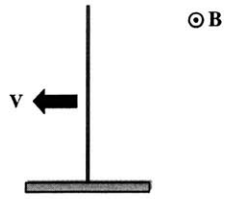

Figure 1-1: Spacecraft with an EDT

We discuss the power generation mode first, followed by the thruster mode. In Fig 1-1, a cartoon of a spacecraft and an ED tether deployed upwards is depicted. The tether is traveling to the left across the geomagnetic field whose vector points out of the page. Due to the relative motion to the magnetic field, an electromotive force (EMF) appears along the tether (Fig 1-2).

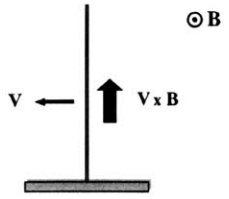

Figure 1-2: EMF on EDT

This EMF elevates the potential towards the upper end of the tether. In open circuit, the potential difference between the upper and lower ends is the EMF times the length of the tether, $l \cdot |\mathbf{V} \times \mathbf{B}|$.

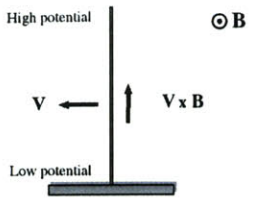

Figure 1-3: Potential different

In order to have a current flow inside the tether, an electron collector and an electron emitter are attached to the upper end and the lower end respectively (Fig 1-4). The electron emitter attached to the lower end through the spacecraft is used to control the on-board potential.

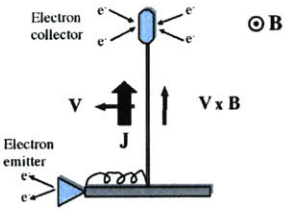

Figure 1-4: Current on EDT

This positive potential attracts and collects electrons from the ambient plasma through the collector. Collected electrons are driven as a current by the EMF inside the tether. By placing a rechargeable battery connected to the tether, we can recharge the battery, thus generating power (Fig. 1-5). In order to see the difference between a local potential on the tether and the local space potential, let us look at the tether and the space in the frame moving with the tether [6]. In the tether frame, the plasma at infinity has an electric field $\mathbf{V} \times \mathbf{B}$. If $\mathbf{V}$ is to the East and $\mathbf{B}$ to the North, $\mathbf{V} \times \mathbf{B}$ is upwards. Thus, the potential of the plasma, as seen from the tether, is falling at the rate $|\mathbf{V} \times \mathbf{B}|$ with distance z.

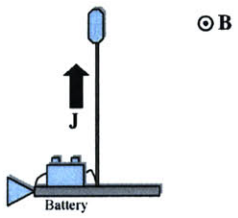

Figure 1-5: Power Generation

Now, suppose the tether is deployed upwards from a satellite, and the satellite is in good electrical contact with the local plasma. Suppose also that the top of the tether is somewhat positive with respect to its own local plasma (say $\sim 100V << L \cdot |\mathbf{V} \times \mathbf{B}|$),

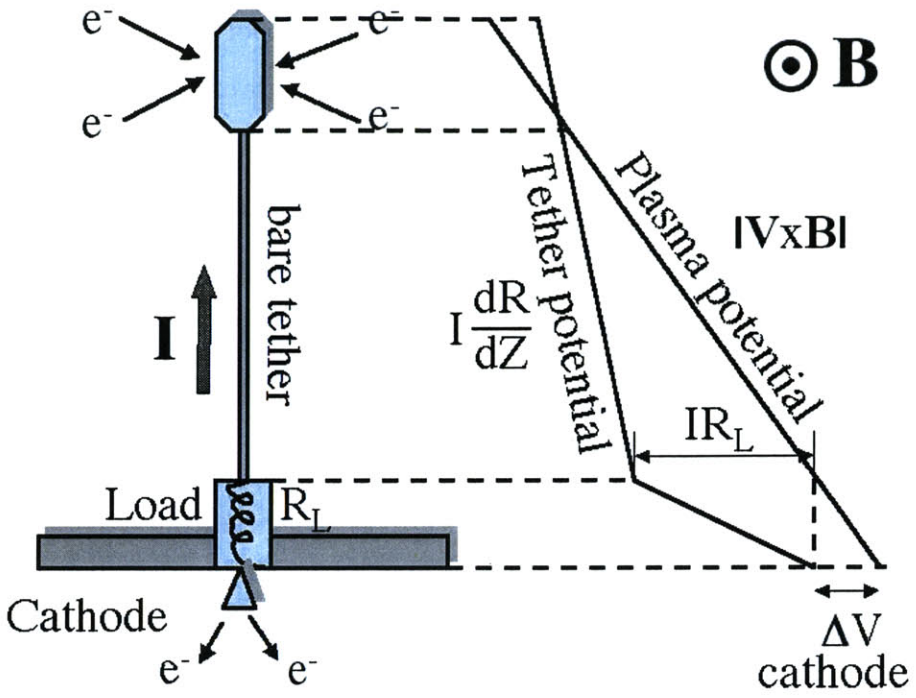

Figure 1-6: Potential diagram in the generator mode

where L is the tether length. This top portion collects ionospheric electrons, which flow down the tether. Their associated current, I, is then upwards, and since the tether has some finite resistance, the potential of the tether must be falling upwards at a rate $I\frac{dR}{dz}$. This fall rate should be less than the rate $|\mathbf{V} \times \mathbf{B}|$ at which the plasma potential is falling. At the satellite, there must be some sort of load, say a resistance R_L, in which the potential falls by IR_L.

If we represent positive potential to the right, this description is summarized in the potential diagram as in Fig. 1-6.

We cannot generate power out of nothing (Fig. 1.2). The current inside the tether and the geomagnetic field interact with each other and exert a Lorentz force in the opposite direction of motion, slowing down the tether and the spacecraft. In fact, the ED tether in power generation mode is converting spacecraft's kinetic energy into electric energy. The Lorentz

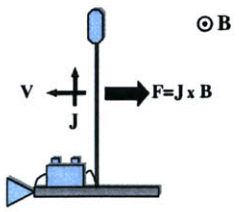

Figure 1-7: Lorentz drag force

force may be utilized to deorbit an expired spacecraft to the atmosphere where it burns out. In that case, power would probably be dissipated in a resister rather than stored.

Next, we look at the thruster mode of an ED tether. In thruster mode, the ED tether is deployed downwards (Fig. 1-8). As in the power generation mode, there is EMF along the tether. Instead of having current flow upwards, we place a power supply at the upper end and reverse the current flow. In order to maintain the current flow, an electron collector and an electron emitter via the power supply are attached at the lower end and the upper end, respectively.

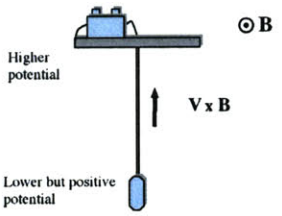

Figure 1-8: EDT in thruster mode

Again, the electron emitter can be manipulated to keep the lower end of the tether at positive potential, thus collecting electrons. Current created in such a way flows downwards in the tether and exerts Lorentz force, in interaction with the geomagnetic field, in the same direction as the tether's motion (Fig. 1-9). In practice, a battery recharged by solar panels, gives the power supply and an ED tether reboosts a spacecraft without expenditure of propellant. This fact is often referred to as propellantless propulsion by an ED tether.

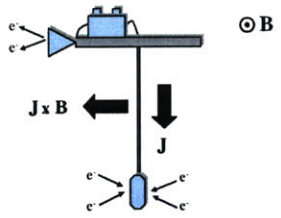

Figure 1-9: Reverse Current and Thrust

Let us see again the potential difference between the tether and the local plasma in the tether frame. The tether is now downwards and electrons are collected near the bottom. Thus the current is downwards, and so the tether potential increases with altitude z. Since the plasma potential still decreases with z as before, the tether-plasma bias is continuously higher as one climbs along the tether (unlike the generator case, where a cross-over point existed). Thus, all of the tether is positive with respect to the local plasma, and could be made to collect electrons. But those electrons collected near the satellite would do little work and dissipate a lot of power

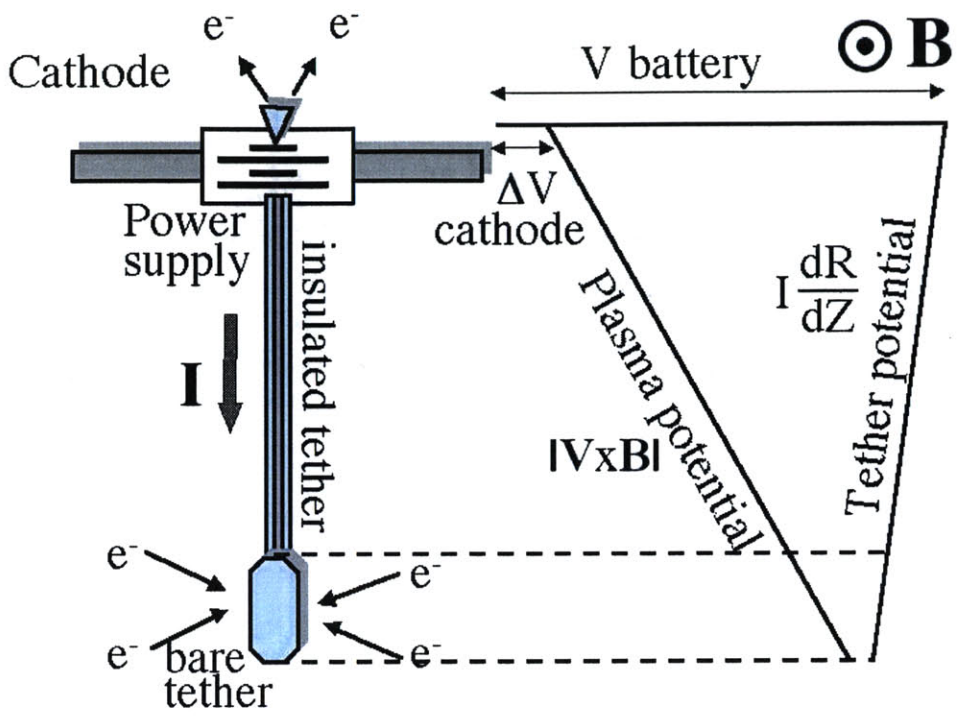

Figure 1-10: Potential diagram in the thruster mode

as they slam on the tether with high energy, so it may be best to insulate most of the tether and expose only some fraction near the bottom end. The potential diagram is now given in Fig 1-10.

1.3 Real EDT in Space : TSS-1/R & ProSEDS

In this section, we introduce two actual implementations of the EDT concept. The first one is the Tethered Satellited System 1 (TSS-1) and its reflight (TSS-1R) which actually flew in space and collected electrons from space. The second one is the Propulsive Small Expendable Deployer System (ProSEDS) which is planned to be launched in Fall 2002.

The difference in these ED tethers is the shapes of their electron collectors. TSS-1/R used a spherical body attached to the upper end of the tether to collect electrons. The tether was insulated and did not collect electrons (Fig. 1-11). The ED tether of

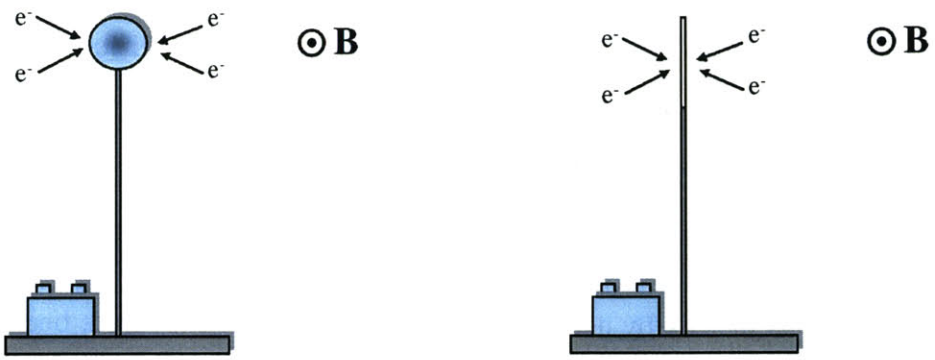

(a) TSS-1/R with a balloon collector

(b) ProSEDS with a cylindrical bare tether

Figure 1-11: TSS-1/R vs. ProSEDS

ProSEDS, on the other hand, does not have a large collector like TSS-1/R. It collects electrons by itself through the bare uninsulated part (Fig. 1-11).

The difference entails different applications of probe theory in the prediction of current-voltage characteristics. TSS-1/R used a big metallic sphere as a collector, whose diameter is much larger than the local Larmor radius of electrons. Therefore, magnetic effects have to be considered. Parker and Murphy applied canonical angular momentum and total energy conservations and derived the upper limit of current collection as a function of the tether potential in steady state. The derivation of Parker-Murphy theory is shown sec 2.2.4.

The results of the TSS-1/R space experiment revealed much higher current collection than that of Parker-Murphy theory, by a factor of $2 \sim 3$. Several researchers have attempted to understand the physics underlying the enhanced current collection. Some of their works are introduced in Chap. 2.

The physics involved in the current collection to a bare tether is somewhat different due to its size compared to the Larmor radius. The tether radius is typically of the same order of the Debye length which is about 7mm for the undisturbed density $n_\infty = 10^{11}[1/m^3]$ (2mm for $10^{12}[1/m^3]$), whereas the Larmor radius of an electron with the electron thermal velocity (for $T_e = 0.1(eV)$) is $2 \sim 3$ cm. The large ratio of Larmor radius to the tether radius renders magnetic field effects very weak. Without

magnetic effects, as the limiting case, the current collection depends on the ratio of the Debye length to the tether radius, Debye ratio. In addition, the fast motion of the tether across the ionospheric plasma introduces additional complexities, not easily understood using simple theory.

When the Debye ratio is small, that is, when the tether has a very thin sheath, some electrons just fly by near the tether without being captured, because the tether's potential is screened out and fails to deflect the electron. When the Debye length is large on the other hand,there is a thick sheath around the tether. Electrons do see the tether potential and are attracted by it, but if their angular momentum is too high, they may just fly by the tether and go away without being captured. The capture rate is then only limited by the dynamics of the orbital motion (the Orbital Motion Limit, or OML [18]). Clearly, this regime, where screening does not hinder collection, must yield the highest current possible for given density and tether size. In the next section 1.4, the OML theory is explained in more detail.

The Debye ratio seen in the case of the bare tether current collection is normally well inside the OML regime. OML can be thought of as the upper limit of current collection under steady state condition. Therefore we can expect the 2D OML current collection as the prediction of current collection to the ProSEDS ED tether. The advantage of the ProSEDS bare tether over the TSS-1/R is its efficiency. Since the ambient plasma density is so low, enlarging the contact area becomes necessary in order to collect enough current. In the case of a large metallic sphere as an electron collector as used in the TSS-1/R, Debye shielding makes the current collection ineffective,i.e. out of the OML regime. Moreover, the magnetic effects restrict the electron collection to essentially one dimensional. However, using the tether itself as an electron collector, one can exploit the effectiveness of the current collection in the OML regime and can enlarge the contact area by having a longer tether without leaving the regime [8].

In Table 1.1, the comparison between TSS-1/R and ProSEDS is recapitulated.

	ProSEDS	TSS-1/R
Collector	Cylindrical	Spherical
Pre-Flight Expectation	2D OML Thin cylinder	Parker-Murphy Large Sphere Magnetic Effects
Experimental Results		$2 \sim 3$ times higher than Parker-Murphy

Table 1.1: Comparison between ProSEDS and TSS-1/R

1.4 Current Collection in OML Regime

In this section, I explain the OML theory in two different ways. One is as done by Langmuir and Mott-Smith in their pioneering work [10] in the 1920's. Their approach is to look at the particle distributions at infinity, follow the particles' trajectories calculated from the energy conservation and the momentum conservation and then count particles which reach the surface of the tether. Although it is not necessary to use the angular momentum conservation in the derivation of OML current, the explanation of the OML current with these two conservations gives a good insight of the physics involved in the OML theory. On the negative side, this approach does not apply to non-symmetrical configurations, such as the tether plus a wake.

The other approach is the one done by Laframboise and Parker in 1973 [19]. Their approach is to start from the surface of the tether. They look at an electrons on the surface and reverse the trajectory in time. Then, the current is calculated by counting the electrons whose trajectories are traced back to the infinity.

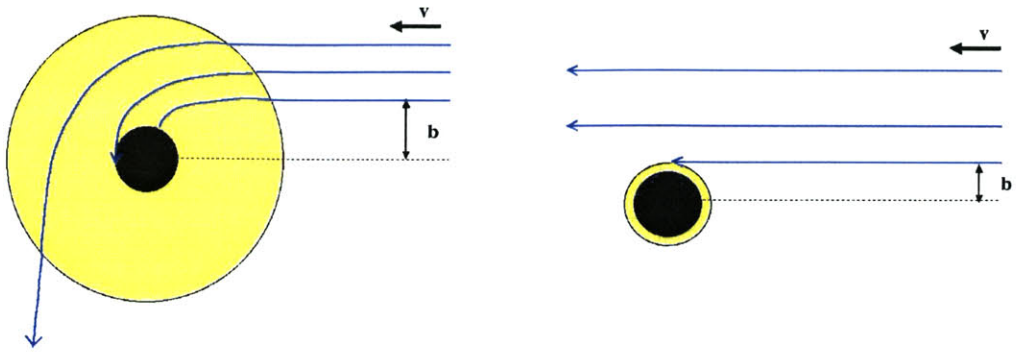

(a) Orbital-Motion-Limit : All electrons see the presence of the tether. Electrons with large angular momentum miss the tether and go away.

(b) Langmuir Limit : Due to the shielding of the tether, electrons do not see the presence of the tether and electron trajectories are straight.

Figure 1-12: Electron trajectories in Orbit-Motion-Limit (large sheath and/or small tether radius) and Langmuir Limit (small tether and/or large tether)

1.4.1 Langmuir and Mott-Smith

Current collection by spherical and cylindrical probes (tethers) was first analyzed by *Langmuir* and *Mott-Smith* [10] , who named the thin cylinder limit, 'Orbital Motion Limit (OML)'. When OML theory applies, namely, when the ratio of the probe (tether) radius to the Debye length of the plasma is so small that the shielding becomes unimportant, the number of electrons absorbed by the probe is determined from orbital consideration alone. In Figure 1-12, electron trajectories in two limits, OML and Langmuir Limit, are shown. Figure 1-12(a) shows the electron trajectories in OML. An electron sees the presence of the tether through potential field and its trajectory is deflected toward the tether as the electron approaches. Whether the electron is captured or not depends on its angular momentum. Figure 1-12(b) shows the electron trajectories in Langmuir Limit. Since the sheath is small and the tether is shielded, electrons do not see the presence of the tether. Therefore electrons trajectories are straight. Only electrons with the impact parameter, b, smaller than the tether radius are captured by the tether.

The OML limit can be described in terms of the effective potential [11]. Let J

and E be the angular momentum and the energy of an electron, respectively. From the energy conservation and the angular momentum conservation of an electron in two dimensions, although the velocity $w_{||}$ along the cylinder axis can be nonzero, we have

$$E = \frac{1}{2}m_e\left(w_r^2 + w_\theta^2\right) - e\phi \tag{1.1}$$

$$J = m_e r w_\theta \tag{1.2}$$

where r is the distance from the probe center, m_e the electron mass, $-e$ the electric charge of an electron, ϕ the local potential, w_r the radial velocity component, and w_θ the azimuthal velocity component. Substituting equation (1.2) into equation (1.1), we have

$$w_r^2 = \frac{2}{m_e}\left(E + e\phi - \frac{J^2}{2m_e r^2}\right). \tag{1.3}$$

In order for an electron to reach the surface of the probe, the right-hand side of equation (1.3) must be positive not only at the surface of the probe, but also all along the path from infinity to the surface. To consider the particle motion from the one dimensional viewpoint, the effective potential defined by

$$U = -e\phi + \frac{J^2}{2m_e r^2} \tag{1.4}$$

should be considered. Substituting the effective potential (1.4) into (1.3), we have

$$w_r^2 = \frac{2}{m_e}\left(E - U\right). \tag{1.5}$$

By taking the effective potential as a normal 1-D potential, we can treat the 2-dimensional electron motion as a 1-dimensional case. Figure 1-13 illustrates two limits regarding the effective potential. Assume that the probe is on the left of the figure. When the sheath is thin (Langmuir Limit), the second term of equation (1.4) becomes dominant near the probe and U has an intermediate maximum value. For some electrons, this bump in the effective potential works as a potential wall and

prevents them from reaching the surface unless they have enough energy to climb over the wall. When the sheath is thick (OML limit), the first term in equation

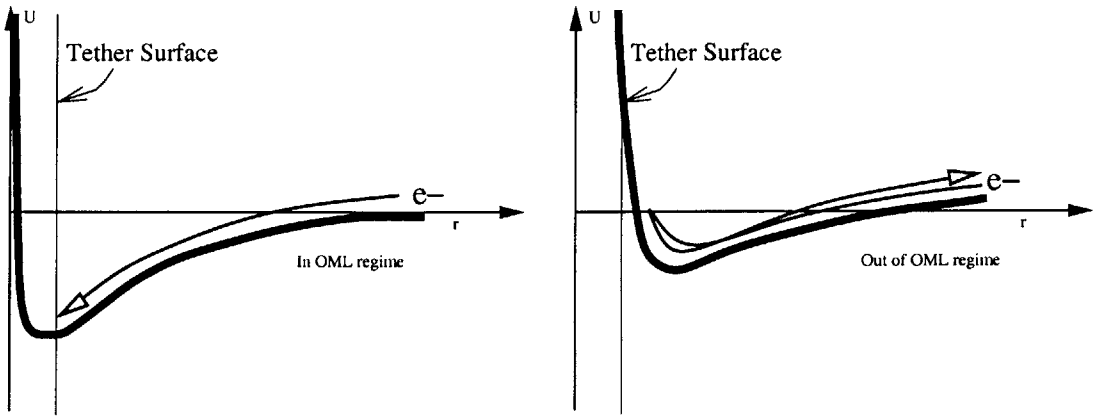

(a) Effective potential for small J and trajectory of a captured electron

(b) Effective potential for large J and trajectory of a "fly-by" electron

Figure 1-13: Effective potential and electron trajectories in and out of OML regime

(1.4) becomes dominant throughout the region, and the electric potential is large enough to shield out the angular momentum term in the effective potential In (a) of Figure 1-13, the angular momentum is so small or the potential is so large that all electrons fall into the potential well and are captured by the surface of the tether, where the effective potential is still negative. For a large angular momentum or a small potential, the angular momentum term in the effective potential becomes large. And the effective potential on the surface of the tether becomes positive. Therefore only electrons which have a kinetic energy in $r-$direction, $\frac{1}{2}m_e w_r^2$, more than the effective potential energy, eU(surface), are captured by the tether.

The derivation of the current collection in and near the OML regime by Langmuir and Mott-Smith is followed in Appendix A in a mathematically more detailed way.

1.4.2 Laframboise and Parker

Laframboise and Parker rephrased the definition of the OML current as follows; if the trajectories of all the electrons on the surface which have a total energy more than the potential energy difference between the surface and the infinity, can be traced

back to the infinity without being intercepted by the probe, the current collection to the surface is in the OML regime, giving rise to the highest current in steady state.

Let ϕ_p be the surface potential and the potential at infinity be zero, $\phi_\infty = 0$. The electrons which are energetically capable of traveling from the surface of the tether to infinity are characterized at the surface by

$$E = \frac{1}{2} m_e (w_r^2 + w_\theta^2) - e\phi_p \geq 0 \tag{1.6}$$

where $\vec{w} = (w_r, w_\theta)$ is the electron velocity. Note that equation (1.6) excludes some hypothetical electrons which have enough total energy $\frac{1}{2}m_e(w_r^2+w_\theta^2+w_z^2)-e\phi_p \geq 0$ but not enough total energy in the plane perpendicular to the tether, $\frac{1}{2}m_e(w_r^2+w_\theta^2)-e\phi_p$. In a two-dimensional problem, there is no mechanism that converts the kinetic energy in the direction parallel to the tether, $\frac{1}{2}m_e w_z^2$ to the perpendicular energy. Therefore, an electron which does not have a enough perpendicular total energy is not counted in the OML current calculation, whatever the value of w_z may be.

In the absence of collisions, the solution to Vlasov's equation must have the Maxwell-Boltzmann form for any velocity that does occur:

$$f_e(\vec{w}) = n_\infty \left(\frac{m_e}{2\pi k T_\infty} \right)^{3/2} \exp\left(- \frac{-e\phi_p + \frac{m_e}{2}\left(w_\perp^2 + w_\parallel^2\right)}{kT_\infty} \right) \tag{1.7}$$

where n_∞ is the density at infinity, k the Boltzmann constant, T_∞ the temperature at infinity and $w_\parallel$ a velocity component parallel to the cylindrical probe.

At the surface of the probe, only electrons which satisfy the equation (1.6) can exist and be counted for the current collection. The current density into the probe is given as, when $\frac{e\phi}{kT_\infty} >> 1$,

$$j = \frac{e n_\infty}{\pi} \sqrt{\frac{2e\phi_p}{m_e}} \tag{1.8}$$

which is independent of electron temperature, T_e. Note that equation (2.8) are independent of the shape of the cylinder's cross section (as long as OML conditions prevails). Also, for a given shape, the current density j is independent of location

within the surface.

When a three-dimensional problem is considered, the electrons counted in the calculation of the OML current collection are characterized by

$$\frac{1}{2}m_e(w_x^2 + w_y^2 + w_z^2) - e\phi_p \geq 0. \tag{1.9}$$

The 3D OML current is also calculated in the same manner as in the 2D case, and given as

$$\begin{aligned} j_{OML}(3D) &= \iiint_{w_x^2+w_y^2+w_z^2 \geq 2e\phi_p/m, w_\perp > 0} ew_\perp f_e d\mathbf{w} \\ &= en_\infty \sqrt{\frac{\kappa T_e}{2\pi m_e}} \left(1 + \frac{e\phi_p}{\kappa T_e}\right) \end{aligned} \tag{1.10}$$

OML limit is the upper limit under the consideration of energy conservation. All the energetically possible electrons at the probe surface are taken into account in the calculation. Therefore as long as an electron's total energy is conserved, the current density to the probe should be equal or less than the OML current density. The plot of current density vs. the radius-to-Debye ratio is shown in Fig 1-14.

Both calculations by *Laframboise and Parker* and *Langmuir and Mott-Smith* assumes operation in the OML regime. More detailed work which calculates the current collection in and out of the OML regime is done by *Sanmartín and Estes* [13] and presented in Chap.2.

1.5 Engineering Problems and Scientific Significance

In order to design an ED Tether as a thruster or a power generator, we need to know how much current we can get from the EDT system, because the force (Thrust/Drag) is proportional to the current. As a prediction of the current-voltage characteristics of ProSEDS bare ED tether, we mentioned the 2D OML current. However, as the

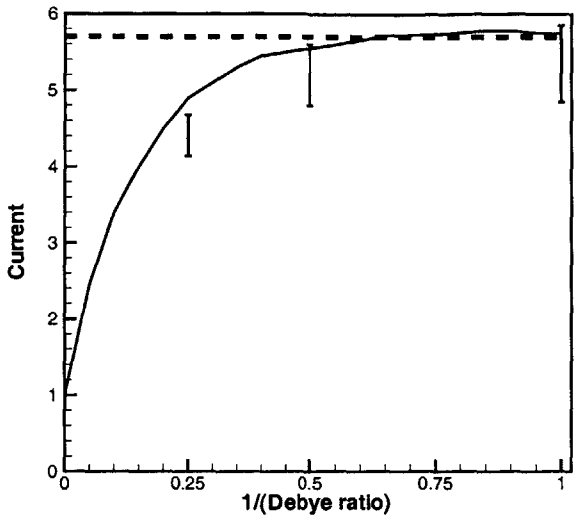

Figure 1-14: Current density to the cylindrical probe as a function of Debye ratio. Solid line is the "exact solution" by *Laframboise* and dotted line is the OML current density. The bars represent PIC computational results [33].

Parker-Murphy upper bound was exceeded in the TSS-1/R space experiment, it is quite possible that the 2D OML theory may be violated and the tether may collect more current. This thesis is aimed at providing the preflight predictions of ProSEDS space experiment by performing computer simulations using a Particle-In-Cell (PIC) method.

This work is also aimed at a new and tough problem in Langmuir-probe theory. Cylindrical probes have been used in space for many years for plasma measurements. Probe bias, however, is usually kept negative, or at most weakly positive, as the plasma properties such as density and temperature can be measured in the low voltage range with a small collected ion current. In this work, a cylindrical probe (ED tether) is place in a space plasma with a highly positive bias. The consequence of such a highly positive bias is the following; hypersonic ion flow breaks the symmetry of the ion distribution and creates an ion "caustic" line and a wake, which also changes the electron distribution. As for electrons, in the case of a negatively biased probe, the magnetic field does not modify the equilibrium of a gas because almost the full

Maxwellian distribution is populated. This is not the case for the highly positive bias. This work is believed to be the first numerical and theoretical work on a highly positive cylindrical probe in space.

In Chapter 2, relevant previous work is introduced. In Chapter 3, the numerical method (PIC) and the techniques used in simulations are explained. In Chapters 4 and 5, results from simulations are presented. In the simulations, a set of plasma parameters is chosen as a nominal case and several other cases with different parameters are computed in order to see the effect of the changed parameter. In Chapter 6, we discuss the results. The prediction of current collection in the ProSEDS experiment is given. In the final Chapter, conclusion and suggestions for future work are listed.

1.6 Conclusions of Background Section

Electrodynamic Tethers are considered to be a high-efficient, budget-saving alternative propulsion system for station-keeping, orbit-raising or de-orbiting purposes. In theory, we don't need any fuel which would be necessary for a conventional chemical or electric propulsion device. And we can consequently save several shuttle flights to refill the fuel (at least in comparison to chemical propulsion), which would save a lot of money.

The concept of the EDT is based on the utilization of the orbital velocity of a spacecraft and the Geomagnetic field. The cross product of the velocity of the spacecraft, v and the magnetic field, B, generates an electromotive force, E_{emf}, along the EDT, giving rise to a potential difference between the two ends. One end of the tether is somehow kept at a positive potential, either by the motion-induced EMF or by the power supply. By placing an electron collector at the end of positive potential, the EDT can collect electrons and the EMF drives them down to the spacecraft as a current. We can recharge a battery using this current. However, the current interacts with the Geomagnetic field and generates the Lorentz Force. This Lorentz Force acts as a drag to slow down the spacecraft. In short, the EDT is converting the spacecraft orbital energy into electrical energy. This is the Power Generation Mode of EDTs.

In order to put into practice the EDT technology, we still need to solve several problems. One of them is the Current-Voltage characteristic of an electron collector. There exist some theories. When the radius of the electron collector is comparable to or smaller than the local Debye length, current collection is limited by the Orbital-Motion-Limit (OML). OML is the upper limit of the current collection in the steady collisionless uniform plasma. When the radius of the electron collector is much larger than the electron gyroradius, current collection is under the effects of the magnetic field. Parker-Murphy theory provides the canonical upper limit in such a situation. TSS-1/R operated in this regime.

Sanmartín, Martínez-Sánchez and Ahedo [8] proposed a bare EDT, which collects electrons on a part of the EDT itself without a big spherical collector as used in TSS-1/R. The idea is based on the fact that among two upper limits associated with a large radius and a small radius of collectors, OML is more efficient than the P-M limit. The radius of a typical EDT is of the order of a few mm, which is about the same as the Debye length in the ionosphere where EDTs are applied. It is therefore in the OML regime.

The calculation of Current-Voltage characteristics of a Bare EDT does not seem straightforward, as the results of TSS-1R imply. The steady-state analysis with no magnetic field would lead to the upper limit of the OML. However, as observed in the TSS-1R experiment (a spherical collector), enhanced current collection may be possible even in the case of a cylindrical collector (a bare EDT). The OML theory is for a non-flowing, non-magnetized plasma, whereas in the ionosphere, the bare EDT will experience both flowing and magnetic effects. These effects make the analytical prediction very difficult, and the OML theory is good only for an order-of-magnitude estimate. The purpose of my work is to find out the C-V characteristics of a Bare EDT under flowing and magnetic effects, and understand the underlying physics with the help of computer simulations.

Chapter 2

Previous Research

2.1 Introduction

This chapter deals with the history of Electrodynamic Tethers (EDTs) in a more physically and mathematically correct manner than Chapter 1. First we introduce theoretical works which are related to the current collection by probes in a collisionless plasma. Some of them were done as early as the 1920's. The next section deals with experimental works both in space and in laboratory. The final section in this chapter deals with previous computational works on the electron current collection by EDTs, or more generally on Langmuir Probe current collection.

2.2 Theoretical Works

In this section, I pick up some of the important works in the history and discuss their relevance to EDT technology.

Theories for current collection by a cylindrical or a spherical probe are still incomplete. Especially when magnetic effects, with or without plasma flow, are present, the problem becomes very involved and formidable. *Sanmartín*[14] and *Laframboise and Sonmor* [21] did a very good job in reviewing older theories. In what follows, I will write a brief summary of Langmuir probe theory with some derivations of fundamental formulae such as the OML and Parker-Murphy.

2.2.1 Mott-Smith & Langmuir (1926) Orbital Motion Limited (OML) current : Unmagnetized plasma

We can call the work by *Langmuir et al* [10] the pioneer of Langmuir Probe Theory as the choice of name indicates. Considering its historical importance, I follow what they did in their paper in Appendix A. In the paper "The theory of collectors in gaseous discharge"(1926, Physical Review) [10], *Langmuir and Mott-Smith* derived general formulae for the current collection by spherical and cylindrical probes. They applied two equations of conservation, namely energy conservation and angular momentum conservation. It is assumed that the potential field is symmetric, i.e. $\phi = \phi(r)$. Those equations are applied at points at $r = r$ (on the surface of a probe) and $r = a$, which is the "edge" of the sheath, outside of which the plasma is totally undisturbed. Since the presheath where the quasi-neutrality prevails but the plasma potential is different from that at infinity extends practically to infinity, the limit of $a \to \infty$ was taken to get general formulae.

2.2.2 Laframboise & Parker (1973) OML current without the conservation of angular momentum

In 1973, *Laframboise & Parker* [19] derive the OML, equations (2.3) and (2.4) or identically equations (A.28) and (A.30), without using the conservation of angular momentum. Their argument is the following. In a steady uniform plasma, collisionless orbits, if traced back to ∞, connect to a uniform isotropic velocity distribution there (mostly Maxwellian) and hence their direction is unimportant. Since they retain their local energy, we therefore know the velocity distribution at points on these orbits. This argument yields the result that in the OML regime, i.e. when all orbits from a probe can be traced back to ∞, we know the distribution function on the probe. The only requirement is that all positive energy orbits actually connect to ∞,

which they fail to do if the sheath is thin.

When the distribution at ∞ is Maxwellian, the distribution on the probe which has positive charge ϕ_p, is also Maxwellian except that particles corresponding to negative total energy $\frac{1}{2}m_e w^2 + q\phi_p < 0$ are excluded. The current density into the probe is given as,

$$
\begin{aligned}
j &= e\iiint_{\frac{1}{2}m_e w_\perp^2 - e\phi_p \geq 0} w_\perp \cos\theta f_e d\mathbf{w} && (2.1)\\
&= e\int_{-\infty}^{\infty} dw_{\|} \int_{\sqrt{2e\phi_p/m_e}}^{\infty} \int_{-\pi/2}^{\pi/2} w_\perp f_e w_\perp \cos^2\theta d\theta dw_\perp && (2.2)\\
&= \frac{en_\infty \bar{c}_\infty}{2\sqrt{\pi}} \left[\sqrt{\frac{e\phi_p}{kT_\infty}} + \frac{\sqrt{\pi}}{2} e^{\frac{e\phi_p}{kT_\infty}} \operatorname{erfc}\left(\sqrt{\frac{e\phi_p}{kT_\infty}} \right) \right] && (2.3)\\
&\rightarrow \frac{en_\infty \bar{c}_\infty}{2\sqrt{\pi}} \sqrt{\frac{e\phi_p}{kT_\infty}} && (2.4)
\end{aligned}
$$

since, in the limiting form, $x \rightarrow \infty$, we have

$$
\begin{aligned}
\operatorname{erfc}(x) &= 1 - \operatorname{erf}(x) = \frac{2}{\sqrt{\pi}} \int_x^{\infty} e^{-t^2} dt && (2.5)\\
&\rightarrow \frac{1}{\sqrt{\pi}} \frac{e^{-x^2}}{x} && (2.6)
\end{aligned}
$$

where $\bar{c}_\infty$ is the random thermal velocity given as

$$
\bar{c}_\infty = \sqrt{\frac{8kT_\infty}{\pi m_e}} \tag{2.7}
$$

Therefore, when $\frac{e\phi}{kT_\infty} >> 1$, the current density (2.4) becomes

$$
j = \frac{en_\infty}{\pi} \sqrt{\frac{2e\phi_p}{m_e}} \tag{2.8}
$$

which is independent of electron temperature, T_e. Note that equation (2.3), and hence equation (2.8) are independent of the shape of the cylinder's cross section (as long as OML conditions prevails). Also, for a given shape, the current density j is independent of location within the surface.

When a three-dimensional problem is considered, the electrons counted in the calculation of the OML current collection are characterized by

$$\frac{1}{2}m_e(w_x^2 + w_y^2 + w_z^2) - e\phi_p \geq 0. \tag{2.9}$$

The 3D OML current is also calculated in the same manner as in the 2D case,

Very important results of their work are ; conservation of angular momentum is not used, and therefore the shape of the probe is irrelevant.

2.2.3 Sanmartín and Estes (1999)

Both *Langmuir and Mott-Smith* and *Laframboise and Parker* calculations are based on the assumption that the probe is already in the OML regime. *Sanmartín and Estes* calculated the limit of the probe radius for the current collection to be in the OML regime, by solving Poisson's equation with the right-hand-side term calculated by taking the integral of the distribution function in (J, E) space, where J is angular momentum and E total energy. The Maxwellian distribution was taken for the distribution function.

Poisson's equation in the cylindrical coordinates for the potential $\phi(r)$ is

$$\frac{\lambda_{Di}^2}{r}\frac{d}{dr}\left(r\frac{d}{dr}\frac{e\phi}{\kappa T_i}\right) = \frac{n_e}{n_\infty} - \frac{n_i}{n_\infty} \tag{2.10}$$

where λ_{Di} is the ion Debye length and $\lambda_{Di} = \lambda_{De}\sqrt{T_i/T_e}$. with boundary conditions $\phi = \phi_p$ at $r = R$ (the probe surface) and $\phi \to 0$ as $r \to \infty$. For the $e\phi_p >> \kappa T_i, \kappa T_e$ the repelled-particle (ion) density, n_i, is given by the simple Boltzmann law,

$$n_i \approx n_\infty \exp\left(-\frac{e\phi}{\kappa T_i}\right) \tag{2.11}$$

The electron density, n_e, is then expressed as an integral of the undisturbed Maxwellian

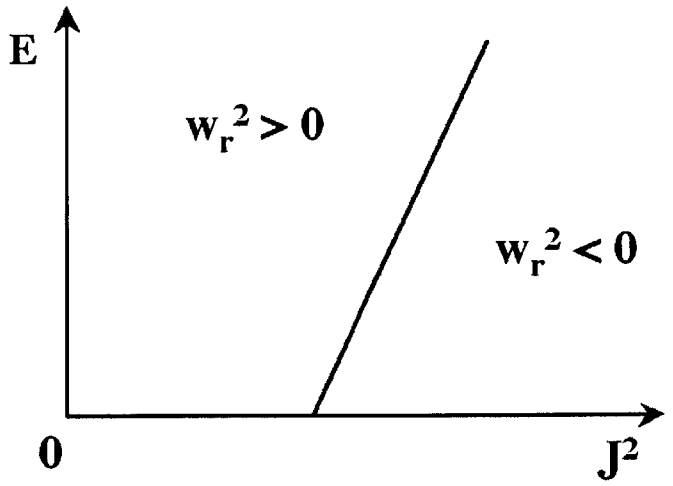

Figure 2-1: Region of integration for the calculation of current collection in (J, E) space.

distribution function over appropriate velocity ranges.

$$\frac{n_e}{n_\infty} = \int\int \frac{\exp(-E/\kappa T_e) dE\ dJ}{2\pi\kappa T_e \sqrt{J_r^2(E) - J^2}}, \tag{2.12}$$

where $J \equiv m_e r w_\theta$ and $J_r^2(E) \equiv 2m_e r^2[E + e\phi(r)]$.

The domain of integration in equation (2.12) depends on r due to the electron capture at the probe and the electric field. For an incoming electron with positive total energy, $E > 0$, to actually reach a point, r, w_r^2 must be positive throughout the entire range, $r < r' < \infty$. This condition is given from (1.3) as

$$m_e^2 r^2 w_r^2 = J_r^2(E) - J^2, \tag{2.13}$$

Since for an incoming electron, J is a constant, the range of integration for the given energy is

$$0 < J < J_r^*(E) \equiv \text{minimum}(J_{r'}(E); r \leq r' < \infty). \tag{2.14}$$

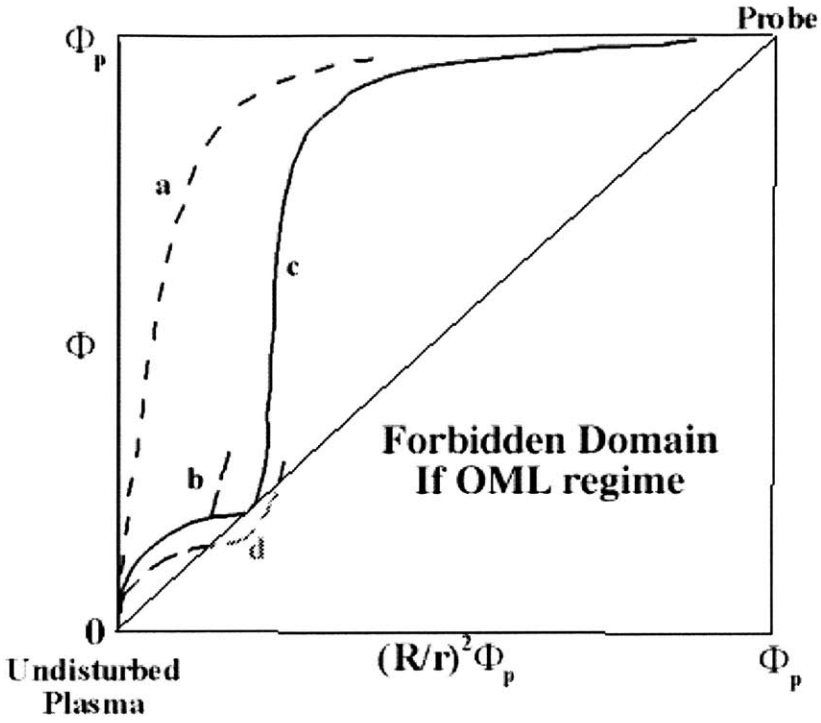

Figure 2-2: Graphical criterion of potential profile for the OML current collection

If $J_r^*(E)$ is different from $J_r(E)$, those electron in $J_r^*(E) < J < J_r(E)$ never reach r, and must be excluded from the integral in (2.12). For an outgoing electron with the positive total energy, E, the range of integration of J becomes

$$J_R^*(E) < J < J_r^*(E). \tag{2.15}$$

Electrons in the range $0 < J < J_R^*(E)$ have been captured by the probe.

The current to the probe is obtained easily as

$$I = 2RLen_\infty \sqrt{\frac{2e\phi_p}{m_e}} \int_0^\infty \frac{dE}{\kappa T_e} \exp\left(\frac{-E}{\kappa T_e}\right) \frac{J_R^*(E)}{J_R(0)}. \tag{2.16}$$

The domain of integration in (J, E) space is shown in Fig. 2-1. Current is maximum under the condition $J_R^*(E) = J_R(E)$, for $0 < E < \infty$ [no potential barrier for just

radius R], giving rise to the OML current. With $E \sim \kappa T_e << e\phi_p$, we have $J_R(E) \approx J_R(0)$, equation (2.16) giving,

$$I_{OML} \approx 2RLen_\infty \sqrt{2e\phi_p/m_e} \tag{2.17}$$

The condition for the OML regime to hold, $J_R^*(E) = J_R(E)$ for $0 < E < \infty$, requires the potential to satisfy

$$R^2\phi_p \leq r^2\phi(r)(R \leq r < \infty) \tag{2.18}$$

Condition (2.18) can be illustrated in a $(\phi, \phi_p R^2/r^2)$ diagram (Fig. 2-2). The profile for $R = R_{max}$ would just touch the diagonal, as in the case of c. Profiles a and b would lie in the OML regime, but not d.

Finally the potential distribution in the OML regime was calculated by substituting the current obtained above in the Poisson equation in the sheath layer and matching the boundary condition with the outer layer in an asymptotic form. In doing so, it was also shown that the asymptotic solution of the potential is in the form of $\phi \approx a\phi_p(b - \ln r)$ (a and b are constants determined by the boundary condition with the outer layer), indicating that the high bias makes space-charge effects negligible within some neighborhood of the probe.

2.2.4 Parker-Murphy theory (1967): Magnetized Plasma

In space, there is Geomagnetic field. It is small ($B \sim 0.3G$), but its effect is significant. One of the first major works dealing with magnetic effects on probe current collection is by *Parker & Murphy* [24]. They derive an upper bound of current collection by a spherical probe using canonical angular momentum. They assume negligible thermal effects and very high probe potential. The calculation of upper bound of a spherical current collection with thermal effects is treated by *Rubinstein & Laframboise* (1982) [39]. An infinite cylindrical case was done by *Laframboise & Rubinstein* (1976,1978) [30, 38]. The brief derivation of Parker-Murphy theory is as follows

Canonical angular momentum is derived from the Lagrangian. The Lagrangian is given as

$$L = \frac{1}{2}mv^2 + e\vec{A}\cdot\vec{v} - e\phi \tag{2.19}$$

where $\vec{A}$ and ϕ are the vector and scalar potentials of the electromagnetic field. In cylindrical coordinates, this becomes

$$\begin{aligned} &\text{Lagrangian} && :L = \tfrac{1}{2}mr^2\dot{\theta} - e\phi + e\vec{A}\cdot\vec{v} \\ &\text{Velocity} && :\vec{v} = (\dot{r}, r\dot{\theta}, \dot{z}) \\ &\text{Vector potential} && :\vec{B} = \nabla \times \vec{A} \end{aligned}$$

When $\vec{A}$ and ϕ are independent of θ, we have for $\vec{B} = B\hat{z}$ constant,

$$B = \frac{1}{r}\frac{d}{dr}(rA_\theta) \tag{2.20}$$

$$A_\theta(r) = \frac{1}{2}rB \tag{2.21}$$

Thus the Lagrangian becomes

$$L = \frac{m}{2}(\dot{r}^2 + r^2\dot{\theta}^2 + \dot{z}^2) + \frac{1}{2}er^2B\dot{\theta} - e\phi \tag{2.22}$$

Since the Lagrangian is independent of θ, one constant of the motion, the canonical angular momentum is obtained by

$$q \equiv \frac{\partial L}{\partial \dot{\theta}} = mr^2\dot{\theta} + \frac{1}{2}er^2B \tag{2.23}$$

$$= mr^2(\dot{\theta} + \frac{\omega_c}{2}) \tag{2.24}$$

which corresponds to equation (10) in the paper of Parker and Murphy. ω_c is the electron cyclotron frequency.

Another constant of the motion is the energy, given as

$$E = \frac{m}{2}(\dot{r}^2 + \dot{z}^2 + r^2\dot{\theta}^2) - e\phi(r, z) \tag{2.25}$$

which is equation (11) in their paper.

Eliminating $\dot{\theta}$ from these equations, we have

$$r^2\left(\frac{2q - m\omega_c r^2}{2r^2 m}\right)^2 = \frac{2}{m}(E + e\phi) - (\dot{r}^2 + \dot{z}^2)$$
$$< \frac{2}{m}(E + e\phi) \tag{2.26}$$

For $\dot{\theta} = \dot{\theta}_\infty$ and $r = r_0$, we have

$$q = r^2(\dot{\theta} + \frac{\omega_c}{2}) = r_0^2(\dot{\theta}_\infty + \frac{\omega_c}{2}). \tag{2.27}$$

Substituting this into (2.26) and taking a square root, we have

$$\frac{(r_0^2 - r^2)\omega_c + 2r_0^2\dot{\theta}_\infty}{2r^2} < \left(\frac{2(E + e\phi)}{mr^2}\right)^{1/2} \tag{2.28}$$

On the probe, i.e. $r = a, \phi = \phi_0$, this becomes

$$\frac{(r_0^2 - a^2)\omega_c + 2r_0^2\dot{\theta}_\infty}{2a^2} < \left(\frac{2(E + e\phi_0)}{ma^2}\right)^{1/2} \tag{2.29}$$

Thus the PM limit is given as

$$\frac{r_0^2}{a^2} < \frac{\omega_c}{\omega_c + 2\dot{\theta}_\infty}\left\{1 + \left(\frac{8(E + e\phi_0)}{ma^2\omega_c^2}\right)^{1/2}\right\} \tag{2.30}$$

Since $\dot{\theta}_\infty << \omega_c$ and $E << e\phi_0$, this becomes a familiar form of Parker-Murphy law.

$$\frac{r_0^2}{a^2} < 1 + \left(\frac{8e\phi_0}{ma^2\omega_c^2}\right)^{1/2} \tag{2.31}$$

The current collection is calculated by multiplying the thermal current density at infinity by πr_0^2. Along the B-field, a tube of radius r_0 is extending to infinity. All electrons inside this tube are considered to contribute to the current collection. Note that this analysis does not require the specification of the potential form. The only assumption used is that ϕ is independent of θ.

2.2.5 Laframboise & Rubinstein (1976,1978,1983) Infinite cylindrical and spherical probes in magneto-plasma

In general, it is very difficult to find the equivalence of Parker-Murphy theory for a cylindrical probe, because, despite the two dimensional geometry of the probe, the particle motion is highly three dimensional. In terms of OML, when $B = 0$, all particles with $E_\perp \equiv \frac{1}{2}m_e v_\perp^2 > 0$ are considered in the calculation of density, current density ,etc. in the OML regime. However in the presence of magnetic field, there will be $E > 0$ orbits which intersect the probe repeatedly due to the gyration. In reality, a particle on this orbit is collected by the probe only once. All the other sections of the orbit correspond, in terms of *Laframboise & Parker* (1973), to those which are traced back to the probe again, not to ∞.

In order to calculate the current collection to an infinite cylindrical probe, *Laframboise & Rubinstein* [30, 38, 39] assume that electric potential changes within a mean gyroradius $\bar{a}$ are small enough (the sheath is thick enough and B is large enough) so that all orbits can be approximated by helices between any two intersections with the probe. As in the OML theory, any orbit connecting to the probe from ∞ will carry a population given by the distribution function at ∞ (Maxwellian). Therefore the problem of calculating current becomes a detailed study of the intersections of helices with the probe. *Laframboise & Rubinstein* solved the equation of motion of an electron, $m\dot{v} = -ev \times B$ for each orbit, checked if it intersected the probe and calculated the current to the probe numerically.

They also calculated the adiabatic effects on current collection. The abovementioned approximation is valid in the limit $\bar{a} \ll L_\phi$, where $L_\phi^{-1} = |\phi^{-1}\nabla\phi|$. However, if this limit is approached, the limit $\bar{a} \ll L_E$ will in general be approached, where L_E is the characteristic scale of changes in the probe sheath electric field. In the latter case, the guiding-center approximation for particle motion is valid, and the quantity $\frac{1}{2}mv_x^2 + q\phi$ becomes an adiabatic invariant, i.e. the kinetic energy gain of incoming particles goes entirely into increased speed along B. As a result, a more attracting

probe potential can alter current collection only by increasing the pitch of orbits near the probe. This leads to more particles bypassing the probe, thus missing it. Current will be decreased, yielding a negative-resistance characteristic.

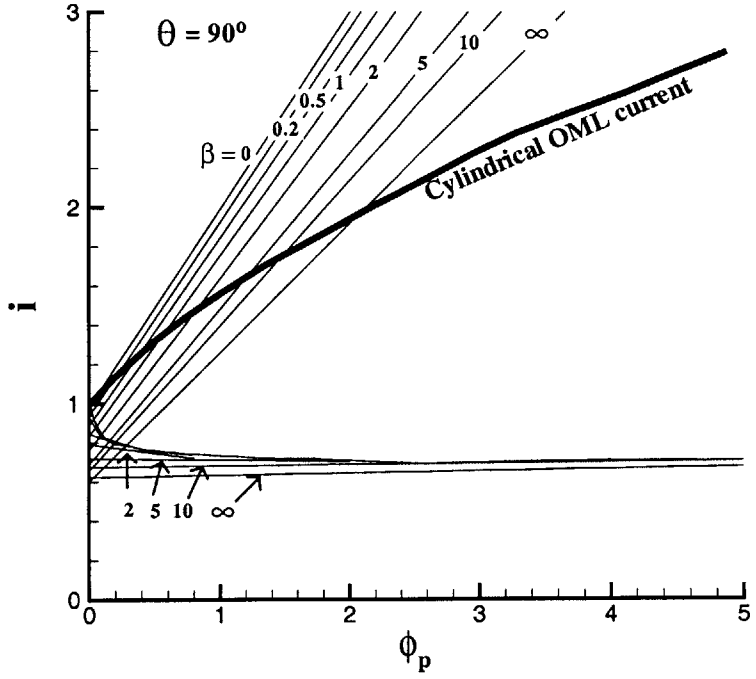

Figure 2-3: Current $i = I/[r_p n_\infty \sqrt{2\pi\kappa T_e/m}]$ vs probe potential $\phi_p = e\phi_p/\kappa T_e$ for various values of $\beta = r_p/\bar{a} = r_p eB(2/\pi mkT)^{1/2}$ ($\bar{a}$ =mean gyroradius, r_p =probe radius)

In Figure 2-3, the increasing and decreasing lines represent upper bound and adiabatic limit currents from the calculation of *Laframboise & Rubinstein* [30], with the cylindrical OML current. Although this current is no longer an upper bound if $\beta \neq 0$, it still represents an upper bound for the limit when electric forces on particles are much larger than thermal forces, i.e. $\chi_p \gg 1$. What we can notice here is that, as the probe potential becomes larger, the discrepancy between upper (OML if $\phi_p \gg 1$) and lower limit gets larger. Then a question arises of how the actual current collection behaves between these limit as we increase the probe potential. *Laframboise and Sonmor* (1993) [21] explain that when ϕ_p is small, the actual current is expected

to approach the lower adiabatic-limit current, since the adiabatic-limit condition is that changes in the probe sheath electric field are small over an average particle gyroradius. Then as ϕ_p becomes more positive, adiabatic-limit conditions will break down, and collected currents will rise toward the upper-bound values. *Laframboise* also mentioned that this "N-shaped" current-voltage characteristic was seen in the data from spherical (not cylindrical) electrostatic probes on the University of Iowa Plasma Diagnostics Package flown on several space shuttle flights. (Laframboise and Sonmor in private communications with G.B. Murphy, 1983).

Laframboise and Rubinstein also calculate the current collection to a spherical probe in magnetoplasmas (PM theory) with thermal effects. They used the same technique used in the case of cylindrical probes. The result was that for small probe potentials, they obtained the canonical upper bound as in the spherical case, and the adiabatic-limit "negative-resistance". The difference from the spherical case is that for large probe potentials thermal effects remains evident for small β's.

2.2.6 Laframboise (1997) After TSS-1/R : Magnetic presheath

Since results from the TSS-1/R fights revealed the current collections to the spherical probe to be $2 \sim 3$ times higher than the upper-bound Parker-Murphy model, there have been many theories trying to explain the enhancement of the current collection. The strong new effect here is meso-sonic flow around the tether. It is not surprising that new phenomena would arise.

Laframboise (1997) [22] introduced the concept of "magnetic presheath", which extends very far from the spacecraft in both directions along the geomagnetic field, an ion-enhancement region, also quasineutral, which is located forward of the magnetic presheath and concentrates the electron flux passing into it, and an elongation, along the drift direction, of the electron collection area perpendicular to the geomagnetic field.

The steady-state version of his theory leads to an upper-bound current collection

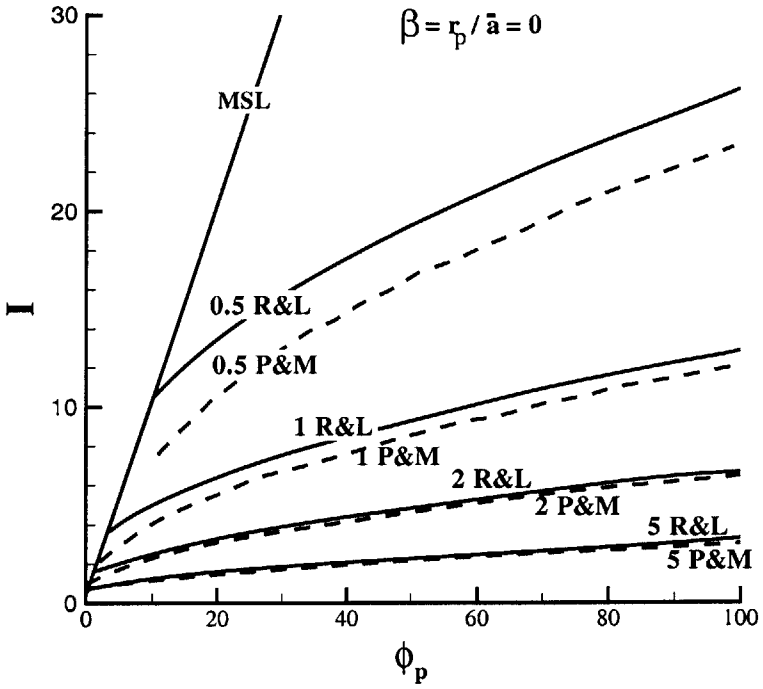

Figure 2-4: Comparison of the *Rubinstein and Laframboise* [1982] (solid line) and *Parker and Murphy* [1967] canonical upper-bound values for dimensionless attracted-particle current I as a function of dimensionless probe potential ϕ_p, for various values of the dimensionless magnetic field strength β. The curve for $\beta = 0$ is the *Mott-Smith and Langmuir* [1926] orbit-limited current result [21].

prediction of 6.4 times the *Parker and Murphy* (1976) current, independently of sub-satellite voltage. The relative ion drift speed U, even though small compared to $\bar{v}_e$, nonetheless turns out to be crucial in obtaining this increased current. This is because $U >> v_{T,i}$, so the ion flow is actually hypersonic, and shows strong new features. They also modified this theory to account partly for effects of plasma instabilities. The ion-enhancement region violates the Bohm criterion for stability locally unless electron density is enhanced as well. The two-stream instability in the magnetic wing was considered in order to account for the electron density enhancement.

Laframboise's account of the enhanced current collection was as follows; if both the Debye length and the average ambient-electron gyroradius of the surrounding plasma are much smaller than the spacecraft or probe, the sheath surrounding it will

be of limited extent, but a magnetic presheath will also form, defined as a quasineutral electric-potential disturbance which extends very far in both directions (See Figure 2-5).

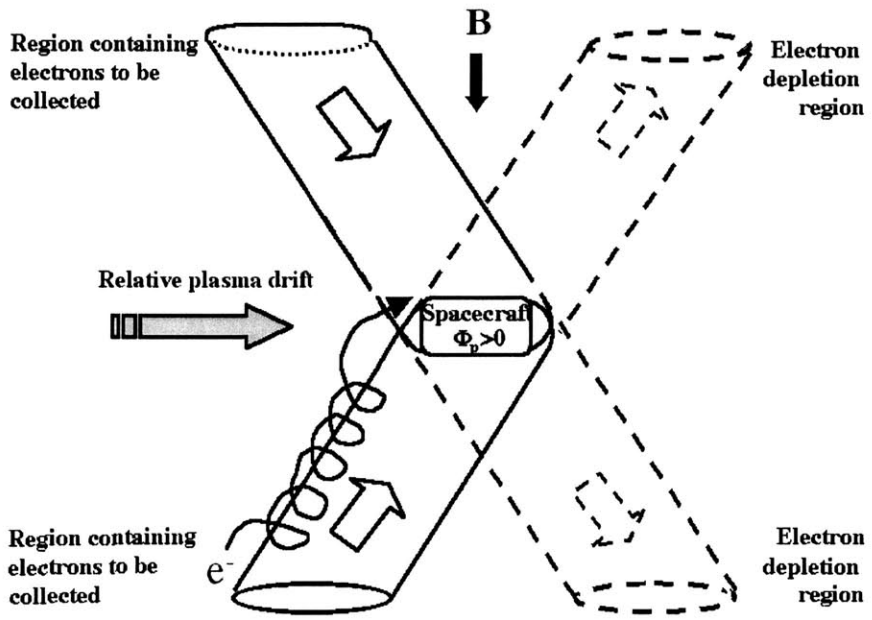

Figure 2-5: Magnetic presheath proposed by *Laframboise* [1997]

Within the magnetic presheath, there will be a depletion of electrons whose velocity components along the geomagnetic field B are directed away from the spacecraft. The magnetic presheath therefore will be a region of positive potentials.

If this depletion is almost complete, the electron density in this region will be decreased by about half, and in order that quasineutrality be attained, potentials within this region must be large enough to repel about half the ions from it. The drift energy of O^+ ions moving at $U = 8km/sec$ is 5.35 eV, so we therefore expect that potentials within the magnetic presheath will be of the order of $5V$.

The mechanism of steady-state enhanced current collection is that electrons in the magnetic presheath accelerate due to the elevated potential ($\sim 5eV$). This acceleration of electrons elongates the electron-collection region (See Fig 2-5). This increase of the collecting area from the Parker-Murphy model turned out to be by a factor

which approaches 2 in the limit.

2.2.7 Cooke & Katz (1994,1998): Plasma heating in the presheath

Plasma heating is taken into account in the work by *Cooke & Katz* (1994,1998) [4, 2] for the enhanced current collection. This model postulates the heating that occurs as electrons fall through the potential necessary to reflect the ram ion while satisfying the Bohm sheath stability criterion. The Bohm sheath stability criterion claims that throughout the shielding region surrounding a probe the sign of the charge density be opposite that of the probe. Otherwise the Bohm unstable sheath suffers fluctuations. *Katz et al* (1994) demonstrated that magnetically constrained electrons can not match even a constant ambient ion density in the presheath and it was postulated that this Bohm unstable sheath suffers fluctuations sufficient to establish an unmagnetized electron fluid. It was also assumed that electrons in the presheath are trapped by

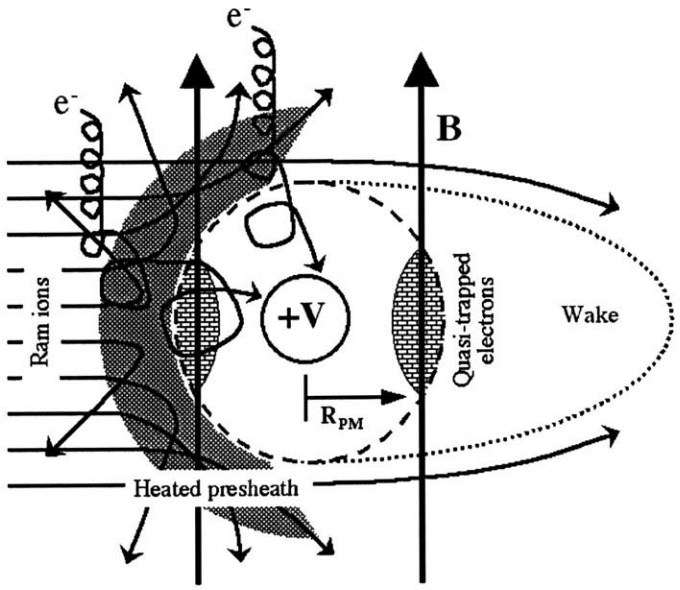

Figure 2-6: Plasma heating in the presheath due to the Bohm instability [2]

the fluctuations long enough to participate in the collective oscillation so that the

fluid description may be reasonable. They derived from fluid equations the relation between δT_e (electron temperature increment) and δV (local potential increment in the presheath) as $\delta T_e = \frac{2}{5}\delta V$. In the ionosphere, the ion ram energy is of $5eV$, leading to $\delta T_e \sim 2eV$. The corresponding current enhancement is shown to be 2.5 times P-M current (See Fig. 2-7)

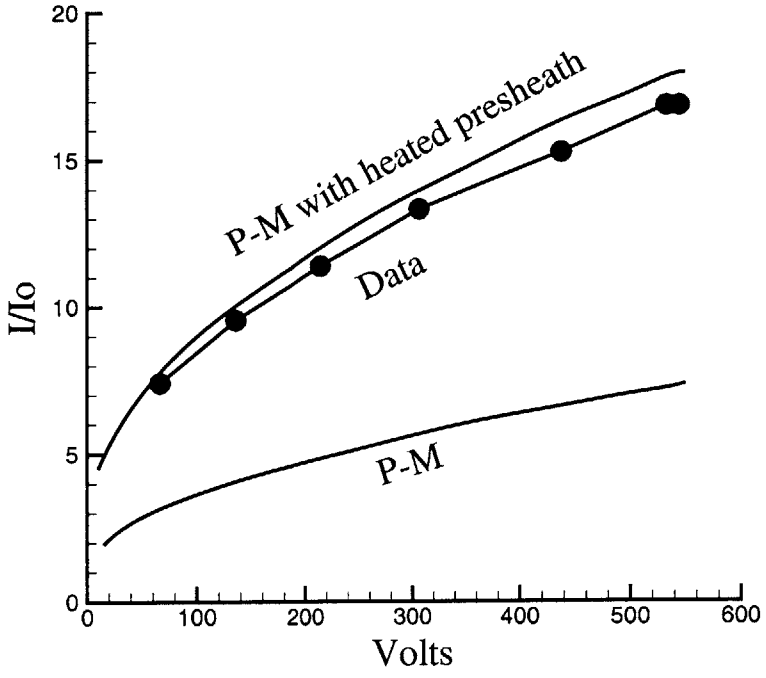

Figure 2-7: Parker-Murphy current collection with heated presheath

Yet unknown in this theory is the mechanism generating the scattering and the scattering frequency. And also the mechanism of trapping electrons in the presheath is left to be studied.

2.3 Experimental Works

Actual experimental tests of Langmuir Probe theory often encounter difficulties in the comparison with theoretical values. There are many effects which inevitably modify

the plasma settings and make it difficult to single out the probe phenomena. For example, end effects of cylindrical probes, asymmetric geometries of spherical probes due to the supporting prop and the difficulties in the measurement of ambient plasma parameters are major causes. And also laboratory simulations of space plasmas inevitably bring about the wall effects of the vacuum chamber. The scientific community of experimental plasma physics is active in controlled electron beam experiments in space and laboratory [23]. Their studies are often focused on the parametric study of the interaction between beams and the plasma, i.e. the boundaries in parametric space between single-particle characteristics and collective beam-plasma effects. So far, I have not found many works on Langmuir Probe experiments set in space plasma or in laboratory simulations without beam injections for positive large bias. In this section, I briefly touch on a few of those works on the ground and space experiments of passive Langmuir probes (without beams).

2.3.1 Gilchrist and Bilén: Electron current collection by Bare EDT (Ground Experiment)

Electron current collection by a cylindrical probe was measured in laboratory experiments by *Gilchrist & Bilén* [29]. They use a Hall thruster (P5 thruster) as a flowing plasma source. The thruster was run on xenon propellant ($m_i = 2.18 \times 10^{-25} kg$). An estimate average bulk directed energy was $21(eV)$. Other plasma parameters are ; electron temperature $T_e = 0.8eV$, probe radius $r_p = 0.14mm$ and the Debye length ranges $1 \sim 3$ times probe radius.

The data showed that at voltages ($> 60V$) somewhat above the estimated energy of the incoming beam of ions ($21(eV)$) collected currents were seen to be enhanced over the OML [31], but only slightly (Figure 2-8).

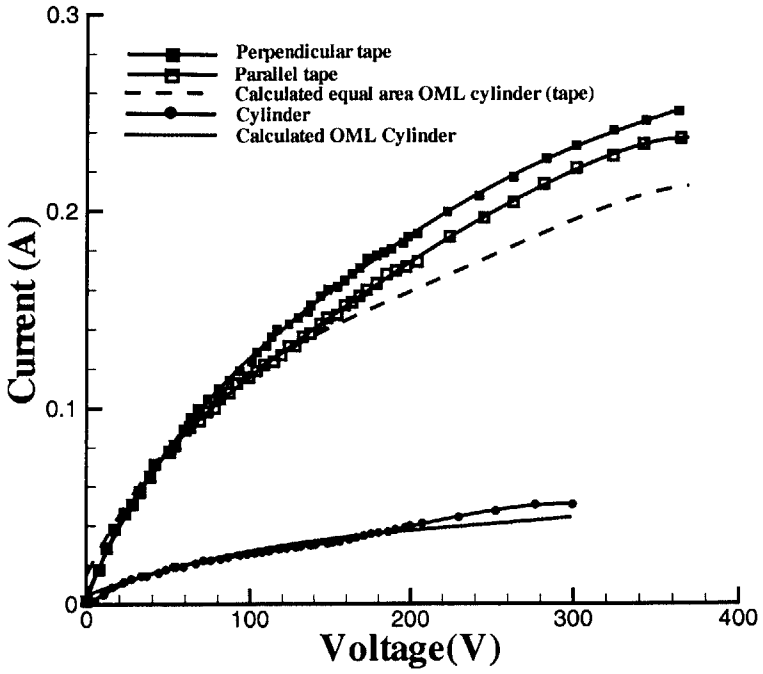

Figure 2-8: Experimental Data and OML of Bare EDT's

2.3.2 Tether Space Experiments

Since the 1960's, there have been several space experiments using tethers. Some were to investigate the dynamics of the tether, others to investigate the electrodynamics of the ED tether. Table 2.1 shows the list of known space tether missions. The first demonstration of a nonconducting tether took place in 1967 with Gemini II in low Earth orbit illustrating gravity gradient stabilization.

The first mother-daughter tethered rocket experiment was conducted in 1980 by the Institute of Space and Astronautical Science (ISAS) and Utah State University using a Japanese sounding rocket. The experiment was repeated in 1981 and 1983. The latter experiment was designated as CHARGE-1 (Cooperative High Altitude Rocket Gun Experiment). A reflight of the CHARGE payload (CHARGE-2) was successfully carried out in December 1995. In CHARGE-2, electron beams from 0.5 to $48mA$ at $1keV$ were injected from the mother payload and voltage up to $500V$ was

Name	Date	Orbit	Length	Comments
Gemini 11	1966	LEO	30 m	Spin stable 0.15 rpm
Gemini 12	1966	LEO	30 m	Local vertical, stable swing
H-9M-69	1980	Suborbital	500 m	Partial deployment
S-520-2	1981	Suborbital	500 m	Partial deployment
Charge-1	1983	Suborbital	500 m	Full deployment
Charge-2	1985	Suborbital	500 m	Full deployment
ECHO-7	1988	Suborbital		
Oedipus-A	1989	Suborbital	958 m	Spin Stable 0.7 rpm
Charge-2B	1992	Suborbital	500 m	Full deployment
TSS-1	1992	LEO	<1 km	Electrodynamic, partial deploy, retrieved
SEDS-1	1993	LEO	20 km	Downward deploy, swing and cut
PMG	1993	LEO	500 m	Electrodynamic, upward deploy
SEDS-2	1994	LEO	20 km	Local vertical stable, downward deploy
Oedipus-C	1995	Suborbital	1 km	Spin stable 0.7 rpm
TSS-1R	1996	LEO	19.6 km	Electrodynamic power generation and science
TiPS	1996	LEO	4 km	Long-life tether
ATEx	1999	LEO	<30 km	Incomplete deployment

Table 2.1: Summary of known space tether missions [32]

applied between the two payloads with and without the beam injection [35].

In the 1990's, several important *in-situ* tether experiments took place. Those included the retrieval of a tether in space [Tethered Satellite System-1 (TSS-1)], successful deployment of a $20km$ tether in space [Small Expendable Deployer System-1 (SEDS-1)], closed loop control of tether deployment (SEDS-2), and operation of an electrodynamic tether (EDT) with tether current driven in both directions:power and thrust modes [Plasma Motor Generator (PMG)].

Although the TSS-1R mission was not completed as planned, the Italian satellite was deployed to a distance of 19.7 km–making the TSS-1R the largest man-made electrodynamic structure ever placed in orbit. This deployment was sufficient to

generate high voltages across the tether and extract large currents from the ambient plasma. These voltages and currents, in turn, excited several space plasma phenomena and processes of interest.

One of the significant findings in TSS-1R is the enhancement of the current collection. Currents collected by the satellite at different voltages exceeded the levels predicted by Parker-Murphy theory, which predicts the upper limit of current collection in the steady condition, by factors of up to three. Parker-Murphy theory is explained in section 2.2.4.

2.4 Computational Works

Numerical works for collisionless plasma have been performed since 1960's. When reasonably fast CPU's and Memory space were not available like these days, simulations traced many particle orbits from infinity, where the distribution is Maxwellian, to a probe according to the potential field, calculated plasma density, and thus derived a new potential distribution. This procedure was iterated many times till the field quantities converged. However this method tends to miss the plasma fluctuations, since each particle trajectory from infinity to a probe was calculated based on the fixed potential field for each iteration.

Recent computer technology allows us to use many particles at the same time and calculate the potential field simultaneously, those allowing self-consistency in the presence of unsteady effects, such as plasma fluctuations. There are still many practical problems in this method yet to be solved. In the followings, I introduce some works using the abovementioned methods.

2.4.1 Laframboise (1966)

In 1966, in his Ph.D. thesis, *Laframboise* [18] calculated "exact" solutions of current collection by spheres and cylinders in an unmagnetized quiescent plasma. He assumed Maxwellian distribution at infinity and traced many particles to fill the computational domain. In tracing particles, he assumed symmetry of the field quantities and applied

energy conservation and angular momentum conservation. As discussed in Section 2.2.1, when the radius of the probe is comparable to or smaller than the Debye length, his calculation gives rise to the OML current. In addition, he also calculated the current collection outside the OML regime.

In this calculation, mass ratio was unimportant, since the repelled particles (ions) have a Maxwellian-Boltzmann distribution everywhere except for a cut-off tail due to the presence of the probe. However as the probe potential was kept at 25 times higher than the plasma energy, the effect was totally negligible. Since the density of ions, derived from the Maxwellian distribution function, is independent of mass, an arbitrary mass ratio was justified.

Results are shown in Figure 2-9

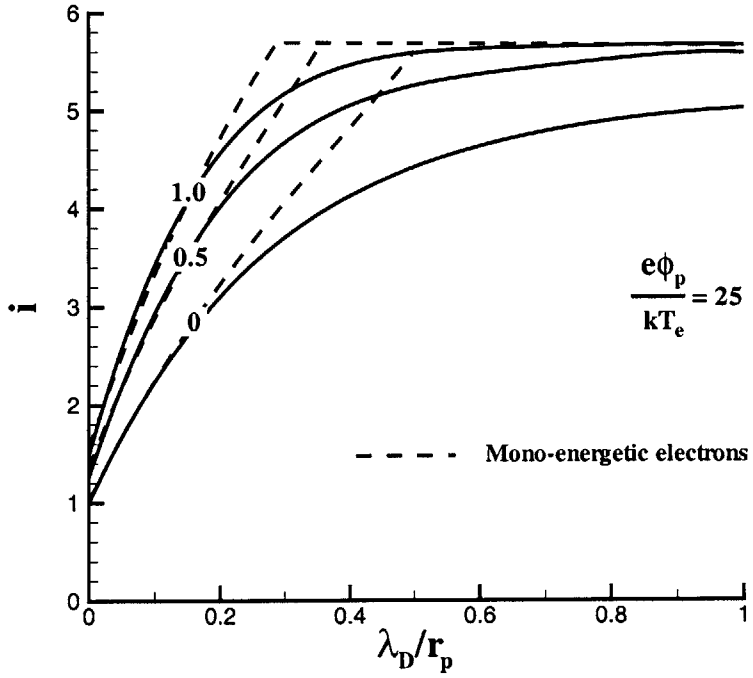

Figure 2-9: Electron current collection to a cylindrical probe inside and outside of OML regime. Solid lines are Laframboise results for $T_e/T_i = 0$, 0.5 & 1.0.

2.4.2 Godard & Laframboise (1975,1983)

In 1975, in his Ph.D. thesis *Godard* [27] calculated the velocity-dependent current collection of the spherical and cylindrical probes. His calculation [28] covers wide ranges of parameters such as the probe radius to Debye length ratio, R_p/λ_D, nondimensional probe potential, $\Xi = e\phi_p/\kappa T_e$, and ion-to-electron temperature ratio T_i/T_e, where e and κ denote the electronic charge and the Boltzmann constant. The sheath distortion has not been taken into account.

2.4.3 Usui (1993)

Usui used Particle-In-Cell (PIC) Method to calculate the current collection by a spherical probe, modeling the cases of TSS-1/R. PIC method has been established as a tool to investigate particle-field interactions in a collisionless plasma [36]. A brief introduction to PIC method is given at Section 3.1.

Usui [37] used a two-dimensional electromagnetic code and a three-dimensional electrostatic code. He successfully simulated the Buneman instability near the probe. However the relation between the instability and the current enhancement was left unclear.

2.4.4 Onishi (1998)

In my Master thesis, I introduced a quasi-neutrality condition to improve the quantitative results of PIC method [33]. The importance of this boundary condition stems from the fact that some electrons are absorbed by a tether. I assume here that no ion is absorbed by the tether, because of its very high positive potential. Figure 2-10 illustrates the overall flow of electrons and ions. Due to this partial absorption of electrons by the tether, the electric potential at the computational outside boundary can not be zero with respect to the ambient plasma. If it were zero, the electron density would be less than the ion density, and thus it would violate the quasi-neutrality outside the sheath. The electric potential at the outside boundary should be non-zero so that the quasi-neutrality is maintained except for a wake region even with the partial

absorption of electrons. In order to calculate a local potential on the computational boundary, an equation of the quasi-neutrality is solved and non-zero potential at each boundary point is derived. Details are given in the next chapter.

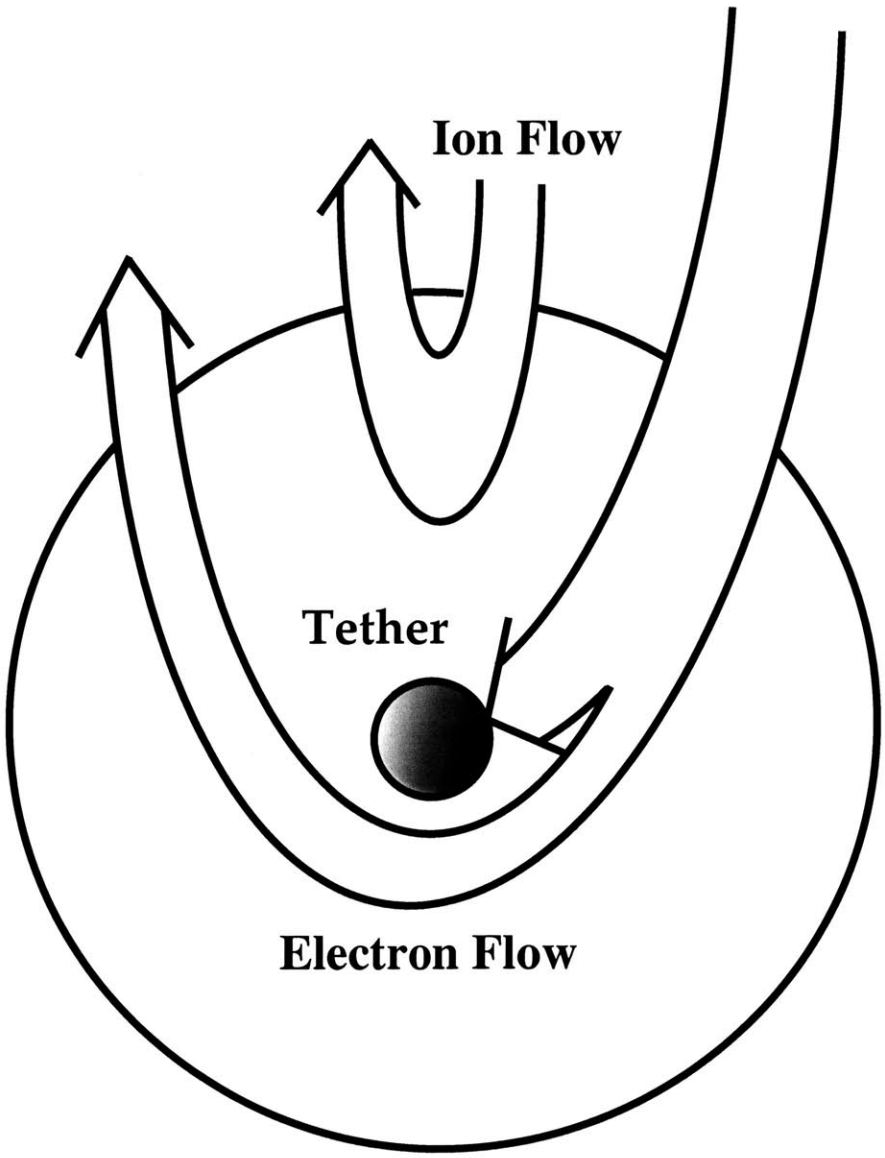

Figure 2-10: Electron and Ion Flows

2.5 Conclusions on Previous Works

There have been many works on the Langmuir probe theory for various plasma conditions. The pioneer work is that of *Langmuir et al* in 1920's. He and his colleagues derived the Current-Voltage (C-V) characteristics in a quiescent unmagnetized plasma, by using energy conservation and angular momentum conservation. They also derived and named the Orbital-Motion-Limited (OML) current, which is the upper limit of current collection in a steady collisionless isotropic plasma.

In 1973, *Laframboise and Parker* re-derived the OML current collection without using the angular momentum conservation. Only a particle's total energy is taken into account in the their derivation. Their work eliminated a strong restriction imposed by the angular momentum conservation, that is the symmetry of potential field. This argument makes the OML theory applicable to any kind of the probe shape.

A formula for current collection to a spherical probe which includes the magnetic effects was first derived by *Parker and Murphy* in 1967. They derived an upper bound to current collection by a spherical probe using canonical angular momentum. They assumed that thermal effects are negligible and the probe potential is very high.

Laframboise and Rubinstein tried to derive the cylindrical version of PM theory. However, the fact that the particle motion is highly three dimensional despite the probe's two dimensional geometry forced them to introduce a strong assumption that electric potential changes within a mean gyroradius are so small that all orbits can be approximated by helices. This assumption led them to lower and upper limits of current collection. As far as the upper limit is concerned, it was shown that the OML is still the upper limit for a high probe potential.

Laframboise and Rubinstein also added the thermal effects to the PM theory (a spherical probe) and derived current collection slightly higher than the PM model for small β's (β =Probe Radius/Gyro Radius).

After TSS-1/R results revealed the enhanced current collections to a spherical probe, *Laframboise* introduced the concept of magnetic presheath to account for an enlarged "tube" in PM theory. *Cooke and Katz* pointed out the possibility of plasma

heating in the presheath due to the Bohm instability.

Among many ground and space experiments, one of the most important works is TSS-1R space experiment. TSS-1R revealed that the current collection by a large spherical probe in the ionosphere is $2 \sim 3$ times higher than the previously expected upper limit. This results indicated the possibilities of particle-field interactions and plasma heating (instabilities).

The Particle-In-Cell (PIC) method has been established as a tool to analyze particle-field interactions in a collisionless plasma. *Sigh et al*, *Usui* and *Onishi* have applied this method to calculate the current collection to a spherical or cylindrical probe under flowing magnetized plasma conditions. They have obtained satisfactory qualitative results such as $E \times B$ drift, wake region, magnetic presheath etc. However further work is still required to obtain a good quantitative approximation and thus explain the physics of the enhanced current collection.

Chapter 3

Computations

To study in detail flowing effects as well as magnetic effects on the electron current collection by a bare tether, a two-dimensional Particle-In-Cell (PIC) code has been developed, which treats electrons and ions totally kinetically. Although the PIC method has been established to study plasma physics and has been applied to many researches, it still has many technical issues which have to be resolved. In this chapter, a brief introduction of PIC is made, followed by specification of our model and the explanation of technical issues and their resolution in order for a PIC method to obtain qualitatively and quantitatively good results.

3.1 Particle-In-Cell (PIC) method

The Particle-In-Cell (PIC) method has been very successful in the simulation of collisionless plasmas. In PIC, many particles are distributed in phase space. That is, a particle's motion is described by its position and velocity. In kinetic theory, this particle distribution is defined as a distribution function and governed by the Boltzmann equation. The Boltzmann equation with no collisional term on its right-hand side is given as follows. (Vlasov's equation)

$$\frac{\partial f}{\partial t} + \mathbf{v}\frac{\partial f}{\partial \mathbf{x}} + \frac{\mathbf{F}}{m_e}\frac{\partial f}{\partial \mathbf{v}} = 0 \tag{3.1}$$

In an actual computation, the number of particles available is much less than that in reality. This fact requires us to introduce the concept of a "superparticle", corresponding to a group of real particles. One superparticle contains many real particles, and as many particles as another.

To describe the motion of the superparticle, we need to know the velocity and the force acting on it. The force acting on a superparticle could be calculated by considering all Coulomb forces caused by the other superparticles. However, this calculation is computationally too expensive. Instead of doing so, PIC uses a grid on which Maxwell's equations are solved to give the electric field, which is then interpolated to the position of each superparticle. As the name "Particle-In-Cell" implies, in a computational domain, a superparticle moves through a grid or a cell, regardless of the position of grid nodes. A PIC code method consists of four processes as described below.

At each time step, the electric charge density on each node is estimated from the positions of all superparticles. This first process is called "charge assignment". Then on a grid, the electric potential and electric field are computed. We use a finite difference method in this second process; especially to solve Poisson's equation, we use Successive Line OverRelaxation (SLOR). Poisson's equation to relate electric potential to charge density is

$$\nabla^2\phi = -\frac{\rho}{\epsilon_0} \tag{3.2}$$

where $\rho = e(n_i - n_e)$ is the electric charge density , and the electric field is

$$\mathbf{E} = -\nabla\phi. \tag{3.3}$$

if $\frac{\partial \mathbf{B}}{\partial t}$ can be neglected.

After computing $\mathbf{E}$ on a grid, the electric field is interpolated onto each superparticle's position, and the corresponding force and acceleration of a superparticle is calculated. This third process is called "interpolation". The first and third processes involve different weighting functions in a energy conserving algorithm. When the particle energy is much higher than the field energy, we can neglect the violation of energy

conservation and use instead a momentum conserving mover. In our model particle energy ($\sim 0.1eV$) is comparable to or even smaller than the field energy ($25eV$ at the tether surface), and therefore it may seem to be better to choose an energy conserving mover. In Figure 3-1, time histories of typical electron's total energy, kinetic energy and potential energy from both algorithms used in our simulation are plotted. The comparison between these two algorithms shows that the momentum conserving algorithm is the better choice. Total energy conserving algorithm using the nearest four points conserves total energy as long as an electron stays within a cell during one timestep. The "self-force" due to the different weighting functions used in the total energy conserving algorithm induces some error. Momentum conserving algorithm conserves the momentum even if an electron travels though a cell boundary. The error expected in the momentum conserving algorithm for the low electron temperature originates from the particle-field interaction at long wavelengths [36]. The particle-field interaction which is expected to happen in our model, e.g. two-stream instability, is likely to be at wave lengths larger than the computational domain. Therefore, even with the momentum conserving algorithm, we may expect a sufficiently good total energy conservation. Our choice for this work is the momentum conserving algorithm. Paradoxically, the "energy conserving" algorithm does not conserve energy.

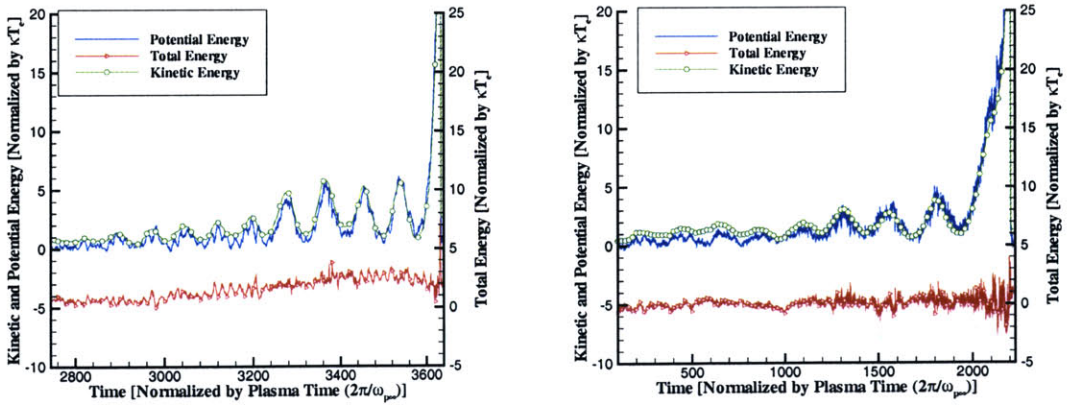

(a) Total Energy Conserving Algorithm

(b) Momentum Conserving Algorithm

Figure 3-1: Momentum and total energy conserving algorithms

Once we know the acceleration, a leapfrog method, the final process, updates the velocity and position of each superparticle as follows;

$$\mathbf{v}_{new}^{(n)} = \mathbf{v}_{old}^{(n-1)} + \frac{q\mathbf{E}^{(n-1/2)}}{m}\Delta t \tag{3.4}$$

$$\mathbf{x}_{new}^{(n+1/2)} = \mathbf{x}_{old}^{(n-1/2)} + \mathbf{v}_{new}^{(n)}\Delta t. \tag{3.5}$$

This completes one iteration in a PIC calculation. One cycle of a PIC is shown skematically in fig 3-2.

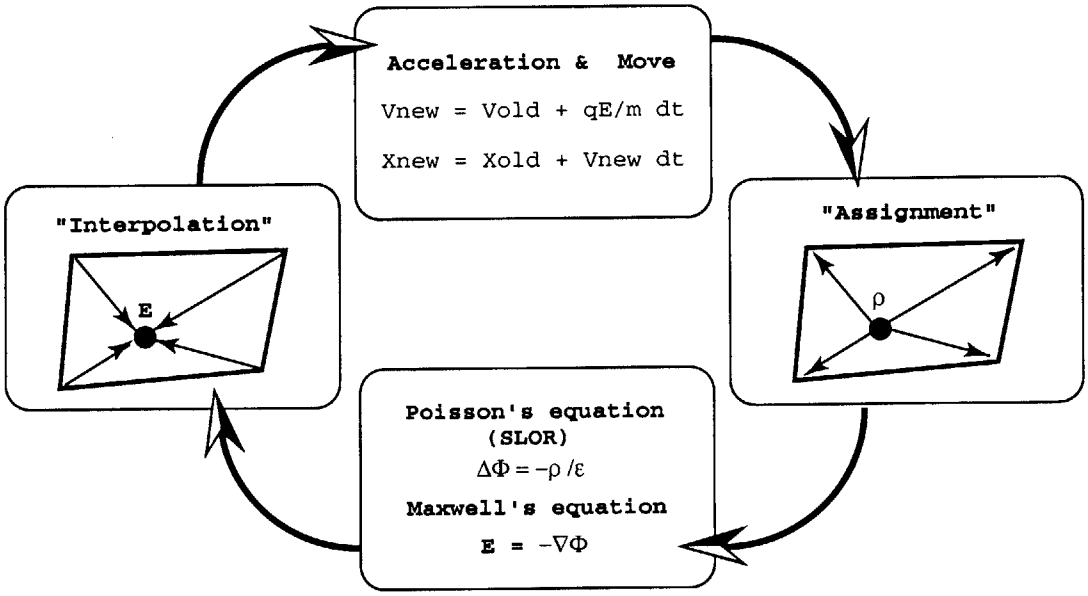

Figure 3-2: A typical cycle of PIC

3.2 Specifications of our models

I have developed two PIC codes with different grid systems in order to calculate current collection to a cylindrical tether, depending on the plasma model that we elaborate on. The model of a quiescent unmagnetized plasma has been developed in order to test the feasibility of the PIC method to calculate electron current collection to a cylindrical probe. There exists an exact solution of this problem [18] with which

I verify the accuracy of the results obtained with a new boundary treatment that utilizes the quasi-neutrality condition (Section 3.2.4).

3.2.1 Structured cylindrical grid

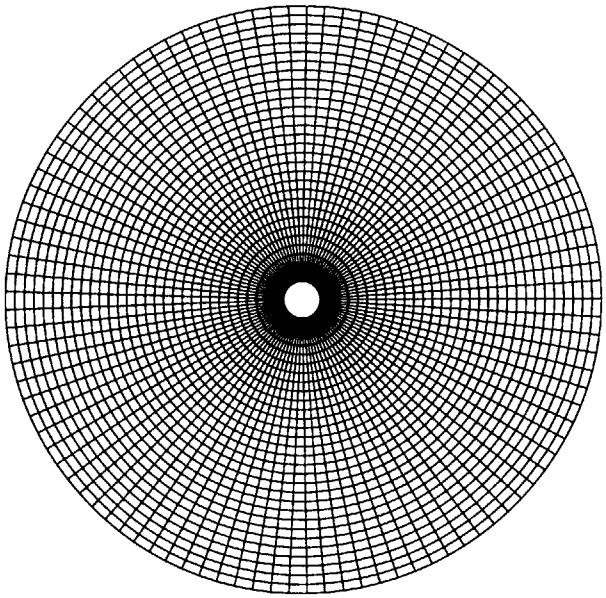

Figure 3-3: Cylindrical structured computational grid for a quiescent unmagnetized plasma

Since the phenomena of a quiescent unmagnetized plasma are axisymmetric, we chose the cylindrical coordinate grid system. The benefit of using cylindrical coordinates is the ease of coding and applying boundary conditions. The drawback is that as it is a structured grid, the size of the computational domain is limited by two numerical conditions; 1) a cell size has to be smaller than the local Debye length, and 2) one cell should contain a certain number of particles in order to maintain a certain accuracy. The first condition is imposed from the outside boundary. The larger the domain, the more cells are required in the azimuthal direction. However on the

surface of the tether, the same number of cells in the azimuthal direction are found. Accordingly the size of cells adjacent to the tether is so small that each cell can not contain enough number of particles. Therefore, the use of a cylindrical structured grid is limited to moderate sizes for the computational domain.

3.2.2 Large Square grid

When the flowing effect is present, the axisymmetric condition on the outside boundary that we used in a quiescent case is no longer valid. There is a wake region behind a tether and magnetic presheath extending to both sides as we shall see later. These asymmetric features of plasma flow require the capability of extending the computational domain in a specific direction. Since slow massive ions are subject to the fast-moving high potential field due to the tether, the ion distribution is then no longer Maxwellian. In these circumstances, the hypothetical mass ratio ($m_i/m_e = 1$) as in a quiescent unmagnetized plasma should be changed to the real mass ratio ($m_i/m_e = 1860 \times 16$, corresponding to atomic oxygen ions).

In Figure 3-4, the computational grid used for the computation of a flowing plasma is indicated. This grid consists mostly of square cells, which enables the fast search of particle positions and the easy extension of the computational domain, and of a small number of non-rectangular grid cells around the tether in order to fit the geometry of the tether surface. All the square grid cells have dimensions as ($0.5\lambda_D \times 0.5\lambda_D$) where λ_D is a Debye length (See Table 3.1). There are 210 cells in the $y-$direction and 160 cells in the $x-$direction in a nominal case. The radius of the tether shown in Figure 3-4 is one Debye length, that is, the *Debye ratio* is unity.

3.2.3 Plasma parameters

Typical plasma parameters are shown in Table 3.1. The parameters are taken based on the actual space environment in which an EDT will be put in practice. Tethered satellites will be orbiting in LEO ($100 \sim 1,000km$) at orbital speed ($U_{tether} = 8 \times 10^3(m/sec)$), which is faster than the ion thermal speed ($v_{t,i} = 7.74 \times 10^2$) but

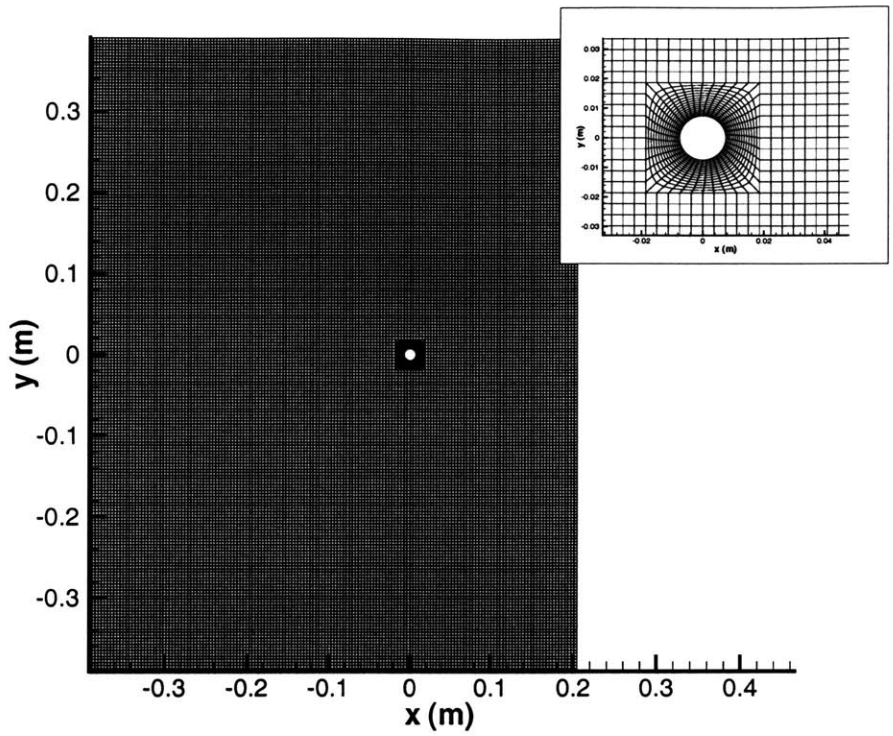

Figure 3-4: Computational Grid. In the small window, an enlarged view of the grid near the tether is shown

slower than the electron thermal speed ($v_{t,e} = 1.32 \times 10^5$). This condition is called "Mesothermal condition" (Section 3.2.6). In computation, ions are flowing into the domain from the left side with orbital speed, plus a small thermal motion. Electrons are assumed to have a Maxwellian type of distribution at the computational boundary. More details are given in following sections.

In Table 3.2, numerical parameters are indicated. With the concept of a superparticle, we can reduce the number of particles necessary in a computation without changing the plasma properties. In Table 3.2, "physical" parameters of the superparticle plasma are also indicated. Note that plasma parameters such as Debye length, plasma frequency, etc do not change. For example, plasma frequencies of a real plasma and a superparticle plasma are the same,

$$\sqrt{\frac{n_e q^2}{\epsilon_0 m}} = \sqrt{\frac{\hat{n}_e \hat{q}^2}{\epsilon_0 \hat{m}}} \tag{3.6}$$

Electric charge	(C)	$q = 1.6 \times 10^{-19}$
Electron mass	(kg)	$m = 9.1 \times 10^{-31}$
Ion mass	(kg)	$M = 2.67 \times 10^{-26}$
Electron Temperature	(eV)	$T_e = 0.1$
Ion Temperature	(eV)	$T_i = 0.1$
Electron density	(m^{-3})	$n_e = 10^{11}$
Ion density	(m^{-3})	$n_i = 10^{11}$
Debye Length	(m)	$\lambda_D = 7.44 \times 10^{-3}$
Geomagnetic field	(H)	$B = 0.3 \times 10^{-4}$
Larmor radius ($w = v_{t,i}$)	(m)	$r_c = 2.51 \times 10^{-8}$
Plasma frequency	(sec^{-1})	$\omega_p = 1.78 \times 10^7$
Electron cyclotron frequency	(sec^{-1})	$\omega_c = 5.27 \times 10^6$
Electron thermal speed	(m/sec)	$v_{t,e} = 1.32 \times 10^5$
Ion thermal speed	(m/sec)	$v_{t,i} = 7.74 \times 10^2$
Plasma flow speed (Tether orbital speed)	(m/sec)	$U_{tether} = 8.00 \times 10^3$
Tether potential	(eV)	$\phi_p = 25$
Radius of tether cross-section	(m)	$r_{tether} = \lambda_D = 7.44 \times 10^{-3}$

Table 3.1: Parameters

where a hat ($\hat{}$) here as well as in Table 3.2 refers to a numerical superparticle parameter. Computation was performed on a PC with a 1.2GHz Athlon processor and 1.0Gbyte memory. It would take about a week in order to obtain a converged solution due to the slow ions (See Appendix B). Once the ions establish a density profile according to the tether potential, it takes on average a couple of days for the electron density to converge.

In order to obtain a converged ion density profile, a *numerical times* method is used [40]. For the first few hundreds iterations, a large time step is used for the ion leapfrog method. Once the ion density is converged for this large timestep, the timestep is reset to the same value of the timestep used for electrons.

3.2.4 Quasi-neutrality Condition

The quasi-neutrality condition has been introduced by the author to improve the quantitative results of the PIC method [33]. The importance of the boundary condition stems from the fact that some electrons are absorbed by a tether. No ion is

Number of particles in a superparticle		$N_p = 200000$
Time Step	(sec)	$dt = 0.1 \sim 0.3 \times \pi/\omega_p$
Electric charge	(C)	$\hat{q} = q \times N_p$
Electron Temperature	(eV)	$\hat{T}_e = T_e \times N_p$
Ion Temperature	(eV)	$\hat{T}_i = T_i \times N_p$
Electron density	(m^{-3})	$\hat{n}_e = n_i/N_p$
Ion density	(m^{-3})	$\hat{n}_i = n_i/N_p$
Electron mass	(kg)	$\hat{m} = m \times N_p$
Ion mass	(kg)	$\hat{M} = M \times N_p$

Table 3.2: Numerical Parameters : a hat (^) indicates a numerical parameter used in a computation

absorbed by the tether, because of its very high positive potential. Figure 2-10 illustrates a conceptual cartoon of the overall flow of electrons and ions. Due to this partial absorption of electrons by the tether, the electric potential at the computational outside boundary needs to be non-zero (mostly positive except for the wake) with respect to the ambient plasma. Setting the outside boundary potential to be zero would eliminate the presheath effect which brings in more electrons from infinity to make up for the absorption, and it is known to require an unrealistic flux manipulation to keep the number of particles in the computation from being unstable [20]. In order to obtain a local potential at computational boundary points, the quasi-neutrality condition is applied. In the following, the quasi-neutrality condition is explained together with the formulae necessary for the implementation in the computation

3.2.5 Application of the quasi-neutrality condition

Let ϕ be the electric potential at an arbitrary point on the outside boundary. Assuming that ions are singly charged, we have the quasi-neutrality equation as

$$|n_e - n_i| \ll n_e. \tag{3.7}$$

In the computation, we use this condition in the form of

$$n_e = n_i. \tag{3.8}$$

However this does not allow us to transform Poisson's equation to Laplace's equation by equating the source term to zero, because the small difference $e(n_i - n_e)$ is divided by the small quantity ϵ_0, leaving $\nabla^2\phi$ indeterminate. As the plasma approximation claims, plasma tends to neutralize itself by imposing $n_e = n_i$. Therefore we impose the condition (3.8) on the outside boundary, and solve Poisson's equation inside that boundary only with a non-zero source term on its right-hand side.

In computation, equation (3.8) consists of four parts; incoming electron density n_e^{in}, incoming ion density n_i^{in}, outgoing electron density n_e^{out} and outgoing ion density n_i^{out}. The incoming particle densities, n_e^{in} and n_i^{in}, are assumed to be in an analytical form and given as functions of the local potential. Outgoing particle densities are calculated numerically (Sec. 3.2.12). Equation (3.8) is then rewritten as

$$n_e^{in}(\phi) + n_e^{out} = n_i^{in}(\phi) + n_i^{out}. \tag{3.9}$$

3.2.6 Meso-thermal Condition

Before we derive the formulae for the incoming particle densities, $n_e^{in}(\phi)$ and $n_i^{in}(\phi)$, we need to be aware of a condition called Meso-thermal condition. In LEO, an ED tether will be in an realistic orbiting condition under which the electron thermal speed, $v_{t,e}$, is much faster than the tether speed, U_{tether}, whereas the ion thermal speed, $v_{t,i}$, is much slower (Table 3.1).

$$v_{t,i} << U_{tether} << v_{t,e}. \tag{3.10}$$

In words, ions are traveling supersonically and electrons are traveling at a low subsonic speed. By "flowing plasma" in the following sections, we mean that the plasma is under the meso-thermal condition defined by (3.10). Incidentally, a "quiescent

plasma" simply means that $U_{tether} = 0$.

3.2.7 Incoming Electron Density, $n_e^{in}(\phi)$

At the computational outside boundary, electrons from infinity are assumed to have a Maxwellian distribution function for a quiescent plasma $U = 0$, and a shifted Maxwellian for a flowing plasma $U = U_{tether} \neq 0$.

$$f_e(\vec{w}) = n_\infty \left(\frac{m_e}{2\pi\kappa T_e}\right)^{3/2} \exp\left(-\frac{\frac{1}{2}m_e((w_x - U)^2 + w_y^2 + w_z^2) - e\phi}{\kappa T_e}\right) \tag{3.11}$$

The shifted Maxwellian ($U \neq 0$) is not exactly correct because the angle-average of a shifted Maxwellian is not a Maxwellian. However, under the meso-thermal condition (3.10) in which the electron thermal speed is many times larger than the flow speed (about 20 times for $T_e = 0.1(eV)$), the approximation may be good enough. As shown later, that the calculation of incoming electron density and flux for different U's shows a small dependence on U may support the use of the distribution function.

Incoming electron density is then obtained by integrating the distribution function (3.11) in velocity phase space. In integrating the function at a point where a local potential is positive, $\phi > 0$, certain electrons need to be excluded from the calculation because they can not exist, coming from infinity. These electrons are different in a 2-dimensional case (defined in x-y plane) and in a 3-dimensional case, characterized by

$$I : w_x^2 + w_y^2 \leq \frac{2e\phi}{m_e} \qquad \text{(2-D)} \tag{3.12}$$

$$I : w_x^2 + w_y^2 + w_z^2 \leq \frac{2e\phi}{m_e} \qquad \text{(3-D)} \tag{3.13}$$

The 3D case simply means that at a point of positive potential, ϕ, there exist only electrons which have a total energy more than the difference between that point and infinity. On the other hand, in the 2D case, even if an electron has a total energy larger than the difference between the electron position and infinity, the electron may not exist for the following reason.

The conservation of the electron total energy is given as

$$\frac{1}{2}m_e(w_x^2 + w_y^2 + w_z^2) - e\phi = E. \tag{3.14}$$

In the 2D case, there is no mechanism to change w_z. Therefore constants are the total energy, E, and w_z. Thus we can define a new constant, $E' \equiv E - \frac{1}{2}m_e w_z^2$ and get

$$\frac{1}{2}m_e(w_x^2 + w_y^2) - e\phi = E'. \tag{3.15}$$

In order for the electron to come from infinity, that is, to exist at infinity ($\phi = \phi_\infty = 0$), E' needs to be positive. Therefore electrons for which E' is negative can not exist at a point of positive potential, ϕ, and characterized by (3.12). If we reverse the trajectory of an electron with an enough total energy, $w_x^2 + w_y^2 + w_z^2 > \frac{2e\phi}{m_e}$ but not in x-y plane, $w_x^2 + w_y^2 < \frac{2e\phi}{m_e}$, from the positive potential point, the electron would wander around in x-y plane and would not go to infinity. If $w_z \neq 0$, the electron would go to $z = \pm\infty$, which is not defined as "infinity" because $\phi(x, y, \infty) \neq 0$ in the 2D problem.

The difference between the 2D and 3D calculations is seen in Figure 3-5, where electrons excluded in the calculation of the incoming electron density are indicated. It is seen clearly that more electrons are excluded in the 2D calculation than in the 3D calculation. In Figures 3-6 and 3-7, calculated incoming electron densities are shown. In each figure, four different plots for different sides of the computational grid (Figure 3-4) are shown. At each side, the effect of the plasma flow on the density calculation is different. At the ram side (right side, $\theta = \pi$ in the figure) the shifted distribution function (3.11) can be rewritten as

$$f_e(\vec{w}) = n_\infty \left(\frac{m_e}{2\pi\kappa T_e}\right)^{3/2} \exp\left(-\frac{\frac{1}{2}m_e((w_n - U\cos\theta)^2 + (w_t + U\sin\theta)^2 + w_z^2) - e\phi}{\kappa T_e}\right) \tag{3.16}$$

where w_n and w_t are the normal and tangential components of electron velocity at

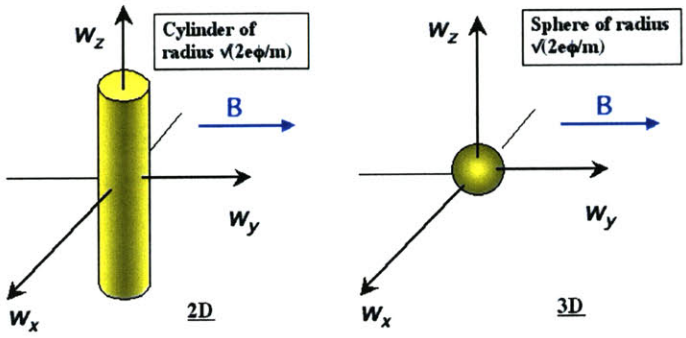

Figure 3-5: Electrons in velocity space. Electrons with velocities inside indicated regions, cylinder (2D,left) and sphere (3D,right), are excluded in the calculation of the OML current.

the boundary and are given as

$$\begin{aligned} w_n &= w_x \cos\theta + w_y \sin\theta \\ w_t &= -w_x \sin\theta + w_y \cos\theta \end{aligned}$$

Distribution functions in terms of (w_n, w_t, w_z) at other sides of the domain are obtained by substituting the value of θ indicated in the figure ($\theta = 0$ at the wake side, for example).

From Figures 3-6 and 3-7, it may be understood that the effect of the plasma flow on the distribution function is so small that the assumption to use the shifted Maxwellian distribution at the computational boundary may be justified. Changes in θ in equation (3.16) for a given U have the same effect on the distribution function as changes in U for a given θ. We see a little change in Figures 3-6 and 3-7 for different θ's, accordingly different U's. Another check on the effect of plasma flow is to run a simulation with a (non-shifted) Maxwellian distribution in the density and flux calculation only at the boundary (Inside the domain, PIC takes care of the flow

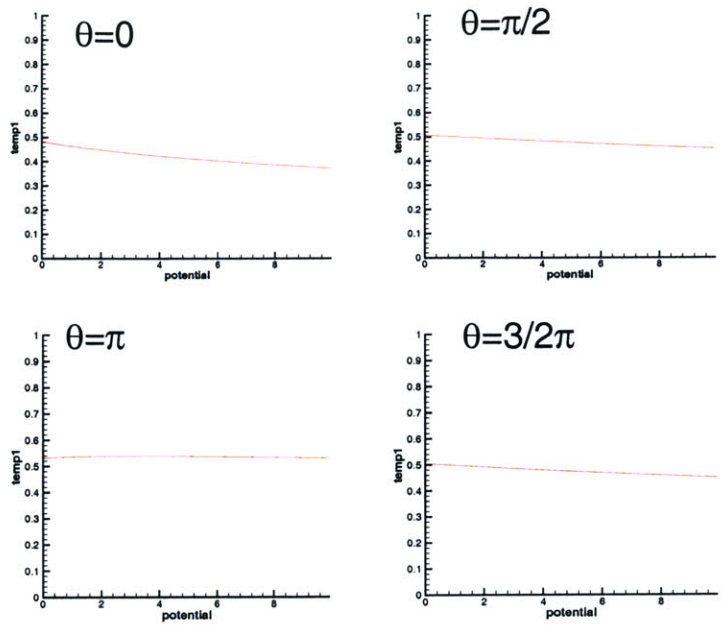

Figure 3-6: Incoming electron density in 2D calculation

effect.) And we found negligible difference.

3.2.8 2D. vs 3D.

While it is easy to understand when we should apply the flowing effect in the density calculation at the boundary, it is not so clear when, where and how the 3D effect should be applied. The application of interest here is a long thin bare tether, thus it is a geometrically 2D problem. However, in the presence of magnetic field, the motion of electrons is highly 3D. To see whether we can apply the 3D calculation in the geometrically 2D problem, let us consider a cylindrical probe (bare tether) in z-axis and magnetic field along the y-axis as shown in Figure 3-8(a). When the local potential is zero or negative, the calculation becomes trivial and both 2D and 3D calculations give rise to the same result. Here we consider a potential hump, $\phi > 0$, such as shown in Figure 3-8(b)

The essential way of distinguishing the 2D and 3D calculation is to check the behavior of an electron with enough total energy, $w_x^2 + w_y^2 + w_z^2 \geq \frac{2e\phi}{m_e}$, but not in the

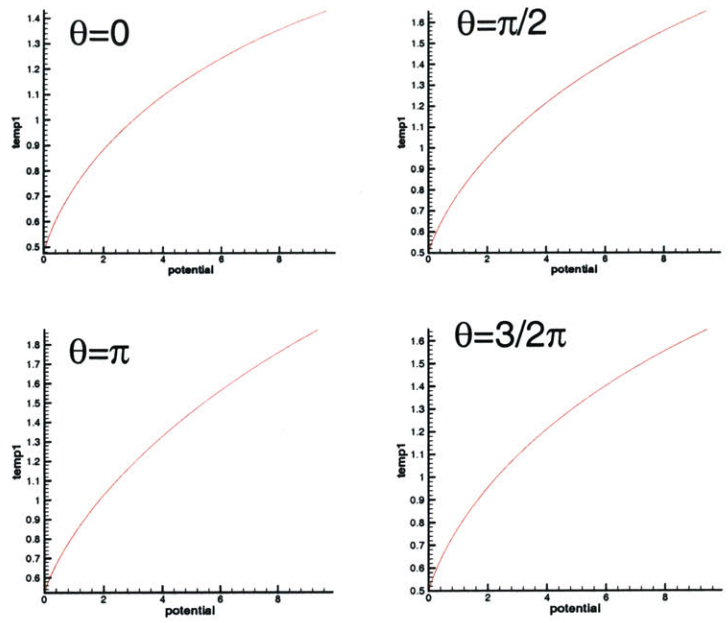

Figure 3-7: Incoming electron density in 3D calculation

x-y plane, $w_x^2 + w_y^2 < \frac{2e\phi}{m_e}$. The check is made following the Laframboise and Parker's argument [19]. We place a hypothetical electron with velocity (w_x, w_y, w_z) at a point of positive potential in the hump, and trace back the trajectory. (Actually, since we are considering a steady state, the direction in time is unimportant regarding the question whether it reaches infinity or not.) If the trajectory reaches infinity where $\phi(x, y) = 0$, we can count the electron in the density calculation.

In the presence of a magnetic field, however the criterion $w_x^2 + w_y^2 < \frac{2e\phi}{m_e}$ becomes irrelevant because the gyration motion cyclically interchange w_x and w_z. Then the question whether the 3D injection is valid or not becomes a question whether all electrons with $w_x^2 + w_y^2 + w_z^2 \geq \frac{2e\phi}{m_e}$, can reach infinity.

The answer depends on the flowing condition. Assume we have a potential hump which is large enough for the 3D calculation to be valid (See Section (3.2.10). The Laframboise and Parker way of checking is applied here. We consider a hypothetical electron in a potential hump and trace back the trajectory backwards in time. We check all electrons with $w_x^2 + w_y^2 + w_z^2 \geq \frac{2e\phi}{m_e}$ at the point and if ALL of them can be

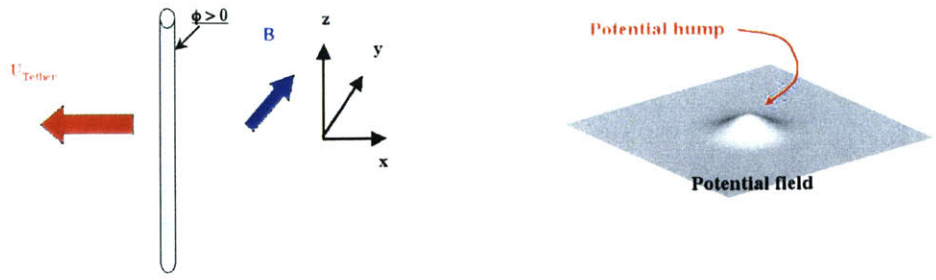

(a) Cylindrical tether and magnetic field (b) Potential hump

Figure 3-8: Cylindrical tether, magnetic field and potential hump

traced back to infinity, the 3D injection is considered valid.

In the absence of a plasma flow, i.e. if the potential hump is not moving, the answer is no. Since the electron motion is restricted around magnetic field and the electron keeps gyrating around them, in a potential hump larger than a Larmor radius, the electron could exit from the potential hump only along the magnetic field line. In order for this to happen, the electron needs enough kinetic energy in the y-direction. If the kinetic energy in y-direction is lower than the potential difference

$$\frac{1}{2}m_e w_y^2 < e\phi, \tag{3.17}$$

the electron is reflected back to inside the potential hump, and it keeps bouncing back and forth inside, never reaching infinity. Therefore the 3D calculation is not valid (except for the subset of electrons for which (3.17) is reversed).

In the presence of a plasma flow, i.e. if the potential hump is moving with respect to the plasma, the trapped electrons with sufficient kinetic energy, $w_x^2+w_y^2+w_z^2 \geq \frac{2e\phi}{m_e}$, but insufficient kinetic energy in y-direction, $w_y^2 < \frac{2e\phi}{m_e}$, may escape from the potential hump because of the flowing effects. As in the non-flowing case, such an electron would be bouncing back and forth along the magnetic field line and could not escape from the hump along the field line. However, due to the plasma flow, or equivalently due to

the motion of the plasma hump, electrons are constantly shifting in the x-direction. Therefore the electron can escape from the hump at the cost of the kinetic energy in the plane perpendicular to magnetic field,

$$\frac{1}{2}m_e(w_x^2 + w_z^2) \geq e\phi \tag{3.18}$$

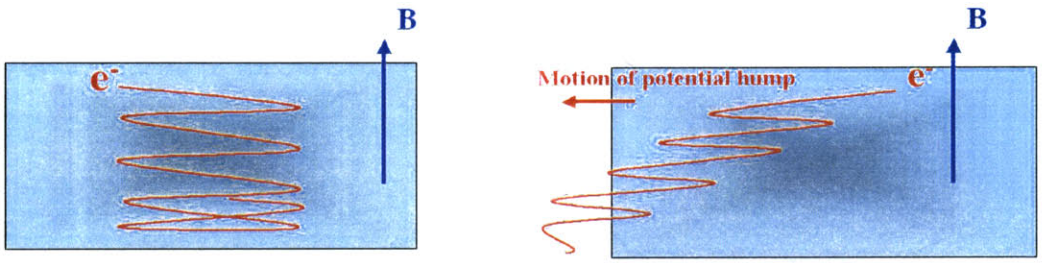

(a) Electron motion in a still potential hump

(b) Electron motion in a moving potential hump

Figure 3-9: Electron motion in a potential hump with magnetic field

In Figure 3-9, trajectories of such electrons are indicated. In Figure 3-9(a), an electron with insufficient kinetic energy in the y-direction bounces back and forth inside the potential hump, never being able to go out. In Figure 3-9(b), the potential hump is moving from right to left and a hypothetical electron placed inside the potential hump with sufficient kinetic energy but insufficient kinetic energy in the y-direction bounces back and forth in the y-direction and shifts in the x-direction due to the plasma flow. (Note that we are following the electron backwards in time. Therefore it shifts toward left.) Due to the shifting, the electron eventually finds the edge of the potential hump in the x-direction and escapes out to infinity. This is true for all electrons with a kinetic energy such that $w_x^2 + w_y^2 + w_z^2 \geq \frac{2e\phi}{m_e}$. Therefore the 3D injection at a local point of positive potential is valid in a geometrically 2D problem such as a cylindrical bare tether, if there is magnetic field in y-direction and the potential hump created by the tether is moving in the x-direction.

In order to illustrate this, several particle simulations are performed, in which a potential field with a potential hump is given as a constant and electrons with a Maxwellian distribution are injected from the boundary, where the local potential is kept to zero. Therefore no distinction is made between 2D and 3D at the boundary. The results are shown in Figure 3-10, where a fixed potential field with a hump and three electron density maps are shown. Simulations are started with no electrons in

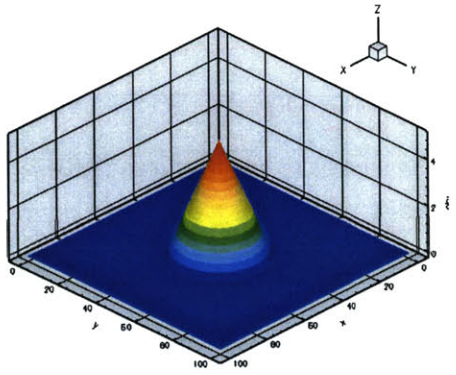

(a) Prescribed potential field

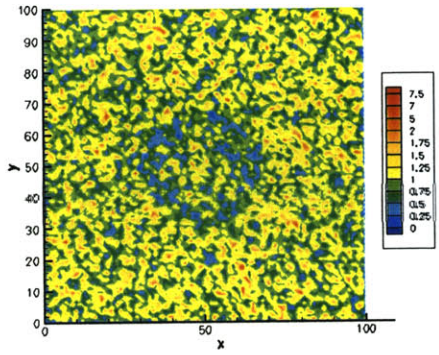

(b) With no flow and no magnetic field

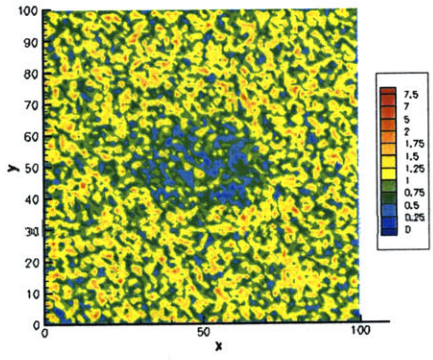

(c) With no flow and magnetic field

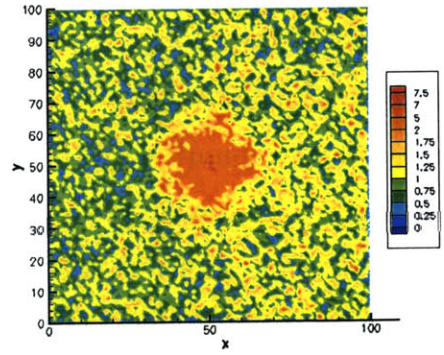

(d) With flow and magnetic field

Figure 3-10: Fixed potential hump and electron density

the domain and electrons are injected using a Maxwellian distribution. Each simulation was performed till the number of electrons in the domain converges. The cases are I) without flow and without magnetic field (2D), II) without flow and with

magnetic field, and III) with flow and with magnetic field (3D). In case I), electron density does not change a lot, as the 2D injection gives rise to a constant density of injected electrons. In case II), due to the absence of electrons with insufficient kinetic energy in the y-direction, $\frac{1}{2}m_e w_y^2 < e\phi$, inside the hump, the electron density shows the tendency of a 1D calculation and we notice decreases in the electron density. For the complete 1D calculation, the hump needs to be infinitely long in the x-direction so that an electron with any Larmor radius completes one gyration. Case III), electron density increases in the potential hump, in violation of the property shown in Section 4.1 for a purely 2D problem, in which case $n_e \leq n_\infty$ everywhere (equality if there is no absorption).

3.2.9 Criterion to use 3D injection at boundary

In order for the 3D injection at computational boundaries, magnetic effects needs to be so strong that any other effects do not hinder the interchange of w_x and w_z of electron motions, while the electron is in transit from infinity to the given point.

In our computation, a potential hump is created by a high bias electrodynamic tether. The electrostatic force by the tether may be strong enough to overwhelm the magnetic effect and the two-dimensional electrostatic effect prevails. And the 3D calculation becomes invalid. Therefore the computational boundary needs to be far enough so that the magnetic effect is still effective. The condition for magnetic effect to be dominant may be stated as follows; for the 3D calculation of electron injection at the computational boundary, w_x and w_z need to be interchangeable by the magnetic effect and an electron should complete at least one gyration before it enters the region where the 2D electrostatic effect is dominant. Typically a local potential at the computational boundary is around $\phi \sim \kappa T_e/e$. Thus the Larmor radius of an electron that has a thermal velocity at infinity is given as

$$r_L = \frac{mv_\perp}{eB} \tag{3.19}$$

where $v_\perp = \sqrt{\frac{2e\phi}{m} + v_T^2}$. This Larmor radius should be much smaller than the x-

component,L_x, of the distance from the tether to the computational boundary. This is equivalent to

$$B >> \frac{m_e\sqrt{\frac{2e\phi}{m_e} + v_T^2}}{eL_x} \tag{3.20}$$

In our simulation, the right-hand-side in (3.20) is calculated for $\phi = 0.1(V)$ and $v_T = 1.3 \times 10^5(m/sec)$ as

$$\text{RHS} \sim \frac{0.9 \times 10^{-30} \times \sqrt{(1.8 \times 10^5)^2 \times (1.3 \times 10^5)^2}}{1.6 \times 10^{-19} \times 0.4} \sim 0.03(G) \tag{3.21}$$

which is much lower than the nominal case ($G = 0.3(G)$).

3.2.10 Transition between 2D and 3D

The transition from 3D to 2D may be seen, again using the theory of Parker and Laframboise. We consider the transition in terms of the hypothetical electron. The potential hump given in Figure 3-8(b), is considered again. We put a hypothetical electron inside the hump, which has a sufficient total energy, $w_x^2 + w_y^2 + w_z^2 > e\phi$, and trace back its trajectory in time.

Now let us define a test electron which has a sufficient kinetic energy but insufficient perpendicular kinetic energy and is placed inside the hump. When magnetic effect is very strong so that the test electron can gyrate inside the hump, it finds the way out of the hump thanks to the drifting. For a given w_z, lowering magnetic field increases the Larmor radius of the test electron. If the size of the hump is not large enough to gyrate, the electron can not transfer kinetic energy from $\frac{1}{2}m_e w_z^2$ to $\frac{1}{2}m_e w_x^2$ due to the lack of space. This begins to happen to electrons with smaller $\frac{1}{2}m_e(w_x^2 + w_y^2)$ as they need more space to gyrate and transfer kinetic energy. Therefore, as B becomes smaller, electrons in a small cylindrical region in velocity space, $\frac{1}{2}m_e(w_x^2 + w_y^2) < e\phi_{smaller} < e\phi$, are excluded from the calculation. And $\phi_{smaller}$ approaches ϕ in the 2D limit.

In terms of plasma parameters, the "space" may be characterized by the plasma Debye length, d_D. The 3D limit is given when $d_D/r_L >> 1$, whereas the 2D limit

when $d_D/r_L << 1$. The presence of the probe inside the hump and its high potential, ϕ, also modifies the "space", replacing d_D by $\sim d_D\sqrt{\frac{e\phi}{\kappa T_e}}$.

3.2.11 Incoming ion density

The calculation of the incoming ion density in a flowing plasma is a bit more complicated, because we do not assume a Maxwellian distribution at a computational boundary due to the mesothermal condition. We only assume that ions have a Maxwellian distribution in the far upstream region before the presheath created by the highly biased tether cuts through and disturbs it. The ion distribution function used at the computational domain is derived as follows; we assume a one-dimensional motion of ions from the far upstream region (infinity) to the computational boundary. This neglects the kinetic energy $\frac{1}{2}m_e(w_y^2 + w_z^2)$ due to ion side deflection, and is a common approximation in hypersonic flows. Applying the 1-D energy conservation we may relate an ion velocity at infinity and at a boundary point as

$$\frac{1}{2}m_i w_x^2 \sim \frac{1}{2}m_i \hat{w}_x^2 + e\hat{\phi}_b \tag{3.22}$$

$$w_y \approx \hat{w}_y \tag{3.23}$$

$$w_z \approx \hat{w}_z \tag{3.24}$$

where the x-axis is taken in the tether's orbital direction, and $\hat{w}$'s are velocity components at a boundary point, w's velocity at infinity, $\hat{\phi}_b$ a boundary potential. Substituting equations (3.22) $\sim$ (3.24) into a shifted Maxwellian distribution function of ions at infinity

$$f_i(w) = n_\infty \left(\frac{m_i}{2\pi\kappa T_i}\right)^{3/2} \exp\left[-\frac{(w_x - U)^2 + w_y^2 + w_z^2}{v_{Ti}^2}\right] \tag{3.25}$$

we get

$$\hat{f}_i(w_i) = n_\infty \left(\frac{m_i}{2\pi\kappa T_i}\right)^{3/2} \exp\left[-\frac{\left(\sqrt{\hat{w}_x^2 + \frac{2e\hat{\phi}_b}{m_i}} - U\right)^2 + \hat{w}_y^2 + \hat{w}_z^2}{v_{Ti}^2}\right] \tag{3.26}$$

The incoming ion density is calculated numerically, using this distribution function.

In case of a quiescent plasma, the fact that no ions are absorbed by the tether and that the phenomenon is symmetric enable us to calculate the ion density at any point, $n_i = n_i^{in} + n_i^{out}$. Integrating the Maxwellian-Boltzmann distribution function in velocity phase space, we have the ion density as

$$n_i = n_\infty \exp\left(-\frac{e\phi}{\kappa T_i}\right) \tag{3.27}$$

Equation (3.27) is substituted in the quasi-neutrality condition (3.9). Therefore there is no need in calculating the outgoing ion density numerically.

3.2.12 Outgoing particle density

The outgoing electron density, n_e^{out} is still to be determined. This is calculated computationally with a lag of one time step by considering the outgoing flux, $\mathbf{\Gamma}$. The flux through the boundary is given by

$$\mathbf{\Gamma} = n_e^{out} v_e^{out} \tag{3.28}$$

where v_e^{out} is the flow velocity due to the outgoing electrons, that is, the average velocity normal to the boundary [34], which is calculated computationally as follows, As seen in Figure 3-11 during the period of one timestep dt, sampling all particles which go through the boundary cell surface (which has a width dx but is later taken to the limit $dx \to 0$) leads to particles' flux distribution function $wf(w)$. In order to derive a distribution function, we need to sample particles at an arbitrary moment during this time step. To do so, we consider the "probability" that a particle is *on* the

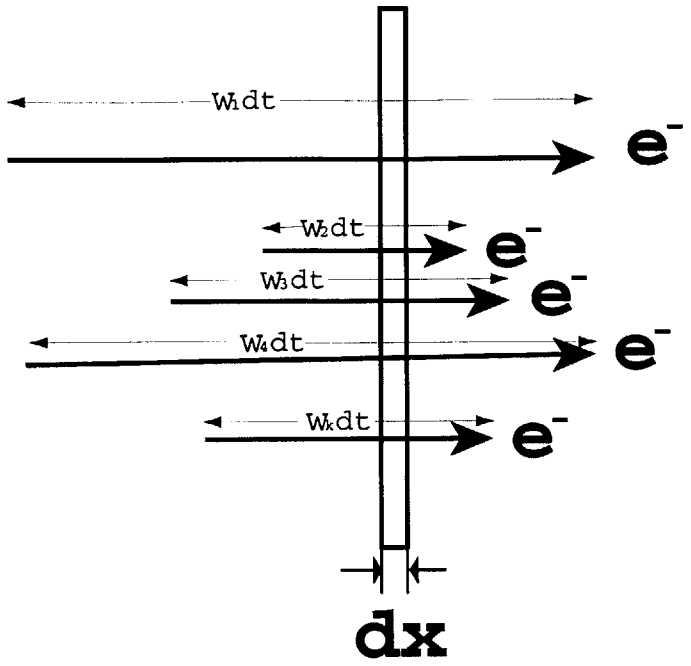

Figure 3-11: Conceptual picture at a boundary cell surface and outbound particles

boundary at the arbitrary moment during the timestep dt. For brevity, all particles' velocities, denoted by $w_i (i = 1 \sim k)$, have been projected on the normal to the surface ($w_i = \vec{w}_i \cdot \vec{n}$). In Figure 3-11, one particle which travels through the surface with a velocity w_i has the probability of being *on* the surface as $dx/w_i dt$. It can be also interpreted that there is a fraction "$dx/w_i dt$" (< 1) of all the crossing particles on the boundary at the moment. Therefore the average velocity is given by

$$\begin{aligned} \bar{v} &= \frac{\frac{dx}{w_1 dt} w_1 + \frac{dx}{w_2 dt} w_2 + \cdots + \frac{dx}{w_k dt} w_k}{\frac{dx}{w_1 dt} + \frac{dx}{w_2 dt} + \cdots + \frac{dx}{w_k dt}} \\ &= \frac{k}{\sum^k \frac{1}{w_i}} \end{aligned} \tag{3.29}$$

which is independent of dx. Trivially, we can take the limit of $dx \to 0$. Substituting the average velocity (3.28) and $\Gamma = k dt dS$ into

$$n_{e,i}^{out} = \frac{k}{\bar{v}\ dt\ dS} \tag{3.30}$$

we get the density of outgoing particles.

$$n_{e,i}^{out} = \frac{\sum^{k} \frac{1}{w_i}}{dt\ dS} \tag{3.31}$$

where dt is the timestep and dS is the area of the outside boundary. This completes the procedure for setting up the quasi-neutrality condition. The local potential, ϕ, is solved for numerically, for example, using a bisection method.

Technical Note

When an electron approaches the computational boundary and goes out of the domain, the normal component of velocity, w_n, to the boundary is calculated and used to calculate the density of outgoing electrons at the point.

In the 2-D (unmagnetized) case, an electron's trajectory is almost straight, because of the small electric field there, and it is rare to have infinitesimally small w_n at the boundary. On the other hand, In 3-D (magnetized) case, electrons are gyrating around the magnetic force line. Therefore, it is possible that an electron barely goes across the boundary giving $w_n \sim 0$.

When this happens, the electron density becomes very large, as $\frac{1}{w_n} \to \infty$,

$$n_e^{out} = \frac{\sum_i \frac{1}{w_{n,i}}}{dtdS} \to \infty. \tag{3.32}$$

In theory, a particle with $w_n = 0$ has to be counted as one and another with $w_n \neq 0$ as $\frac{1}{w_n dt}$. In order to avoid this, we apply a small but finite size to a particle ($dx \neq 0$), and rewrite equation (3.29) as

$$\bar{v} = \frac{\frac{dx}{w_1 dt+dx} w_1 + \frac{dx}{w_2 dt+dx} w_2 + \cdots + \frac{dx}{w_k dt+dx} w_k}{\frac{dx}{w_1 dt+dx} + \frac{dx}{w_2 dt+dx} + \cdots + \frac{dx}{w_k dt+dx}} \tag{3.33}$$

With equation (3.33), we can count a particle with $w_n = 0$ as $\frac{dx}{w_n dt+dx} = \frac{dx}{dx} = 1$.

And of course the contribution of this particle to the mean velocity is

$$\frac{dx}{w_n dt + dx} w_n = 0 \tag{3.34}$$

3.2.13 Incoming Particle Fluxes

Given the potential at the outside boundary, we are now ready to calculate how many electrons and ions are to be replenished into the domain at each timestep. The number of those particles is calculated by multiplying the flux by the timestep and the area of the outside boundary. The incoming electron flux $\Gamma_e^{in}(\phi)$ is calculated by integrating the electron distribution function (3.11) after multiplying a normal component of a particle velocity w_n (normal to the boundary surface).

$$\Gamma_e^{in}(\phi) = \underset{\text{Except for I}}{\iiint_{-\infty}^{\infty}} w_n f_e(\vec{w}) d\vec{w} \tag{3.35}$$

where I is defined by equation (3.13).

When there is no flow, the integral can be performed as

$$\begin{aligned} \Gamma_e^{in} &= \int_{-\infty}^{\infty}\int_{-\pi/2}^{\pi/2}\int_{\sqrt{e\phi/m_e}}^{\infty} n_\infty \left(\frac{m_e}{2\pi k T_e}\right)^{3/2} \exp\left(-\frac{\frac{1}{2}m_e(w^2+w_z^2) - e\phi}{kT_e}\right) w^2 \cos\theta dw d\theta dw_z \\ &= \frac{n_\infty \bar{c}_\infty}{4}\left\{\frac{2}{\sqrt{\pi}}\sqrt{\frac{e\phi}{kT_e}} + \exp\left(\frac{e\phi}{kT_e}\right)\operatorname{erfc}\sqrt{\frac{e\phi}{kT_e}}\right\} \end{aligned} \tag{3.36}$$

where $\bar{c}_\infty$ is the random thermal velocity given in equation (2.7). It should be noted that this is the same as equation (2.3), except for ϕ instead of ϕ_p.

Likewise, the incoming ion flux $\Gamma_i^{in}(\phi)$ is obtained by

$$\Gamma_i^{in}(\phi) = \iiint_{-\infty}^{\infty} w_n \hat{f}_i(\vec{w}) d\vec{w} \tag{3.37}$$

where $\hat{f}_i(\vec{w})$ is given by equation (3.26). At the ram side of the computational boundary, the assumption of one-dimensional motion of incoming ions simplifies equation

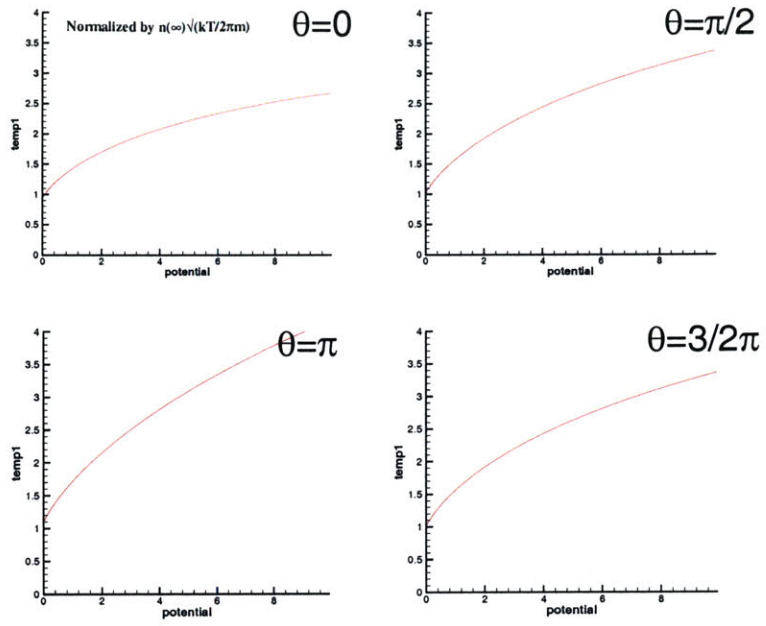

Figure 3-12: Incoming electron flux in a nonmagnetized plasma (2-D)

(3.37) to

$$\Gamma_i^{in} = U_{tether} n_\infty. \tag{3.38}$$

In the absence of a plasma flow, ions also have a Maxwellian distribution at the computational boundary. The flux is then given as

$$\begin{aligned} \Gamma_i^{in} &= \int_{-\infty}^{\infty}\int_{\pi/2}^{\pi/2}\int_{0}^{\infty} n_\infty \left(\frac{m_i}{2\pi k T_i}\right)^{3/2} \exp\left(-\frac{\frac{1}{2}m_i(w^2+w_z^2)+e\phi}{kT_i}\right) w^2 \cos\theta dw d\theta dw_z \\ &= n_\infty \left(\frac{kT_i}{2\pi m_i}\right)^{1/2} \exp\left(-\frac{e\phi}{kT_i}\right). \end{aligned} \tag{3.39}$$

Injection Method

$k_e = \Gamma_e^{in}\, \Delta t\, S$ electrons are injected at a local boundary point (or a cell in computation) where the local potential is ϕ. Here S is the area of a boundary cell where an electron is injected, and Δt is the time step. Electron velocity is chosen as explained by *Birdsall* [36], using a random number generator. The distribution created at the local point by the injected electrons is not a velocity distribution, $f_e(\vec{w})$, but a flux

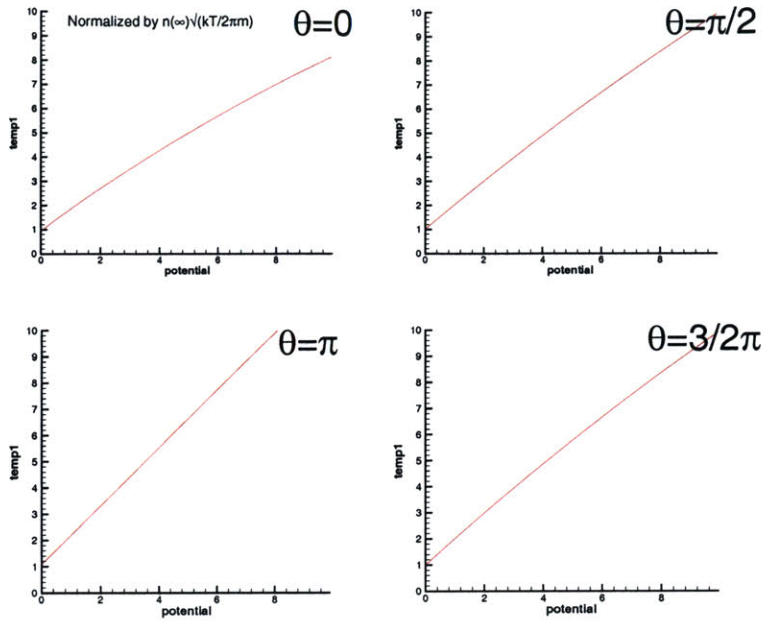

Figure 3-13: Incoming electron flux in a magnetized plasma (3-D)

distribution $w_n f_e(\vec{w})$, where w_n is the normal component of an injected particle's velocity, since we are injecting particles during a finite timestep Δt.

In the case of a flowing plasma, the distribution function is not a Maxwellian any more. To create the shifted Maxwellian distribution (3.11) at the injection point, the rejection method is used [17]

3.2.14 Trapped Electrons outside the Computational Domain

The novelty of the PIC method is its capability of capturing time-dependent particle-field interactions in a plasma. Particle-field interactions entail the gain/loss of particle total energy. Accordingly, there exist many particles, mostly electrons, that have lost some total energy to the field and wander around with negative total energy. A particle with negative total energy is called a "trapped particle". A trapped electron can travel in a region where the local potential is positive so that the velocity has some value, i.e. $\frac{m}{2}w^2 = E + e\phi > 0$ even if the total energy $E < 0$. The region where the local potential is positive is not only the sheath near the tether, but also

the presheath outside the sheath is defined as having a positive local potential.

Trapped electrons, defined as having a negative total energy, are still able to go out of the computational domain, since at the computational outside boundary the local potential is mostly positive (except in the wake). However these trapped electrons can not reach infinity where the electric potential is defined to be zero. Therefore all the trapped electrons wander around inside the presheath region and eventually come back to the computational domain. As an assumption, trapped electrons do not lose or gain total energy outside the computational domain. In order to incorporate the return of trapped electrons with the same total energy, in our model, we simply reinject a trapped electron at the same place where it leaves the domain and immediately after it leaves, with a randomized velocity but the same total energy.

3.2.15 Analytical Move

In the immediate vicinity of a tether, the electric potential is very high due to the high bias on the tether. Accordingly the velocity of electrons traveling in this region becomes very fast, leading to a numerical error within one timestep. In Fig. 3-14, two electron trajectories are indicated with a cross-section of tether (in the center) and several equipotential lines. The straight trajectory represents an electron trajectory in one timestep. The other curved trajectory is the real trajectory that the electron should take in the axisymmetric large electric field. In order to avoid the numerical error, we introduce the analytical motion of electrons in a circular region within which a local potential is more than $5eV$ (ion ram energy), actually using $10eV$ in computation. Within this region, the particle's total energy and angular momentum are assumed to be conserved. This assumption is readily justified by the circular equipotentials in the region. The potential profile is assumed as an analytical, axisymmetric form, which is a function of the distance from the center of the tether, $(r_p < r < r_l)$,

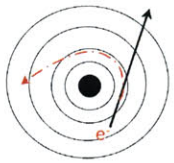

Figure 3-14: Numerical error near an ED tether

where r_p is the radius of the tether, r_l the outer boundary of the analytical region.

As an approximation, we solve Laplace's equation in order to obtain the analytical function in the domain. Obviously this contradicts reality, in which electron density in the domain can not be negligible. However, as explained in Section 2.2.3, the high bias on the tether makes the space charge effect negligible. The term $\sim 1/r^2$ obtained by solving Poisson's equation with the source term contributes little to the solution. Thus the solution obtained from Laplace's equation can simplify the problem without changing the plasma behavior significantly. Given the boundary conditions, we can solve Laplace's equation and obtain the potential in the analytical region as

$$\phi(r) = \frac{\phi_p \log \frac{r}{r_l} + \phi_l \log \frac{r_p}{r}}{\log \frac{r_p}{r_l}} \tag{3.40}$$

From two conservation laws, we have the conservation of angular momentum

$$mr^2\dot{\theta} = J \tag{3.41}$$

and the conservation of total energy

$$\frac{m}{2}\left\{\dot{r}^2 + (r\dot{\theta})^2\right\} - e\phi(r) = E \tag{3.42}$$

Substituting (3.41) into (3.42), we have

$$\dot{r} = \pm\sqrt{\frac{2}{m}(E + e\phi) - \frac{J^2}{m^2r^2}} \tag{3.43}$$

The sign should be chosen depending on the sense of the particle's radial motion. Separating terms of only r and t, we obtain an ODE

$$\pm\frac{dr}{\sqrt{\frac{2e\phi(r)}{m} - \frac{J^2}{m^2r^2}}} = dt \tag{3.44}$$

By integrating, we obtain the radial distance that a particle travels as a function of time, or vice versa.

Before performing the integral, we need to find out the periapsis point, r_m, where the radicand of the LHS in (3.44) becomes zero. r_m is obtained by solving

$$\sqrt{\frac{2e\phi(r_m)}{m} - \frac{J^2}{m^2 r_m^2}} = 0. \tag{3.45}$$

From (3.45), the periapsis point r_m is obtained as a function of angular momentum, J, and the local potential at the outer boundary of the analytical domain, $r = r_l$. In our code, this is done numerically at the beginning of the computation for a certain range of J and ϕ_l and stored in memory. For a known r_m, if $r_m < r_p$, the particle is absorbed by the tether. If $r_m > r_p$, it flies by the tether.

After a given period of time, Δt, we can find the new particle position by integrating equation (3.44),

$$\pm \int_{r_0}^{r_{new}} \frac{dr}{\sqrt{\frac{2e\phi(r)}{m} - \frac{J^2}{m^2 r^2}}} = \Delta t \tag{3.46}$$

where r_0 is an old position of a particle and r_{new} is the new position that we seek to solve. A note of caution should be made here. During the period of time, if the particle flies through the periapsis point, the denominator of the integrand in equation (3.46) becomes zero. In the very vicinity of the periapsis point, we can expand the denominator in a Taylor series and obtain

$$\sqrt{\frac{2e\phi(r)}{m} - \frac{J^2}{m^2 r^2}} \sim \sqrt{B\sigma} \tag{3.47}$$

where

$$B = \frac{2q}{m \log \frac{r_p}{r_l}} (\phi_p - \phi_l) + \frac{2J^2}{r_m^2 m^2} \tag{3.48}$$

$$r = r_m(1 + \sigma) \quad (\sigma \ll 1) \tag{3.49}$$

Therefore the integrand behaves as $1/\sqrt{r}$ at the periapsis and the integral converges. In computation, this part should be done analytically.

Once we know r_{new}, we can calculate the angle, $\Delta\theta$, that the particle subtends

over the time period, Δt.

$$\Delta\theta = \int_{r_0}^{r_{new}} \frac{J}{r^2 m}\frac{dt}{dr}dr \tag{3.50}$$

$$= \int_{r_0}^{r_{new}} \frac{Jdr}{r^2 m\sqrt{\frac{2e\phi(r)}{m} - \frac{J^2}{m^2 r^2}}} \tag{3.51}$$

which gives a new angle for the particle, θ_{new}.

From equations (3.41) and (3.42) with r_{new} and θ_{new}, we get $\dot{r}$ and $\dot{\theta}$ from which we know the new velocity of the particle.

Finally, in a PIC simulation, a Leapfrog method is used to advance a particle's position and velocity in phase space. In this method, position and velocity are defined at time steps which are shifted by $\frac{1}{2}\Delta t$ from each other. In the analytical region, position and velocity are defined at the same time. Therefore appropriate shifting of variables is required when a particle enters/leaves the region.

3.2.16 Sub-Cycling

There is another numerical error inevitable in a PIC method. The PIC method uses a standard leapfrog method for updating particle position in phase space. The standard leapfrog method is not limited by the CFL condition for numerical stability. but numerical errors arise due to the propagation of small errors, such as truncation, in each time step. The upper limit of the time step is then defined so that the truncation error does not increase rapidly. The threshold is given as $\Delta t = \sqrt{2} \times \frac{2\pi}{\omega_p}$ for the leapfrog method.

In our computation, $\Delta t = \sqrt{2} \times \frac{2\pi}{\omega_p}$ is quite large because of errors described as follows. As shown in Fig. 3-15, when an electron is seeing a positive second derivative of potential, $\nabla^2\phi$ in its direction of motion, it loses total energy and accumulates an error, whereas it gains total energy when it sees a negative $\nabla^2\phi$. In order to reduce the error associated with potential humps and ditches, sub-cycling is introduced in the leapfrog method. In sub-cycling, one timestep is divided into several sub-time steps within which an electron travels less than one cell size.

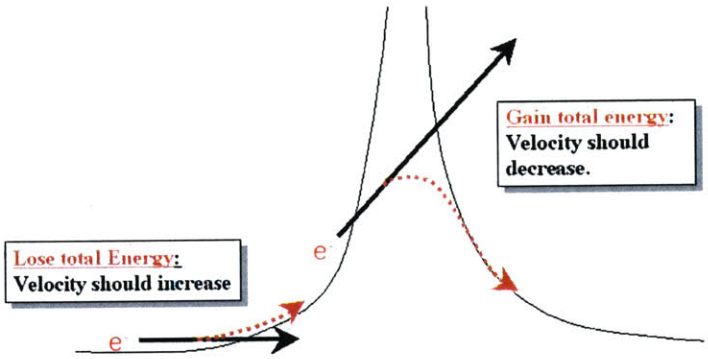

Figure 3-15: Error within one timestep

Chapter 4

Results and Pre-Flight Predictions

In this chapter, we start with a brief review of my Master thesis [33] which deals with current collection to a cylindrical probe in a quiescent nonmagnetized plasma. A previous solution exists for this case, and the comparison is made in order to verify the PIC method applied to the calculation of current collection to the probe. Next, a quiescent magnetized case and a flowing unmagnetized case are considered. There are no complete computational results available for these cases. A discussion is given of the dependence of the current collection on the magnetic field in the absence of plasma flow. And some speculation on the flowing effect on the current collection without the magnetic field is presented based on some preliminary results from our simulations. Finally current collection in a flowing magnetized plasma is present for the arbitrarily chosen nominal case.

4.1 Quiescent Unmagnetized Plasma : Code Verification

As the first prototype code of a PIC method to calculate current collection to a positively biased cylindrical probe, a case in a quiescent unmagnetized plasma is considered. The work is reported in detailed elsewhere [33]. Here we look at the result and its comparison with the previous solution available in literature [18]. Since

it is symmetric and the very high bias of the probe means that it absorbs no ions, we can apply a Maxwellian distribution for ions at any point in the computational domain. Therefore the quasi-neutrality condition (3.9) becomes

$$n_e^{in}(\phi) + n_e^{out} = n_i(\phi) \tag{4.1}$$

and n_i is given by (3.27).

Another thing to note is that the ion density is independent of the ion mass, m_i. Therefore, the mass ratio, m_i/m_i, is unimportant. In fact, the work by *Laframboise* [18], which gives the previous solution, did not specify the mass ratio.

In our PIC model, four different Debye ratios, defined by r_p/d_D, are considered. Those ratios are chosen as 0.5, 1, 2 and 5, which correspond to current collections in and near the OML regime.

Current Collection

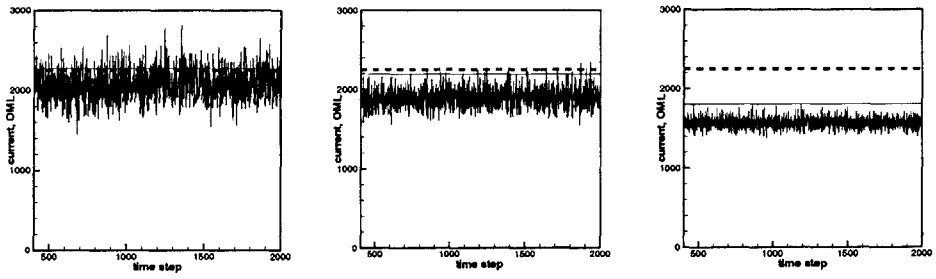

Figure 4-1: Current Collections in a quiescent unmagnetized plasma, Laframboise solutions (solid) and OML (dash) [33]

In Figure 4-1, current collections observed in simulation are shown. All results show current just below the Laframboise solutions. The plasma parameters are set constant for all cases and only the tether radius was varied. The comparison with the Laframboise solution is shown in Figure 4-2. An extra case well inside the OML regime, $d_D/r_p = 0.5$, is added in the figure. It may be seen that all cases give a good quantitative approximation to current collection within $5 \sim 8\%$.

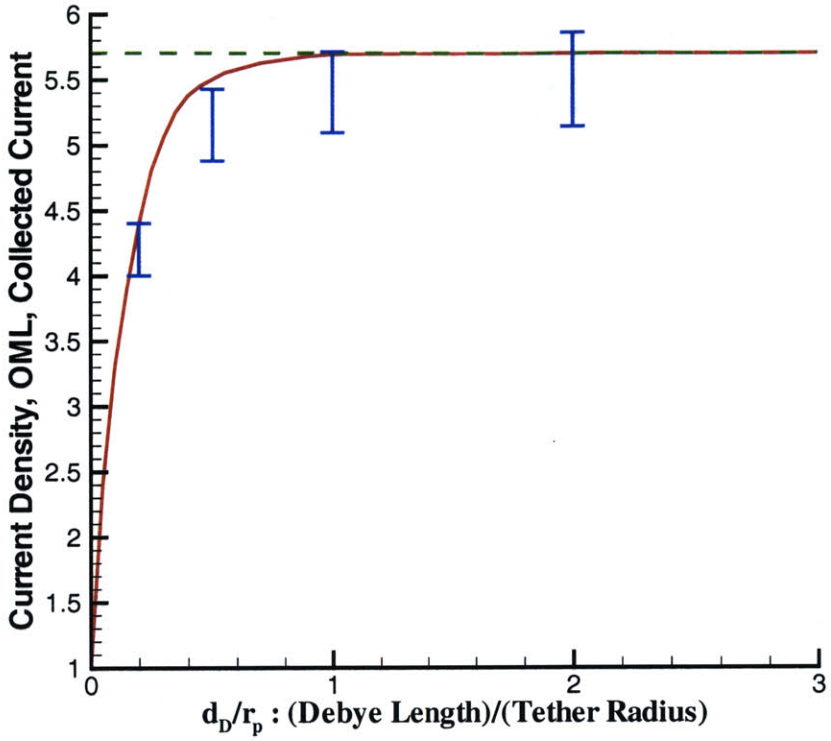

Figure 4-2: Current Collections in a quiescent unmagnetized plasma, Laframboise solutions (solid) and OML (dash)

Potential Maps

Let us look at some potential maps observed in the simulations. *Sanmartín and Estes* [13] (See also Section 2.2.3) gave a graphical criterion for a potential profile to provide a current collection in the OML regime. In Figure 4-3, potential maps for different Debye ratios are shown to the same scale. Non-physical numbers are used. The legend indicates that the electron temperature $T_e = 100$ and the probe potential $\phi_p = 25 \times T_e$, where Boltzmann constant,κ, and electric charge, e, are set to unity [36]. The potential profile averaged over all angles is plotted versus the abscissa, $(r_p/r)^2\phi_p$ in Figure 4-4. When the current collection is in the OML regime the potential profile should be above the diagonal line for all r. For the potential profile in the OML regime in Figure 4-4(a), it is seen that the potential profile is above the diagonal line

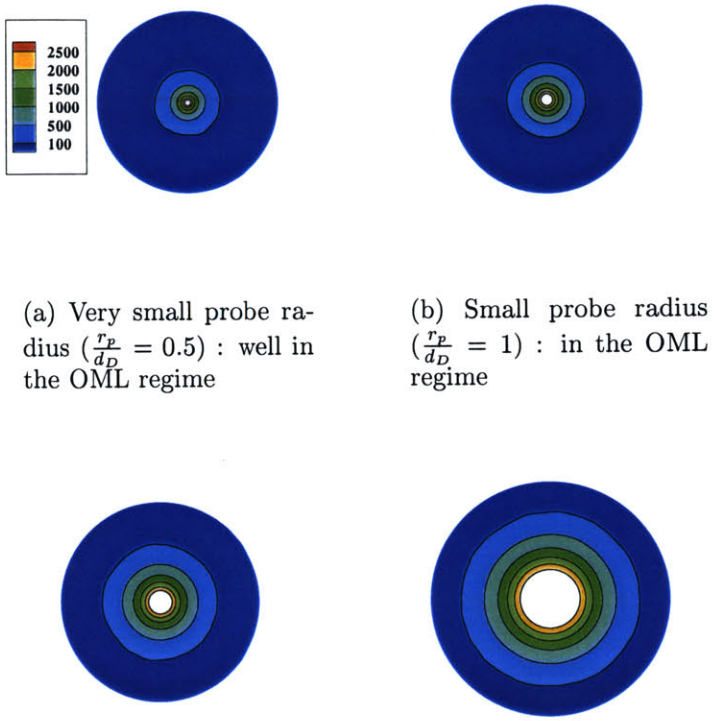

(a) Very small probe radius ($\frac{r_p}{d_D} = 0.5$) : well in the OML regime

(b) Small probe radius ($\frac{r_p}{d_D} = 1$) : in the OML regime

(c) Medium probe radius ($\frac{r_p}{d_D} = 2$) : near the OML regime

(d) Large probe radius ($\frac{r_p}{d_D} = 5$) : out of the OML regime

Figure 4-3: Potential maps in and out of the OML regime in a quiescent unmagnetized plasma. r_p is the tether radius and d_D is the Debye length. All figures are shown to the same scale. $T_e = 100$ and $\phi_p = 25T_e$.

for all r. Figure 4-4(b) corresponds to a transition point where the current collection shifts from the inside of the OML regime to the outside. The collected current in the simulation is a few percent below the Laframboise solution. The error may be considered due to the potential below the diagonal line. As it goes out of the OML regime, the potential profiles clearly go below the diagonal line (Figures (c) and (d)). The more it is below the diagonal line, the farther out of the OML regime it is. This confirms that the quantitative results such as current collection are consistent with the potential profile and the accuracy of the current collection may be trusted.

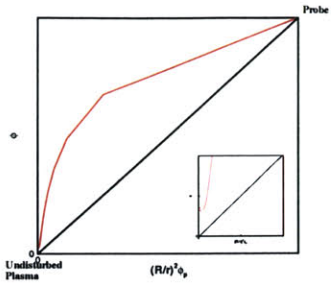

(a) Very small probe radius ($\frac{r_p}{d_D} = 0.5$) : well in the OML regime

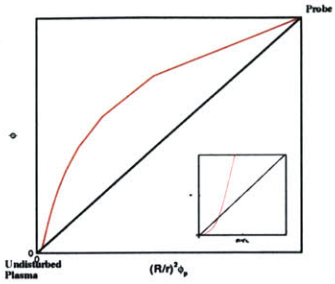

(b) Small probe radius ($\frac{r_p}{d_D} = 1$) : in the OML regime

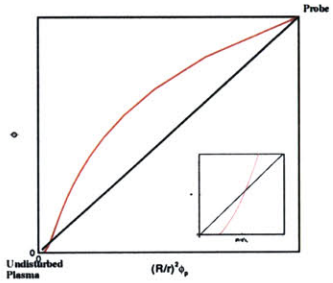

(c) Medium probe radius ($\frac{r_p}{d_D} = 2$) : near the OML regime

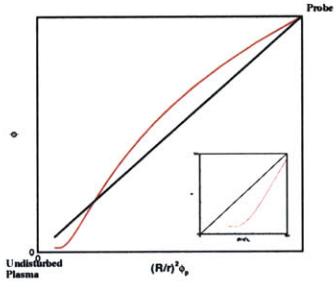

(d) Large probe radius ($\frac{r_p}{d_D} = 5$) : out of the OML regime

Figure 4-4: Potential Profiles with the abscissa as $(r_p/r)^2\phi_p$, where ϕ_p is a probe potential. Potential $\phi(r)$ should be over the diagonal line over all r. In a smaller window, an enlarged plot near the origin is shown.

4.2 Quiescent Magnetized Plasma

Magnetic effects break the symmetry and electron motions are restricted along magnetic field. In order to derive the current collection, canonical momentum conservation is used [9]. When the ratio of probe radius, r_p, to electron gyro-radius, r_L, is small, electrons reaching a highly positive probe have changes in v_z (velocity along the probe) much smaller than changes in the x-y plane. This makes 3D effects on collection negligible.

Total energy of an electron is given as

$$\frac{1}{2}m_e w_\perp^2 + \frac{1}{2}m_e w_z^2 = e\phi + E \tag{4.2}$$

where $w_\perp$ is the velocity in the plane perpendicular to the probe. Canonical momentum along z is given as

$$m_e w_z - eA_z = \text{constant} \tag{4.3}$$

We can differentiate (4.3) and obtain the relation between the velocity change in v_z and the distance that an electron can reach across the magnetic field as it approaches from infinity.

$$\Delta w_z = -v_{Te}\frac{\Delta x}{r_L} \tag{4.4}$$

where $r_L \equiv \frac{v_{Te}}{\omega_{ce}}$. Substituting into (4.2), we get

$$\frac{1}{2}m_e w_\perp^2 + \frac{1}{2}m_e(w_{z\infty} + \Delta w_z)^2 = e\phi + E \tag{4.5}$$

$$\frac{1}{2}m_e w_\perp^2 + \frac{1}{2}m_e(w_{z\infty} - v_{Te}\frac{\Delta x}{r_L})^2 = e\phi + E \tag{4.6}$$

where $w_{z\infty} \sim v_{Te}$. Since $e\phi_p >> \kappa T_e$,

$$\frac{1}{2}m_e w_\perp^2 + \frac{1}{2}m_e\frac{\kappa T_e}{m_e}\left(\frac{\Delta x}{r_L}\right)^2 \sim e\phi_p. \tag{4.7}$$

Orbits reaching the probe are characterized by $\Delta x < r_p\sqrt{\frac{e\phi_p}{\kappa T_e}}$. Therefore, we get

$$\frac{1}{2}m_e w_\perp^2 + \frac{1}{2}\left(\frac{r_p}{r_L}\right)^2 e\phi_p \sim e\phi_p. \tag{4.8}$$

When the probe radius is much smaller than the gyroradius, $(r_p/r_L)^2 << 1$, (4.8) becomes $\frac{1}{2}m_e w_\perp^2 \sim e\phi_p$, indicating that the 2D effect is dominant in the electron acceleration and the current collection is given by the 2D OML. When the probe is much larger than the Larmor radius, $(r_p/r_L)^2 >> 1$, we have $\frac{1}{2}m_e w_z^2 \sim e\phi_p$. From

(4.4), we have

$$e\phi_p \sim \frac{1}{2}m_e(w_{z\infty} + \Delta w_z)^2 \sim \frac{1}{2}m_e v_{Te}^2 \left(\frac{\Delta x}{r_L}\right)^2 >> \frac{1}{2}m_e v_{Te}^2 \left(\frac{\Delta x}{r_p}\right)^2. \qquad (4.9)$$

This leads to $\Delta x << r_p\sqrt{e\phi_p/\kappa T_e}$, meaning that fewer electrons can reach the probe. Therefore, the current collection becomes lower than the 2D OML. The transition between these two is unclear. To summarize, the important conclusion are; (a) In the absence of flow, B reduces the current collection. This is consistent with our discussion of 1-D trapping in Section 3.2.7. (b) The effect is relatively weak, and only shows up when B is so strong that $r_L \sim r_p$.

4.3 Flowing Unmagnetized Plasma

When there is a plasma flow but no magnetic field, the plasma behavior changes drastically and we can not obtain a steady state solution any more. Under the mesothermal condition of interest, scattering of ions by the potential due to the high positive bias on the probe results in ion density greater than that of infinity in some large upstream region (Figure 4-5). On the other hand, due to the 2D motion in the absence of magnetic field, electrons do not increase in density in order that the plasma maintain the quasi-neutrality at the ion peak density. Because of the electron absorption by the probe, the nearly isotropic electrons should even decrease in density.

Attempting to increase the electron density, plasma traps electrons in the presheath region by particle-field fluctuations. Trapped electrons provide the source of extra electrons in the presheath and contribute to the higher current collection. There are no definite computed results on this.

In our computations we observed a continuous potential increase, by doing which a plasma is apparently trying to trap more electrons. Associated particle-field fluctuations were also observed at a fraction of plasma frequency at infinity. It may be speculated that in reality the particle-field interaction takes place at a longer wave-length because of the very low electron temperature. The size of computational

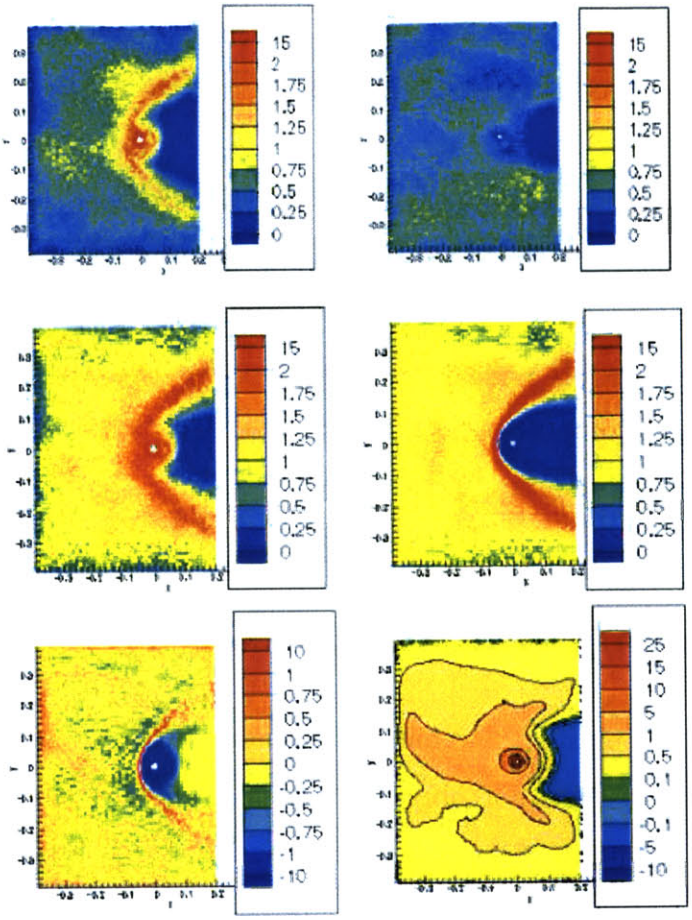

Figure 4-5: Instantaneous field quantities in a flowing unmagnetized plasma: (Top Left) Trapped electron density, (Top Right) Free electron density, (Middle Left) Electron density, (Middle Right) Ion Density, (Bottom Left) Net Charge Density and (Bottom Right) Potential.

domain is not large enough to accommodate such an interaction. Due to the lack of space and due to the necessity of trapping electrons, plasmas in the simulation force probably unrealistic oscillations and create illegimate electron trapping.

In Figure 4-5, instantaneous plots of field quantities are shown. At the top left, the density of trapped electrons defined as having a negative total energy is plotted. It is seen that there are many trapped electrons where ion density is increased due to the scattering by the large probe potential. The population of trapped electrons is also seen everywhere in the computational domain except for the wake.

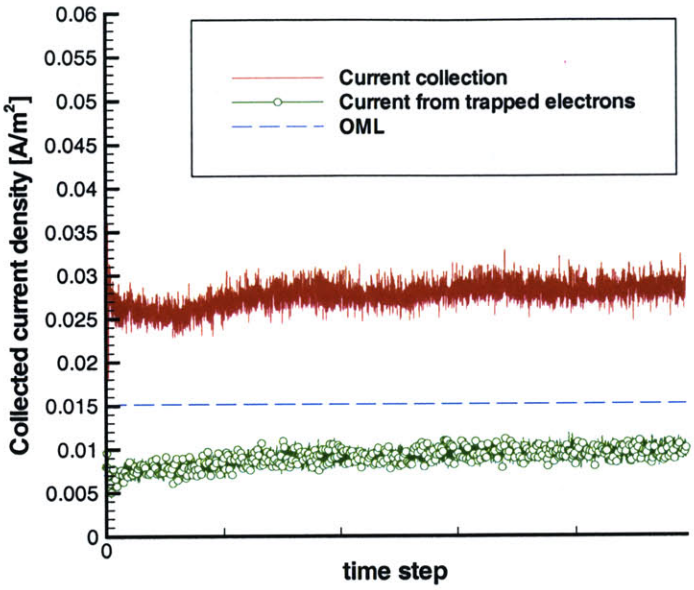

Figure 4-6: Current collection observed in computation. Trapped electrons contribute the excess current over the 2D OML.

In Figure 4-6, current collection observed in the computation is plotted. The collected current turned out to be more than the 2D OML. The current contribution by trapped electrons is also indicated. It is seen that the excess current over the 2D OML is due to the trapped electrons. In order to quiet the plasma, electrons are trapped in a still unknown way and increases in density. The trapped electrons also contribute to current collection. This contribution seems to enhance the current collection over the 2D OML current.

4.4 Flowing Magnetized Plasma

The main purpose of our work is the pre-flight prediction of current collection to the NASA Proseds electrodynamic tether experiment, which would be launched Fall 2002. In the rest of this chapter, I show the results from a nominal case and in the next chapter results from several simulations with different plasma parameters to

Magnetic field	(G)	$B = 0.3$
Tether potential	(V)	$\phi_p = 25$
Plasma density	(m^{-3})	$n_e = 10^{-11}$
Tether radius	(mm)	$d = 7.44$
(Tether radius)/(Debye length)		$\frac{d}{d_D} = 1$
Electron Temperature	(eV)	$T_e = 0.1$
Ion Temperature	(eV)	$T_i = 0.1$
Angle of the tether to its motion	(deg)	$\theta = 90$

Table 4.1: Plasma parameters for the nominal case

Case 1	Magnetic field	(G)	$B = 0.1$
Case 2	Magnetic field	(G)	$B = 0.6$
Case 3	Tether potential	(eV)	$\phi_p = 10$
Case 4	Tether potential	(eV)	$\phi_p = 100$
Case 5	(Tether radius)/(Debye length)		$\frac{d}{d_D} = 0.3$
Case 6	(Tether radius)/(Debye length)		$\frac{d}{d_D} = 3$
Case 7	(Tether radius)/(Debye length)		$\frac{d}{d_D} = 10$
Case 8	Electron Temperature	(eV)	$T_e = 0.05$
Case 9	Electron Temperature	(eV)	$T_e = 0.2$
Case 10	Ion Temperature	(eV)	$T_i = 0.05$
Case 11	Ion Temperature	(eV)	$T_i = 0.2$
Case 12	Angle of the tether to its motion	(deg)	$\theta = 60$

Table 4.2: Other cases: plasma parameters to change from the nominal case

make comparisons among them. We have decided on a nominal case, and changed one parameter for each case. The nominal case is defined in Table 4.1. All the other cases are set by changing one parameter from the nominal case (Table 4.2). And also as a special case, two parameters are changed at the same time in order to see the combined effects of the parameters (Table 4.3). Table 4.4 shows the various cases in terms of the relevant non-dimensional parameters.

Case 13	Case 3 & Case 8	$\phi_p = 10(eV)$ & $T_e = 0.05(eV)$
Case 14	Case 3 & Case 9	$\phi_p = 10(eV)$ & $T_e = 0.2(eV)$
Case 15		$\phi_p = 100(eV)$ & $\frac{d}{d_D} = 0.1$

Table 4.3: Combined cases

	$\frac{d}{d_D}$	$\frac{r_L}{d_D}$	$\frac{e\phi_p}{\frac{1}{2}m_i U_{tether}^2}$	$\frac{kT_e}{\frac{1}{2}m_i U_{tether}^2}$
Nominal	1	3.5	5	0.02
Case 1	1	**10.5**	5	0.02
Case 2	1	**1.75**	5	0.02
Case 3	1	3.5	**2**	0.02
Case 4	1	3.5	**20**	0.02
Case 5	**0.3**	3.5	5	0.02
Case 6	**3**	3.5	5	0.02
Case 7	**10**	3.5	5	0.02
Case 8	**1.4142**	3.5	5	**0.01**
Case 9	**0.7071**	3.5	5	**0.04**
Case 10	1	3.5	5	0.02
Case 11	1	3.5	5	0.02
Case 12	1	3.5	**6.25**	**0.025**
Case 13	**1.4142**	3.5	**2**	**0.01**
Case 14	**0.7071**	3.5	**2**	**0.04**
Case 15	**0.1**	3.5	**20**	0.02

Table 4.4: Parametric comparison : d is tether radius, d_D Debye length, r_L Larmor radius, ϕ_p tether potential, U_{tether} ion ram speed.

4.5 Results from Computations

In this section, we look at the results of the nominal case from our computations. First, several field quantities such as electron density, ion density, net charge and potential are examined. Characteristics of those quantities are discussed in relation with plasma parameters. Next, current collection is shown, followed by the detailed examination of individual particle behaviors.

The nominal case is defined in Table 4.1. We use this case as a starting point and change one parameter for another case for the purpose of comparison in the next chapter. The choice of parameters in the nominal case is arbitrary, although each parameter represents a typical value that an ED tether operated in LEO will encounter, except for the tether potential which at its peak will be much higher than $25(eV)$.

4.5.1 Ion density

In Figure 4-7, the instantaneous ion density in the nominal case is shown. It is normalized by the density at infinity, n_∞. Even though it is instantaneous, throughout a computation after the convergence, the changes in ion density are so small that Figure 4-7 is good enough to discuss average ion density profile in general. Real units [meter,(m)] are used for both axes. An ED tether is located at $(x, y) = (0, 0)$.

The ion density distribution shows strong effects of the mesothermal condition. First, a wake region behind the tether is noticed. The wake is created by the quasi one-dimensional hypersonic motion of massive ions, $U_{tether} >> v_{t,i}$. Ions are flowing toward the tether from the left (ram region) almost one-dimensionally. Due to the tether's large potential, ions are slowed down in front of the tether and deflected from the 1-D trajectory. This creates an accumulation of ion density in front and on both sides of the tether. The envelope of ion trajectories creates something like a caustic line in optics. The potential at the peak of the ion accumulation is $5(V)$, which corresponds to the ion ram energy $\frac{1}{2}m_i U_{tether}^2$. The wake behind the tether starts closing itself. This is due to the small but finite ion thermal motion in the

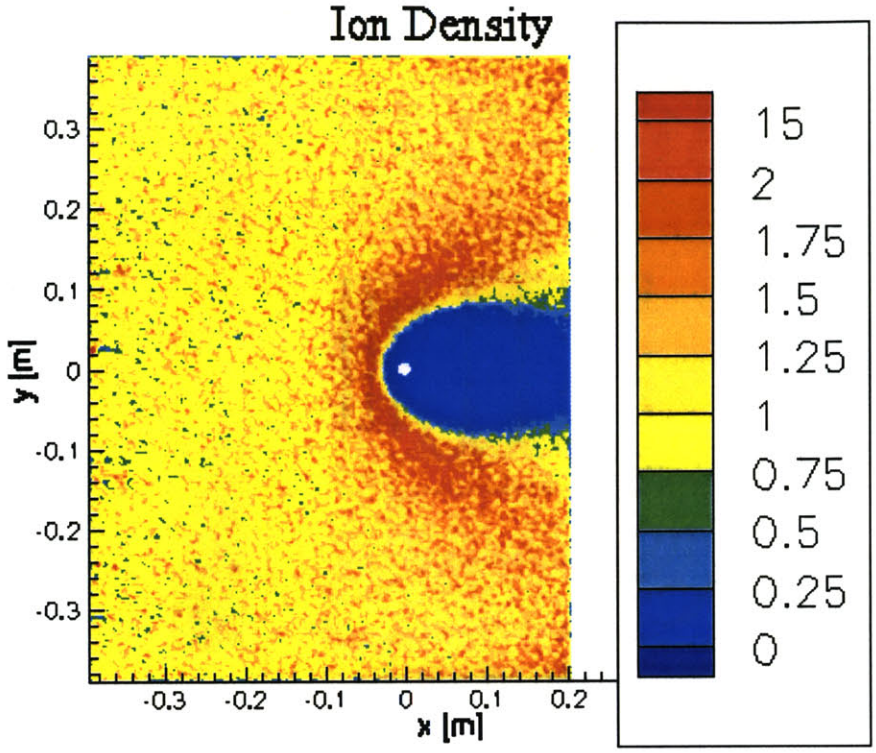

Figure 4-7: Nominal Case : Ion density

$y-$direction. The angle may be estimated roughly as the ratio of ion ram speed, U_{tether}, to the thermal speed, $v_{t,i}$, which is given as

$$\frac{v_{t,i}}{U_{tether}} \sim \frac{773[m/sec]}{8000[m/sec]} \sim 0.1 \tag{4.10}$$

and the angle is approximated as $\tan^{-1} 0.1 \sim 5°$. The distance required from the tether to include the whole wake is then calculated to be about $1[m]$. Throughout the region except for the wake, ion density is always more than that at infinity, due to the presheath region which has a small but positive potential.

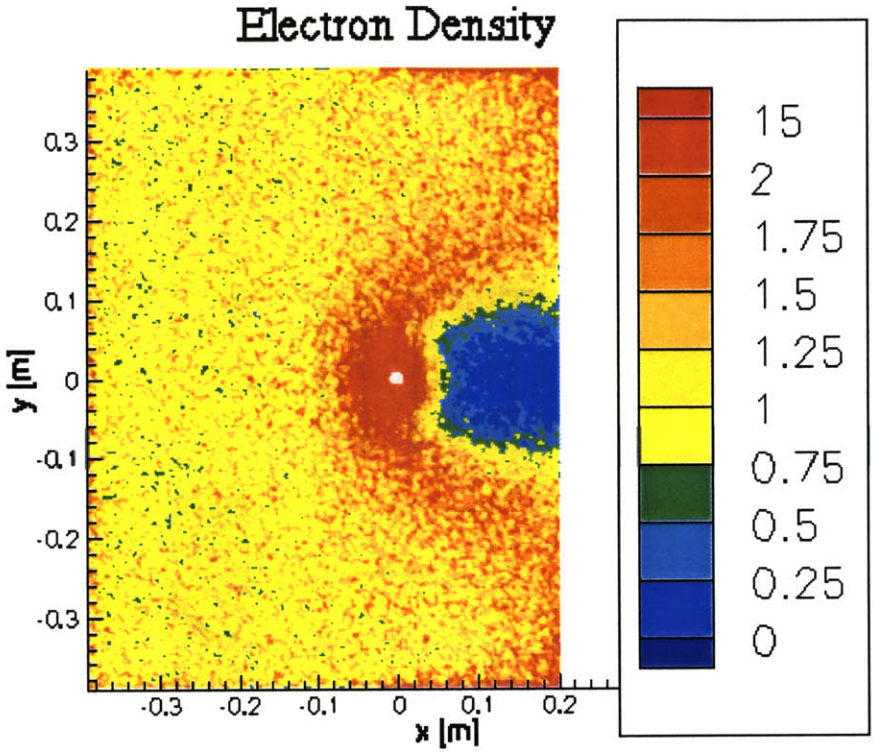

Figure 4-8: Nominal Case : Electron density

4.5.2 Electron density

In Figure 4-8, an instantaneous electron density normalized by that at infinity, n_∞, is plotted. Electrons are much lighter than ions and thus more mobile. Therefore faster perturbation of electron density is expected. The fluctuation of electron density is at most 20% over one plasma time. Since we limit ourselves to the discussion of macroscopic characteristics of electron density in this section, only the instantaneous map is shown.

Under the mesothermal condition, electrons are moving much faster than the tether, therefore the direct effect of plasma flow is almost negligible. A decisive factor to determine the electron density distribution is the ion density distribution, since a plasma has a strong tendency to maintain the quasi-neutrality on a larger scale than the local Debye length. This explains the low but non-zero density in the wake

region. Electron density in the wake region is decreased so that the local Debye length is comparable with the characteristic length of the wake. In this case, the length in the $y-$direction should be taken as a characteristic length. When electrons come close to the tether, the tether's large potential creates a sheath region where a plasma does not maintain the quasi-neutrality any more. Naturally the size of the sheath is of the order of a few Debye lengths.

Increased electron density ($> n_\infty$) is also noticed along the "caustic line" of increased ion density. Increased electron density in a geometrically 2D problem *without* magnetic field under steady conditions would be unlikely to happen [19]. However the presence of magnetic field renders the electron motion 3-dimensional and brings about the required increase in electron density. The question is then posed of where the magnetic effect is overwhelmed by the 2D electrostatic force by the high tether potential. This point will be elaborated on in sec 4.5.8.

The slightly increased electron density at the right top and right bottom corners of the computational domain is thought to be due to the boundary condition used for the ion distribution function on the side boundaries (top and bottom), where the deflection of the ion bulk flow is not taken into account. This brings in more ions at those boundary points and consequently attracts more electrons (or injects them from outside). These electrons only drift away towards the wake side due to the magnetic field and the tether's relative motion and do not contribute to electron collection to the tether.

At boundary points, electrons are injected according to the 3D magnetized plasma. Therefore the density there is always more than that at infinity, n_∞. In later sections, we discuss the validity of such an injection method by looking at individual electron trajectories, and discuss the limit of the 3D electron injection.

4.5.3 Electric Charge Density

In Figure 4-9, the instantaneous net charge density is shown. Since the size of the computational domain was chosen in such a way that it contains the sheath region, the quasi-neutrality can be seen in most of the presheath region. There are, however,

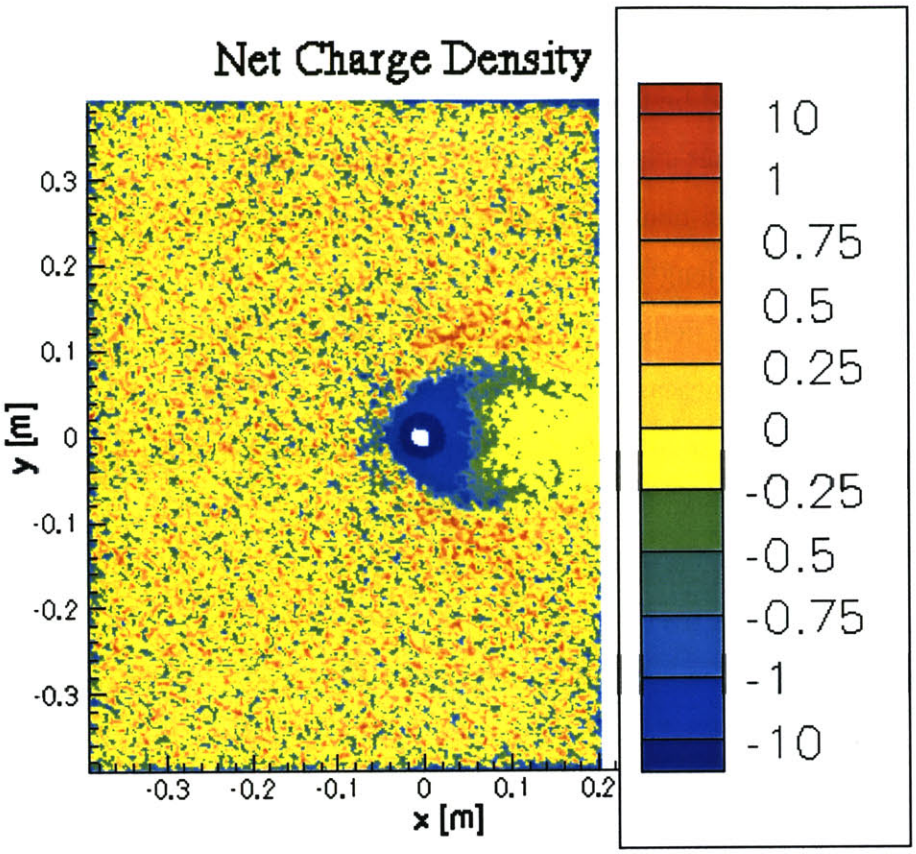

Figure 4-9: Nominal Case : Net charge density

three zones where the quasi-neutrality does not prevail. The first one is the wake. As the electron density is very low due to the ion depletion, the local Debye length is so large that the quasi-neutrality does not hold. Second is the sheath in the vicinity of the tether where a large potential due to the tether bias prohibits the ion population and attracts electrons form the non-neutral sheath. The last, subtle but interesting, is the ion accumulation at the sides of the tether where a "caustic" line was seen in ion density in Figure 4-7. It is interesting to see that the caustic line in front of the tether is well neutralized by electrons, but not on the sides. This hints that there are enough electrons coming from the front to enforce the quasi-neutrality, but not from the sides. Electron trajectories coming from the ram side will be examined in a later section and the mechanism for getting a higher electron density in front of the tether

will be discussed.

4.5.4 Electric Potential

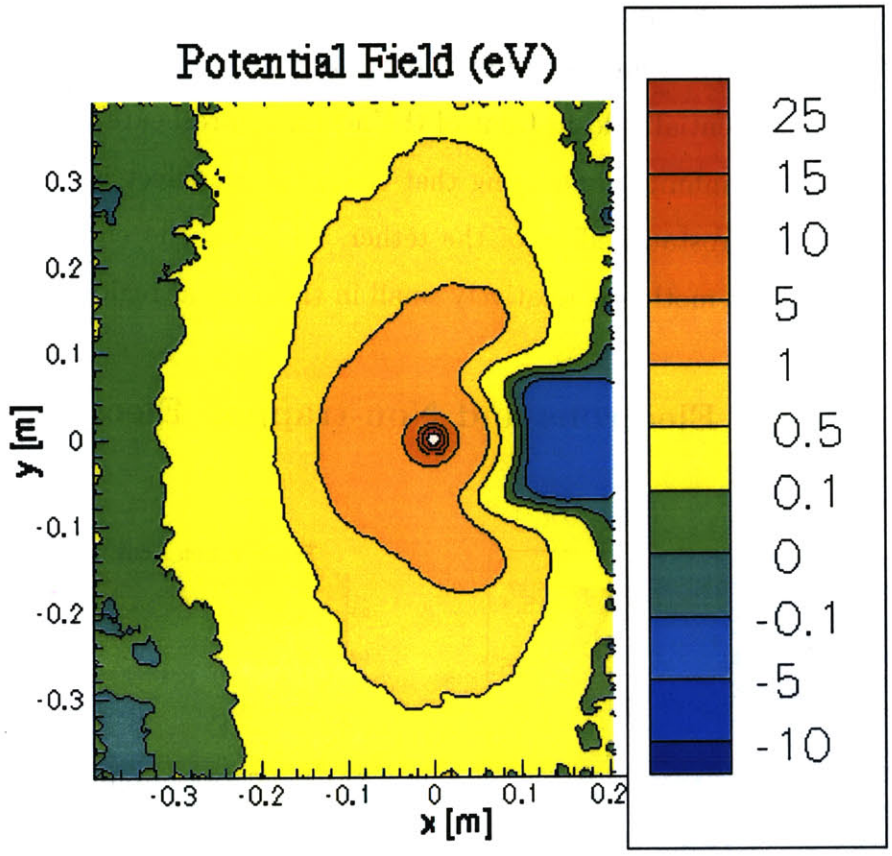

Figure 4-10: Nominal Case : Potential Field (V)

In Figure 4-10, the electric potential field in actual units (Volts) is plotted. Starting from the immediate vicinity of the tether (within a few Debye lengths), an axisymmetric potential is found due to the very high potential on the tether. The equipotential line of $5(V)$ can be located where the peak of ion density is found in Fig. 4-7. It is also noteworthy that at $5(V)$, it is still reasonable to approximate the potential field as axisymmetric. Farther out from the tether, the potential field changes its shape to contain the caustic line of ion density. By adopting such a potential profile, the plasma is trying to attract more electrons and maintain the quasi-neutrality. The

tendency to increase the potential is extended farther out. But it is only extended along the magnetic field (y-axis). Since an electron's motion is restricted by the magnetic field, it cannot move across the magnetic field freely. Instead, the positive potential field extends itself along the magnetic field lines, attracting more electrons from that direction. This potential wing is sometimes called "magnetic presheath" [22], distinguishing itself from the ordinary presheath which has a lower positive potential. Values of potential field in front of the magnetic presheath are almost equal to zero (potential at infinity) indicating that the magnetic effect is stronger in this region than the electrostatic effect of the tether, and that the effect of the tether potential on electrons motion is relatively small in this frontal region.

4.5.5 Trapped Electrons and Non-trapped Electrons

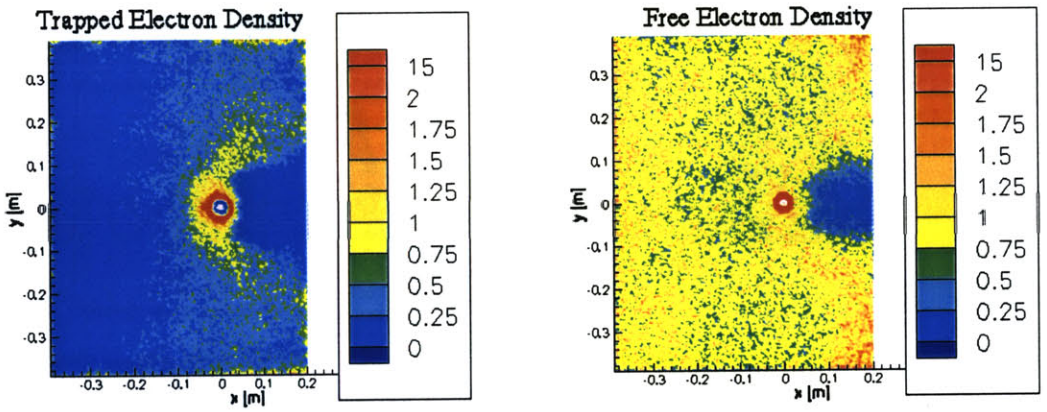

(a) Trapped Electron Density

(b) Non-trapped Electron Density

Figure 4-11: Trapped and Non-trapped Electron Density (Normalized by density at infinity n_∞)

In Figure 4-11, instantaneous trapped and non-trapped electron densities normalized by n_∞ are plotted. A trapped electron here is defined as having a negative total energy. Note that due to the $\vec{U} \times \vec{B}$ polarization field ($E_z = -U_{tether} B_y$) total energy is given as $E = E_\infty + eB_y U_{tether}(z - z_\infty)$. A trapped electron is defined by $E_\infty < 0$. As the PIC method is capable of simulating the unsteady particle-field interaction,

an electron can lose or it gain total energy. Once an electron loses total energy to the point where it becomes negative, the electron cannot go back to infinity where the local potential is set to zero so that only electrons with a positive total energy can exist. Therefore, the electrons with a negative total energy have to wander around inside the presheath and eventually get collected by the tether, or else gain energy from the potential field and escape to infinity. The trapped electrons seen in Fig. 4-11 are not guaranteed to be trapped all the time. They may gain energy at the next time step and get "non-trapped", or stay trapped for a considerable amount of time until the tether collects them. However, as in the case of electron density, we can think of the density maps as time-averaged ones, since the macroscopic view of the density does not change much.

The population of trapped electrons in general is not considerable. There are none on the ram side of the tether, which was discussed above to see little influence from the tether. The distribution of trapped electrons seems to be proportional to the local potential. In the magnetic presheath, in the immediate vicinity of the tether ($\phi > 5eV$) and on the caustic line of high ion density, local potentials are more than the equivalence of electron thermal energy ($kT_e/e = 0.1(eV)$). The zero trapped electron density in the small region around the tether is an artifact. In this region, electrons are moved analytically (sec. 3.2.15) and all the electrons are counted as free electrons, giving a large value in free electron density and zero density in trapped electron density. In our computations, we see large trapped electron density in the immediate vicinity of the tether.

The physical reasons for the trapped electron population are still unclear. Numerically, we can ascribe it to the accumulation of small negative errors due to the leapfrog method that we use as a particle advancing method. When an electron is traveling through a point where the second derivative of the potential field is positive, the finite timestep scheme always induces a small error.

In Figure 4-12, a cartoon of an electron traveling in a concave potential field is depicted. When the electron is climbing up the potential hill, due to the constant velocity for the time step, it loses total energy by missing kinetic energy which it

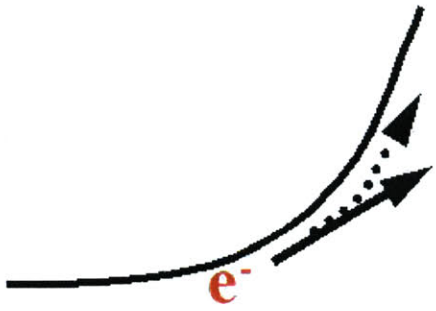

Figure 4-12: Error in total energy

should gain by increasing velocity. Of course, the reverse is also true. When an electron is going down a concave potential hill, it gains total energy. In our simulation, due to the high potential on the tether and the sheath region around it, the potential field around the tether is always concave (positive second derivative).

The leapfrog method in PIC is based on the Eulerian description whose stability condition is not limited by the Courant-Friedrich-Levy (CFL) condition. As a particle accumulates errors as it travels, even a small error ends up being non-negligible. In our computation, we use sub-cycling to minimize the error accumulation.

4.5.6 Current Collection

In Figure 4-13, the electron current collection calculated in our code is plotted with the 2D OML current. Together with these currents, the contribution of trapped electrons to the current collection is also plotted.

The trapped electrons current seem to be negligible here for the following reason. Not only is it already small, but also, according to the discussion we had in the previous section, electrons tend to lose total energy as they travel in the concave potential uphill. Therefore, the contribution seen in Figure 4-13 may be considered due to those electrons which approached the sheath region as a non-trapped electrons

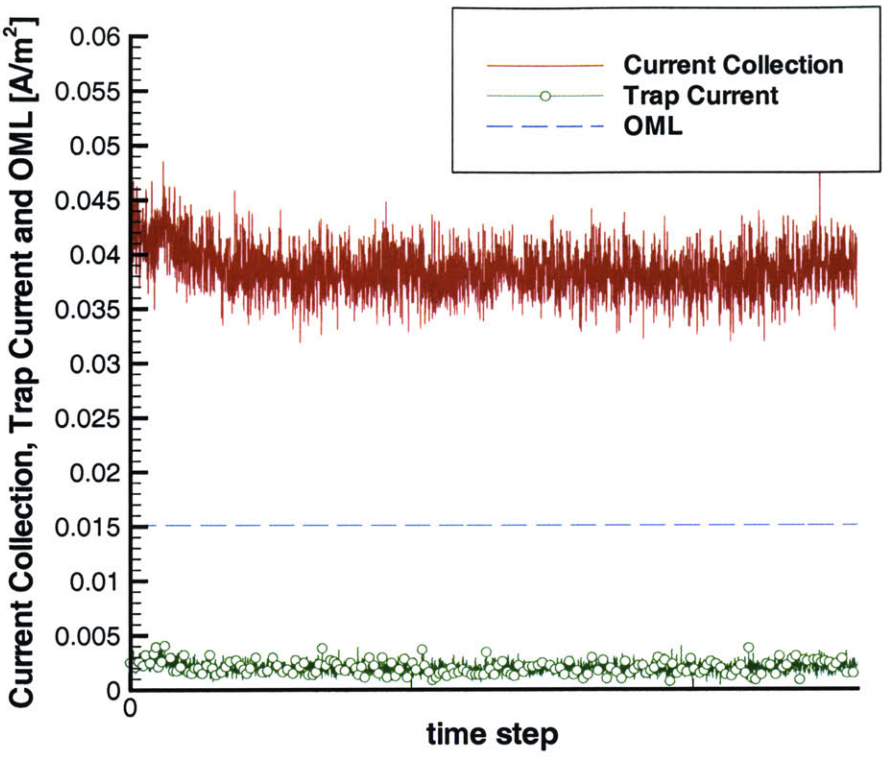

Figure 4-13: Nominal Case : Current Collection and 2D OML

and lost their total energy numerically while traveling in the sheath until they reach the surface of the tether.

Even without the contribution of trapped electrons, the collected current is obviously more than the 2D OML current by a factor of 2.5. This is mainly because of the three-dimensional motion of electrons due to the presence of the magnetic field. Note that the collected current is larger than the 2D OML current but still much lower than the 3D OML current. In order to see the difference of those current collections, let us briefly go through the derivation and discuss the applicability of the 3D OML current collection to a geometrically 2D problem, such as an ED tether.

2D OML vs. 3D OML

In the Parker-Laframboise theory, when computing the current by counting the electron flux on the collecting surface, electrons which have an energy less than the potential difference between this surface and infinity are excluded. In a geometrically 2D surface and with no magnetic field, some hypothetical electrons may be additionally excluded, because, even though their energy is sufficient, it resides mainly in the component parallel to the object's axis, and there is no mechanism to transfer it to the perpendicular plane; if the perpendicular part of the energy is less than the potential difference, these electrons can not exist near the surface. For the same 2D

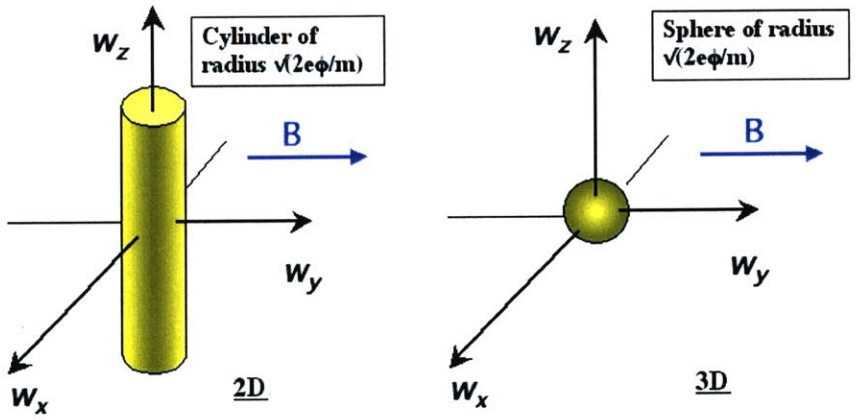

Figure 4-14: Electrons in velocity space. Electrons with velocities inside indicated regions, cylinder (2D,left) and sphere (3D,right), are excluded in the calculation of the OML current.

object, but with some magnetic field perpendicular to it, gyrations cyclically convert motion along the object's axis to motion perpendicular to it. Whether or not an electron with sufficient total energy but insufficient perpendicular energy can be found

near the surface is a complicated question. Considering a reversed trajectory, starting from the surface, the answer depends on whether or not the magnetic rotation is rapid enough to direct the electron away from the object before the electrostatic attraction forces it back to it.

Let us see how much close to or far away from the 3D OML we are in our computation. The 2D and 3D OML currents are given by considering at the collector surface all electrons except for those indicated in Figure 4-14. The 2D OML is already discussed in Section 1.4 and is given for $\frac{e\phi}{kT_e} >> 1$ as

$$J_{OML}(2D) = \frac{en_\infty}{\pi}\sqrt{\frac{2e\phi_p}{m_e}}. \tag{4.11}$$

And likewise the 3D OML current is given as

$$\begin{aligned} J_{OML}(3D) &= \iiint_{w_x^2+w_y^2+w_z^2 \geq 2e\phi_p/m, w_\perp > 0} ew_\perp f_e d\mathbf{w} \\ &= en_\infty\sqrt{\frac{\kappa T_e}{2\pi m_e}}\left(1+\frac{e\phi_p}{\kappa T_e}\right) \end{aligned} \tag{4.12}$$

In the limit of $\frac{e\phi}{kT_e} >> 1$, the ratio of the 3D OML current to the 2D OML is $J_{OML}(3D)/J_{OML}(2D) = \left(1+\frac{e\phi_p}{\kappa T_e}\right) / \left(\frac{2}{\sqrt{\pi}}\sqrt{\frac{e\phi_p}{\kappa T_e}}\right) \cong \frac{\sqrt{\pi}}{2}\sqrt{\frac{e\phi_p}{\kappa T_e}}$. For $\phi_p = 25(V)$ and $T_e = 0.1(eV)$, this ratio would be ~ 14.01. This is much larger than what we see in our results, $J(\text{computation})/J_{OML}(2D) \sim 2.5$. From this, we can postulate that two-dimensional electrostatic effects near the tether reduce the current collection from the 3D OML but the effect does not reach to infinity. From infinity to the point where the electrostatic effect overwhelms magnetic effects, electron gyration allows more electrons to be attracted. Then electrons enter the region where 2D electrostatic force by the tether starts dominating. Let $\phi_{2\sim3}$ be the potential at the transition point. From that point electrons are dominated by the 2D electrostatic force and accelerated only in the perpendicular plane. By this mechanism, hypothetical electrons in $w_x^2 + w_y^2 \leq 2e(\phi_p - \phi_{2\sim3})/m$ in velocity space are excluded from the flux calculation through the surface of the tether.

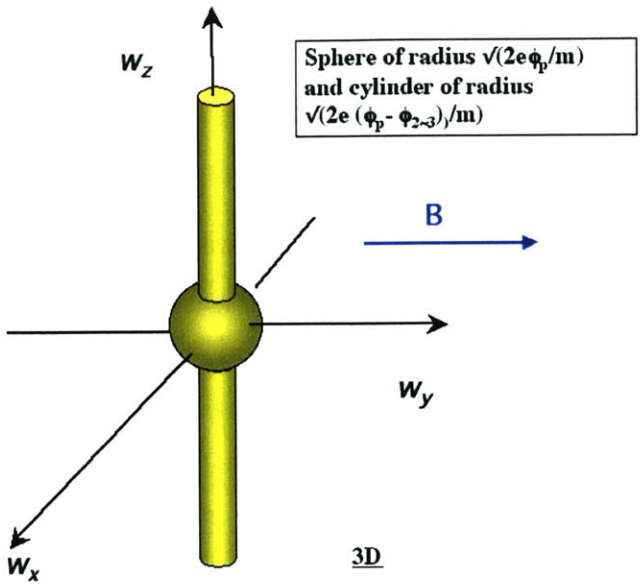

Figure 4-15: Electrons in velocity space. Electrons with velocities inside indicated regions, cylinder (2D,left) and sphere (3D,right), are excluded in the calculation of the OML current.

Let us calculate the current density to the surface when the electrons with velocity indicated in Fig. 4-15 are excluded. After normalizing the velocity with the thermal velocity $v_{Te} = \sqrt{2\kappa T_e/m_e}$ and the potential by $\kappa T_e/e$ as $\Phi = \frac{e\phi}{\kappa T_e}$, we obtain the current density to the surface as

$$
\begin{aligned}
J_{2\sim3} &= \frac{2en_\infty v_{Te}}{\pi^{3/2}} \exp(\Phi_p) \left[\int_0^{\sqrt{\Phi}} \int_{\sqrt{\Phi_p - w_z^2}}^{\infty} w^2 \exp(-w^2 - w_z^2) dw\, dw_z \right. \\
&\quad \left. + \int_{\sqrt{\Phi}}^{\infty} \int_{\sqrt{\Phi_p - \Phi}}^{\infty} w^2 \exp(-w^2 - w_z^2) dw\, dw_z \right] \\
&= \frac{2en_\infty v_{Te}}{\pi^{3/2}} \left[\Phi_p \left(\sqrt{\frac{\Phi}{\Phi_p}} \sqrt{1 - \frac{\Phi}{\Phi_p}} + \sin^{-1} \sqrt{\frac{\Phi}{\Phi_p}} \right) \right. \\
&\quad + \sqrt{\pi} \sqrt{\Phi_p} \int_0^{\sqrt{\frac{\Phi}{\Phi_p}}} \mathrm{erfcx}\left(\sqrt{\Phi_p (1 - x^2)} \right) dx \\
&\quad \left. + \sqrt{\pi} \mathrm{erfcx}\left(\sqrt{\Phi} \right) \sqrt{\Phi_p - \Phi} + \frac{\pi}{2} \mathrm{erfcx}\left(\sqrt{\Phi_p - \Phi} \right) \mathrm{erfcx}\left(\sqrt{\Phi} \right) \right] \quad (4.13)
\end{aligned}
$$

where $\Phi = \frac{e\phi_{2\sim3}}{\kappa T_e}$ and the scaled complementary error function is defined as

$$\text{erfcx}(x) = \exp(x^2)\text{erfc}(x) \tag{4.14}$$

Equation (4.13) for the nominal case with $\Phi_p = 250$ is plotted in Figure 4-16. The current is normalized by the 2D OML current, indicating that for $\Phi = 0$ the current is the 2D OML and for $\Phi = \Phi_p$ the 3D OML ($= 14 \times J_{OML}(2D)$). From Fig. 4-16, it

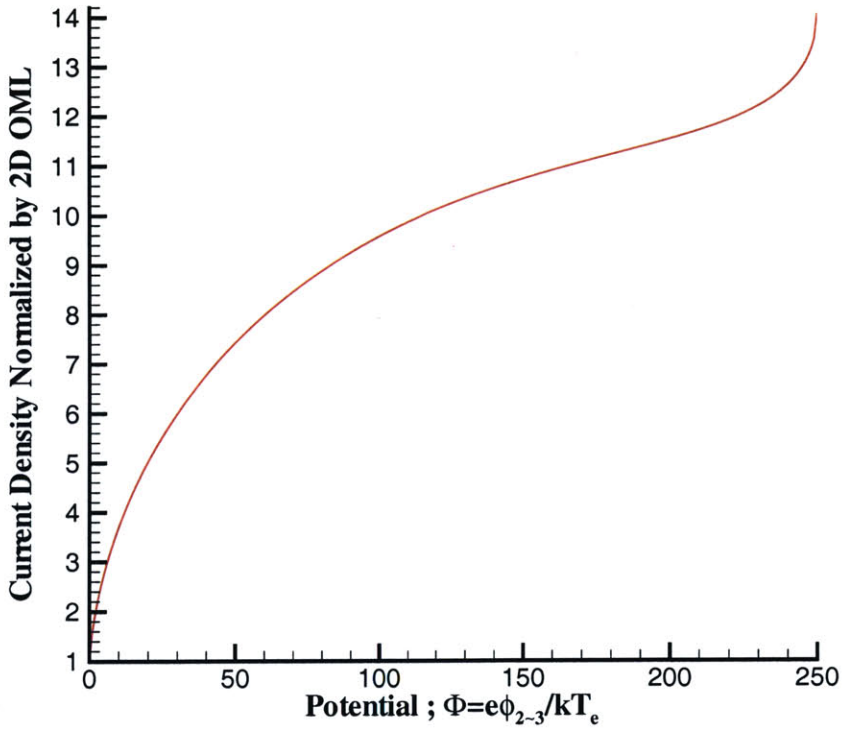

Figure 4-16: OML current density with a transient potential $\Phi = \frac{e\phi_{2\sim3}}{\kappa T_e}$ for the nominal case, $\Phi_p = \frac{e\phi_p}{\kappa T_e} = 250$ ($T_e = 0.1(eV)$)

is seen that, if the electrostatic force becomes dominant over the 3D magnetic effect at $\frac{e\phi}{\kappa T_e} \approx 5$ ($\phi \approx 0.5(V)$), the OML current to the surface becomes about $2.6 \sim 2.7$ times larger than the 2D OML current.

In conclusion, even if the geometry of the problem is two-dimensional, we can

expect the 3D OML current as the upper limit in a steady state. However, the electrostatic effect near and around the tether renders electron motions two-dimensional, reducing the OML below the 3D limit. In terms of reverse trajectory, this can be rephrased to say that the trajectory of an electron on the collecting surface may be intercepted by the tether multiple times, even if it has a sufficient energy to reach infinity. But we can still expect higher current collection than the 2D OML current to a bare cylindrical tether in LEO in steady state.

4.5.7 Particle Motions

In this section, we look at an individual electron's motion and discuss the mechanism in relation with macroscopic views of plasma behavior discussed in previous sections. In Figure 4-17, a typical electron trajectory and the history of its variables are shown with potential field. The potential field is included in order to examine the interaction between the electron's motion and the overall plasma behavior.

The most significant thing to note in this particular case is the electron "trapping" even if the electron's total energy is positive. In the previous section where we discussed trapped electrons, which were then defined as having a negative total energy. Therefore we have to distinguish those trapped electrons with a negative total energy from those that we will discuss here, which do not necessarily have a negative total energy. For the case in Fig. 4-17, the total energy is not only positive, but in addition, it is seen to increase in time. However, the electron trajectory in space, (d) in Fig. 4-17, clearly shows its "trapping". We denote this phenomenon as "containing".

Here we need some comments on the total energy, E. In the presence of magnetic field, a quantity defined by $\frac{1}{2}m_e(w_x^2+w_y^2+w_z^2)-e\phi$ is not supposed to be conserved. The polarization field, $E_z=-UB_y$, does work on the particles (as seen in the tether frame), so that the energy equation reads,

$$E=\frac{1}{2}m_e(w_x^2+w_y^2+w_z^2)-e\phi=\frac{1}{2}m_e(w_{x\infty}^2+w_{y\infty}^2+w_{z\infty}^2)+eB_yU_{tether}(z-z_\infty) \quad (4.15)$$

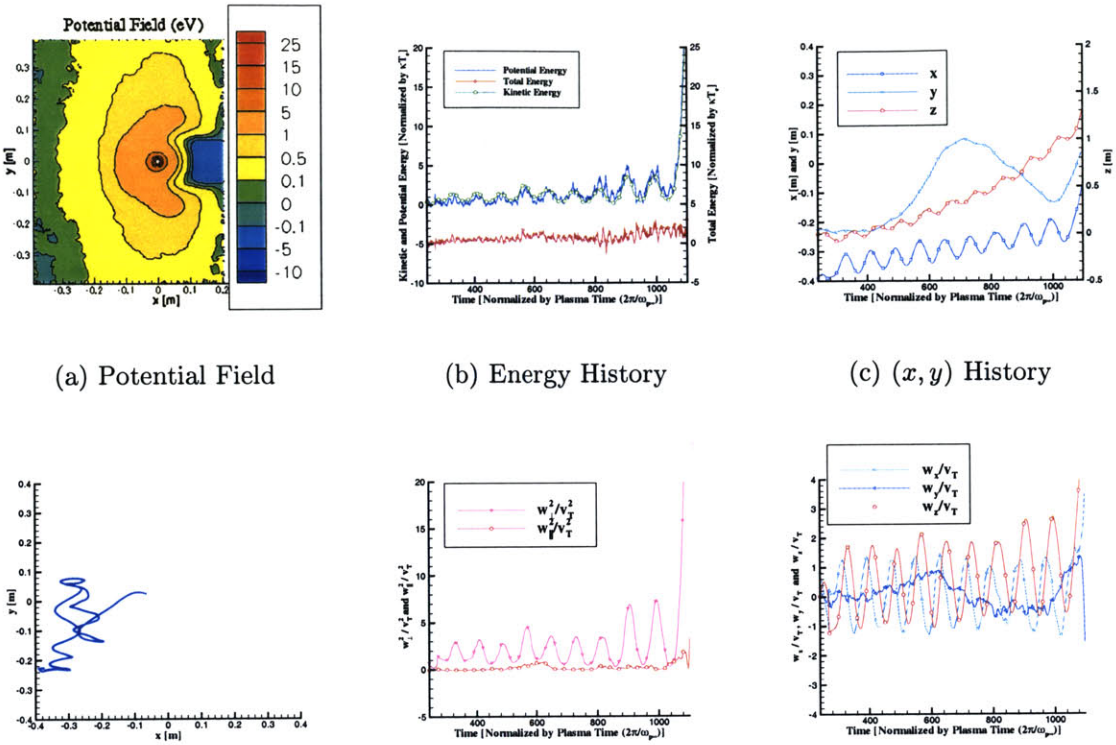

(a) Potential Field

(b) Energy History

(c) (x, y) History

(d) Particle Trajectory (ending in capture near (0,0))

(e) $(w_\perp^2/v_t^2, w_\parallel^2/v_t^2)$ History

(f) (v_x, v_y, v_z) History

Figure 4-17: Typical "contained" electron trajectory and its variables history

and therefore E increases linearly with z. From the equation of motion in the z-direction, we have $\frac{dw_z}{dt} = -\omega_c(w_x - U_{tether})$, which integrates to $\frac{dz}{dt} = w_{z\infty} - \omega_c(w_x - U_{tether}t)$ and for $w_{z\infty} \sim 0$, since $x - U_{tether}t$ is positive most of the time for an electron approaching the tether (electrons accelerate forward as they approach), we have $z - z_\infty > 0$ because $B_y < 0$, and E should be decreasing. In Figure 4-17(b), the plot under the name of "Total Energy" is actually given by

$$E_\infty = \frac{1}{2}m_e(w_x^2 + w_y^2 + w_z^2) - e\phi - eB_yU_{tether}(z - z_\infty). \tag{4.16}$$

A particle with $E_\infty < 0$ is trapped and cannot reach infinity, even if $E > 0$ because $B_y(z - z_\infty) > 0$. The mechanism of the electron containment is as follows. The potential hump created by the tether potential is traveling in LEO at the tether's

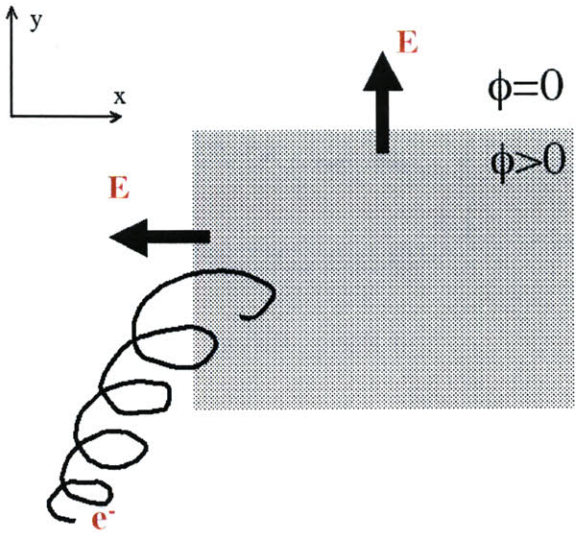

Figure 4-18: Gyrating electron approaches a potential hump

orbital speed. In the frame of reference of the tether, plasma is flowing at the same speed into the plasma hump. For brevity, let us model the potential hump as a rectangular region with a positive potential as shown in Fig. 4-18 . The magnetic field is aligned along the y-direction, and electrons are gyrating about the magnetic field, drifting in the x-direction to represent the tether relative motion with respect to the plasma. The drift of electrons in the x-direction is also recognized in (c) of Fig. 4-17, and it is due to the presence of an E_z field component ($= U_{tether} \times B$) in the tether's frame.

In Fig. 4-18, when the electron encounters the potential hump, it sees the electric field only in the x-direction. Due to this electric field, the electron is accelerated but only in the x-direction. In terms of total energy, the electron gains kinetic energy in its component perpendicular to $\vec{B}$,

$$E = \frac{1}{2} m_e (\underbrace{w_\perp^2}_{\text{Only this term increases}} + w_\parallel^2) - e\phi \tag{4.17}$$

Where the perpendicular kinetic energy (perpendicular to magnetic field) increases

by the potential difference,$e\phi$. The longitudinal component of kinetic energy is the same as before entering the potential hump.

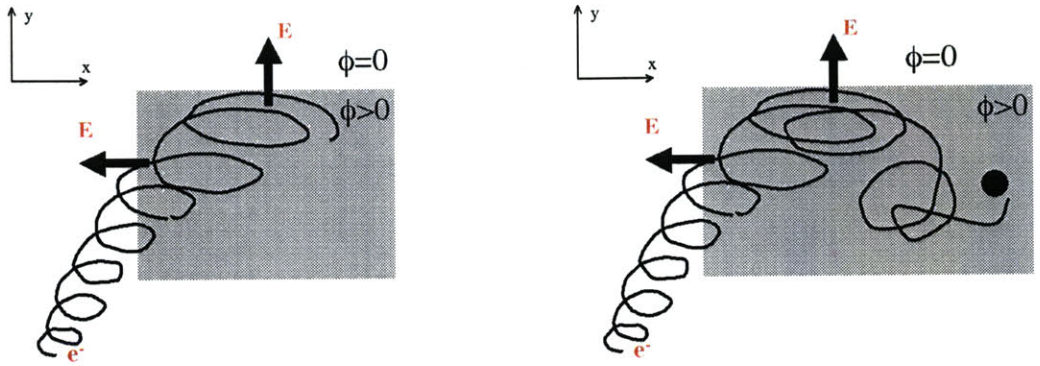

(a) Gyrating electron inside a potential hump

(b) Tether and electron inside a potential hump

Figure 4-19: Electron "trapping" in a potential hump

Once the electron enters inside the potential hump, it continues gyrating with a larger Larmor radius ((a) in Fig. 4-19). But the longitudinal velocity does not change. After a while, the electron is confronted with the electric field at the side of the hump. In order for the electron to continue traveling in the same y-direction, it must have enough kinetic energy in the same direction to climb over the potential difference. In this simple case, if the longitudinal kinetic energy $\frac{1}{2}m_e w_{||}^2$ is smaller than the potential difference, $e\phi$, the electron gets reflected back inside the potential hump. Since there is no mechanism for the electron to gain longitudinal kinetic energy in this model, the electron continues bouncing back and forth inside the potential hump, while being contained (except for the drift) in the x-direction.

When there is no object such as an ED tether, the electron would go out of the potential hump from the back of the hump where it has enough perpendicular kinetic energy to climb over the potential difference. But when there is an object with a high positive potential, the electron goes under the influence of electrostatic force created by the object and may get collected ((b) in Fig. 4-19).

The electrons that we consider here seem to be responsible for neutralizing the ion accumulation in front of the tether. Since those electrons are under the strong

effect of the electrostatic force by the tether, they do not go beyond the tether and neutralize the ion caustic line at the back sides of the tether.

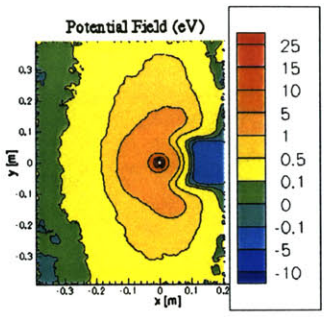

(a) Potential Field

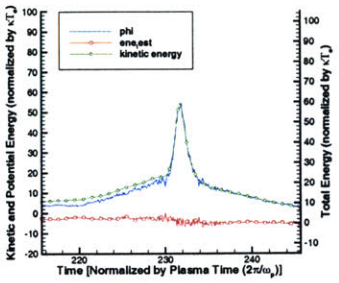

(b) Energy History

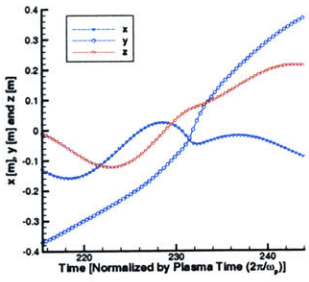

(c) (x, y) History

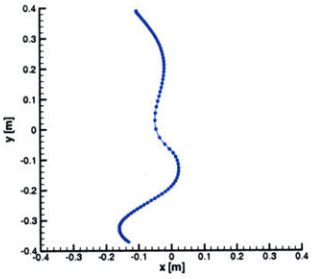

(d) Particle Trajectory

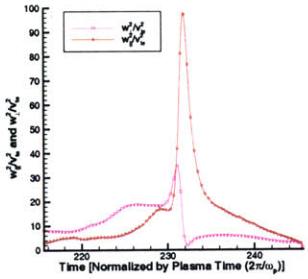

(e) $(w_\perp^2/v_t^2, w_\parallel^2/v_t^2)$ History

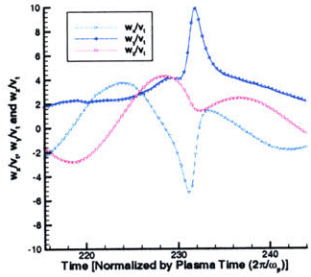

(f) (v_x, v_y, v_z) History

Figure 4-20: Typical "non-trapped" electron trajectory and its variable history

Next, let us look at the case where an electron does not get contained. In Fig. 4-20, a "non-contained" electron trajectory and its variable history are shown. The electron is traveling quite close to the tether from bottom to top ((d) in Fig. 4-20). In most cases, an electron in such a situation is captured by the tether. Therefore, this is a very rare case that an electron is not captured. The figure is shown here in order to demonstrate the difference between "contained" and "non-contained" particles. As seen in (e) in Fig. 4-20, the electron gains kinetic energy in the longitudinal direction (along $\vec{B}$) as it enters the higher potential region. In terms of a square potential hump, the electron enters from the "side", gaining kinetic energy in the $\frac{1}{2}m_e w_\parallel^2$ part and has enough momentum to get out of the potential hump from the other "side".

In (b) of Fig. 4-20, we can notice a small decrease in the electron's total energy, which is defined as E_∞. This may be considered due to numerical error, which was discussed in Sec. 4.5.5. In general, in our computation, a magnetized plasma does not experience violent fluctuations. However, there still exist certain particle-field interactions in our simulation. In the next section, plasma oscillations are discussed.

4.5.8 Plasma Oscillations

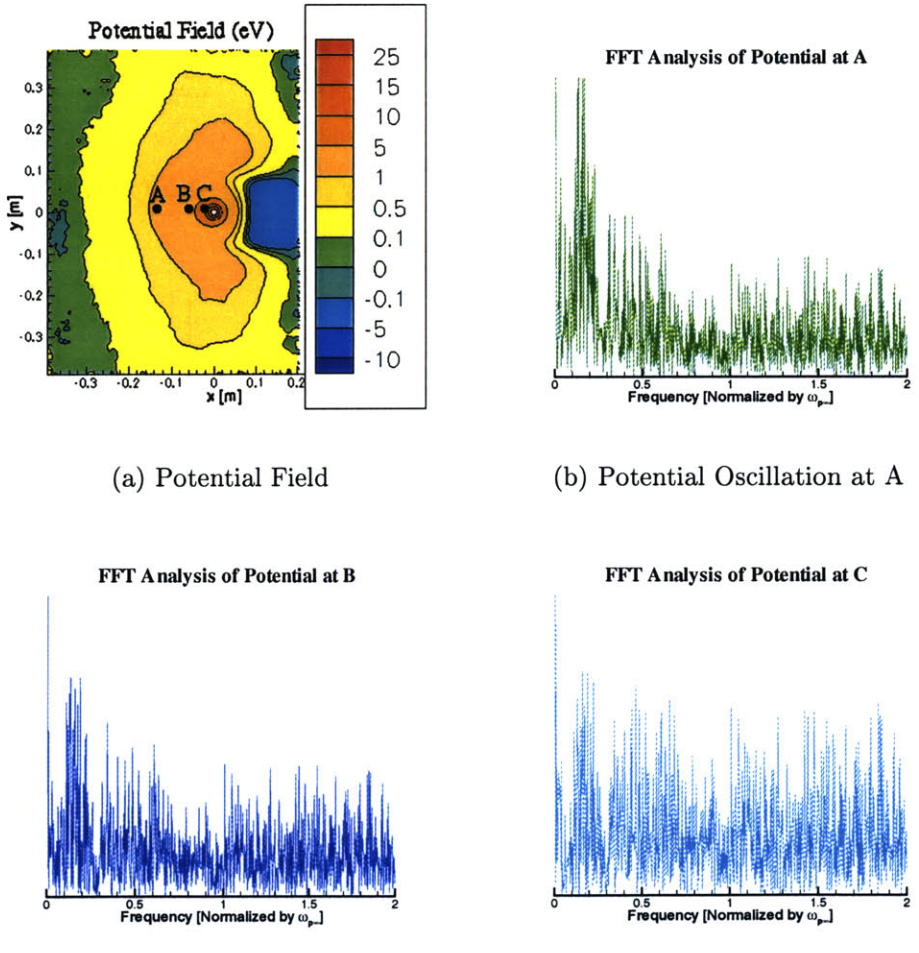

(a) Potential Field

(b) Potential Oscillation at A

(c) Potential Oscillation at B

(d) Potential Oscillation at C

Figure 4-21: Fast Fourier Analysis (FFT) of potential oscillations near the tether

In Figure 4-21, Fast Fourier Transform (FFT) analyses of potential field at points indicated in (a) are shown. Point A is about 35 Debye lengths away from the tether,

Point B 15 Debye lengths away (still in the pre-sheath) and Point C 5 Debye lengths away and inside the sheath. At Point C, there is no significant peak recognized. As we check further away from the tether in front, we start seeing a peak around $\omega/\omega_{p,\infty} = 0.05 \sim 0.25$.

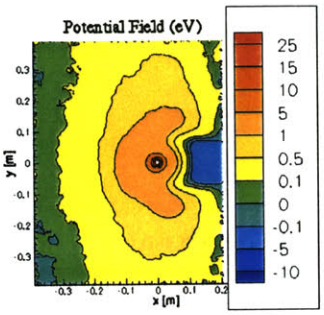

(a) Potential Field

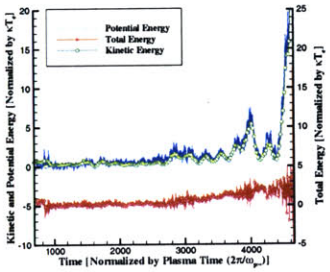

(b) Energy History

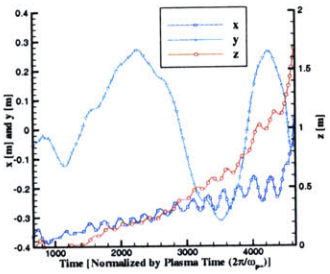

(c) (x, y) History

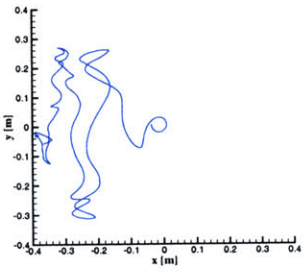

(d) Particle Trajectory

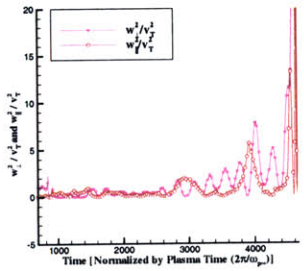

(e) $(w_\perp^2/v_t^2, w_\parallel^2/v_t^2)$ History

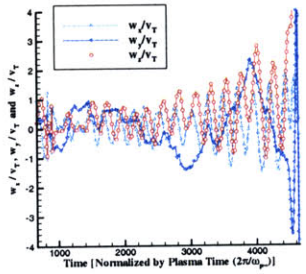

(f) (w_x, w_y, w_z) History

Figure 4-22: Typical "contained" electron trajectory and its variables history

This band of frequency is mainly due to the sloshing of contained electrons. In (d) of Figure 4-22, the trajectory of a typical contained electron is depicted. The frequency of the sloshing motion of the electron can be seen in Fig. (c), where the history of (x, y, z) coordinates of the electron is shown. x- and z-coordinates oscillate at the cyclotron frequency, $\frac{eB}{m_e}$, whereas the y-coordinate increases its frequency as the electron gets contained in a narrower region. The band of frequency ranges up to a frequency corresponding to the electron cyclotron frequency. As the electron approaches the tether, it is now under the effect of the electrostatic force created by

the high potential on the tether. The sloshing motion of the electron becomes an orbiting motion around the tether by the central force. The frequency of the orbiting depends on the distance from the tether.

$$\begin{aligned} mr\omega^2 &= eE \\ \omega &= \sqrt{\frac{eE}{mr}} \end{aligned} \tag{4.18}$$

In Figure 4-23, the magnitude of electric field is indicated, from which we can extract

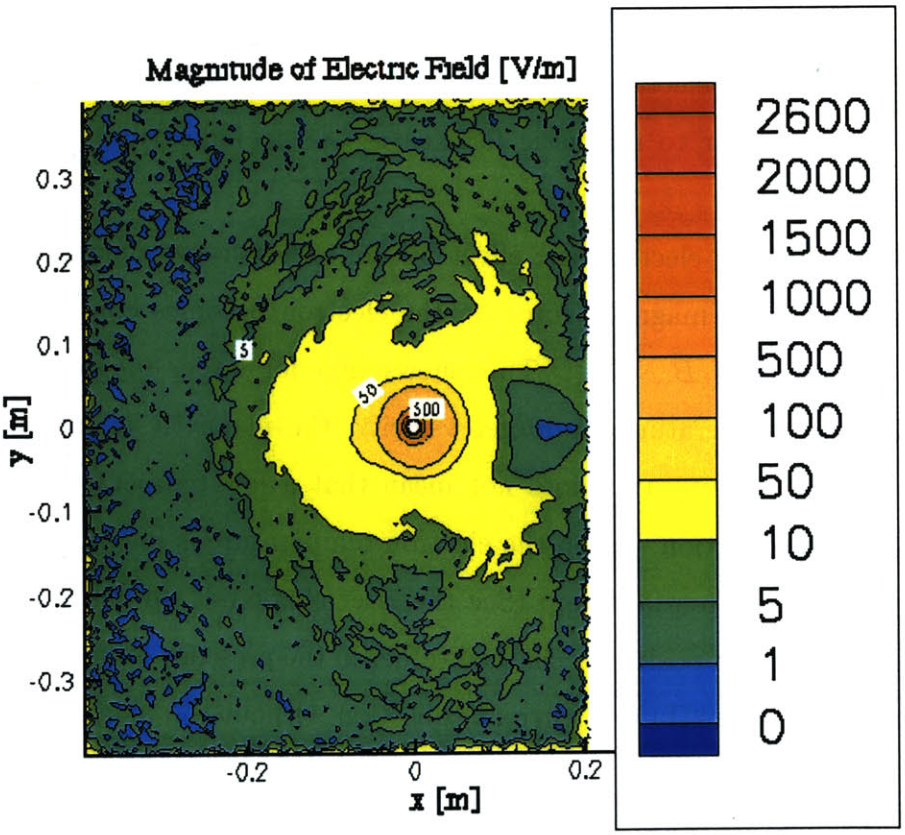

Figure 4-23: Magnitude of Electric Field

some numbers for the estimate. In the vicinity of the tether (within about 10 Debye lengths from the tether), the frequency of an electron orbiting about the tether is

given by equation (4.18) as

$$\omega \sim \sqrt{\frac{1.6 \times 10^{-19} \times 100}{0.91 \times 10^{-30} \times 10 \times 0.7 \times 10^{-2}}} \sim 1.58 \times 10^{7} \quad (4.19)$$

$$= 0.89\omega_p \quad (4.20)$$

This frequency increases as the electron gets closer to the tether. The band of higher frequency than those for the electron sloshing ($\omega \sim 0.2\omega_p$) in (d) of Fig. 4-21 may be ascribed to the high speed orbiting motion of electrons around the tether.

The point where the electrostatic effect starts balancing with the magnetic effect can also be seen from Figure 4-22. At time $\sim$ 4400 in (c), the electron gyro-motion is clearly affected by the electrostatic force at $(x, y) = (-0.2, 0.2)$. At this point, we can approximate the electric field from Fig. 4-23 as $E \sim 5[V/m]$ and the electron velocity perpendicular to magnetic field as $w_\perp \sim v_t$, indicating the force balance $w_\perp B \sim E \sim 5[V/m]$.

In conclusion, the electrostatic effect by the tether starts affecting an electron's trajectory where the magnetic force on the electron becomes comparable with the electrostatic force, $w_\perp B \sim E_\perp$. This shows that for larger magnetic field and/or larger electron temperature, or larger velocity, the magnetic effect prevails closer to the tether. However, this does not mean that a low temperature plasma gives smaller current collection. When the electron temperature is low, it is more likely to be contained in a potential hump (See the later chapters). In general, the electron current collection to a positively charged tether in the presence of magnetic field tends to be larger than the 2D OML current collection without the magnetic field.

4.5.9 Frozen Case

In order to see the effect of plasma oscillation on the current collection, we perform a simulation of the nominal case with a frozen potential field. In Figure 4-24, current collection is shown to be about 2.3 times larger than the 2D OML. It is a little lower than the nominal case. In order to establish a similar potential profile to that of the nominal case, the first few hundreds iterations are run normally and the potential

field is then frozen. The potential is shown in Figure 4-25(a).

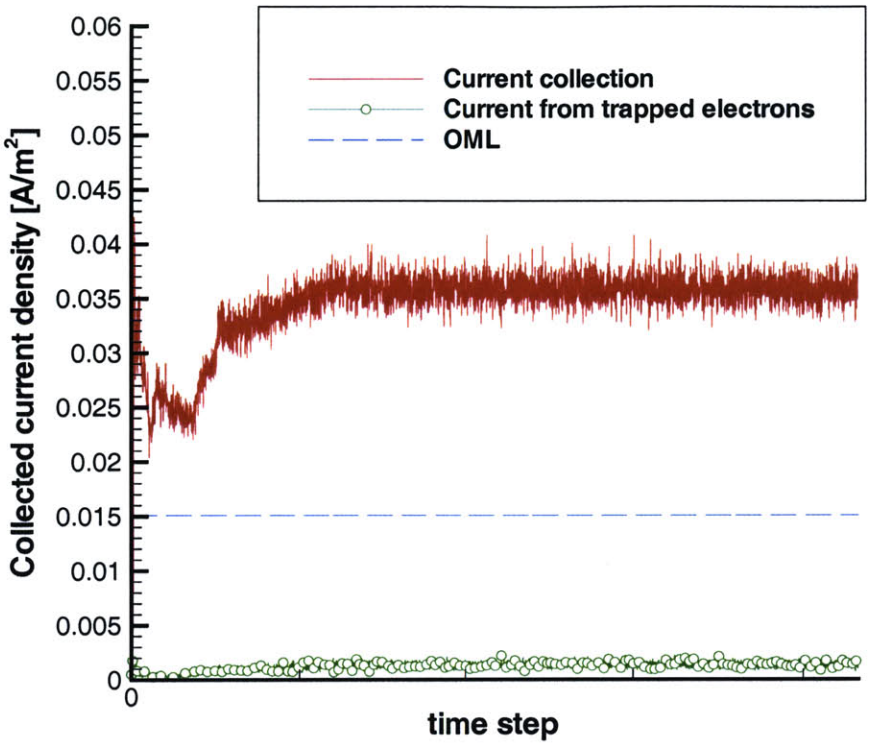

Figure 4-24: Current Collection with a frozen potential field

Total energy, E_∞, plotted in Figure 4-25(b) of course is constant. Electron "containment" is clear in Figure(d). We can also check several numerical effects of a PIC method on the computation. In Figure 4-24, it is also seen that there is some contribution by trapped electrons to the current collection. Since there is no potential fluctuation, there should be no new trapped electrons in the numerical domain. Some "inherited" trapped electrons obtained when we freeze the potential should be collected by the tether after certain long time. And others may still remain in the domain. However as seen in Figure 4-26(a), there is certain population of trapped electrons in the vicinity of the tether, where the local potential is high and increases toward the tether. This is considered to be due to the numerical error explained in Section (4.5.5).

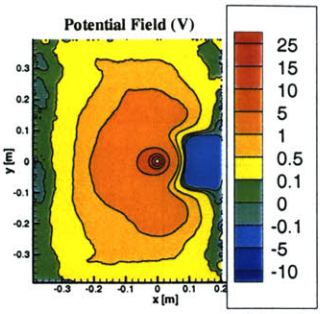

(a) Potential Field

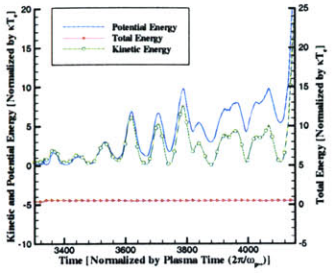

(b) Energy History

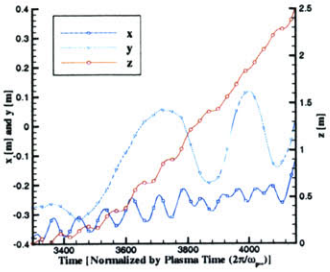

(c) (x, y) History

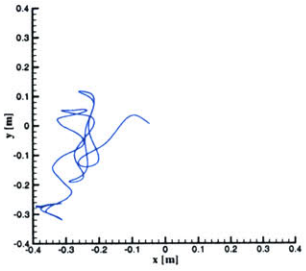

(d) Particle Trajectory

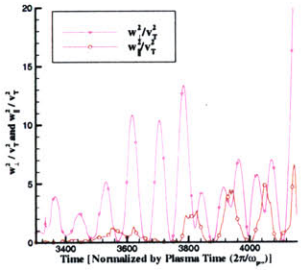

(e) $(w_\perp^2/v_t^2, w_\parallel^2/v_t^2)$ History

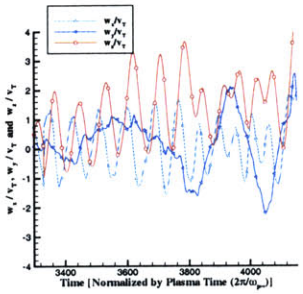

(f) (w_x, w_y, w_z) History

Figure 4-25: Typical "contained" electron trajectory and its variables history in a frozen case

From Figures 4-26(c)-(e), some considerable non-neutrality between electron density and ion density is recognized. It may be due to the lack of the ability of the potential to re-adjust itself to maintain quasi-neutrality. It indicates the power of PIC to produce really self-consistent solutions.

From this check, we can assure that the enhancement of current collection over the 2D OML is possible without plasma fluctuations. The collected current is a little lower than the nominal case. It may be because in the nominal case there are numerical and/or physical electron trappings which contribute extra current to the tether.

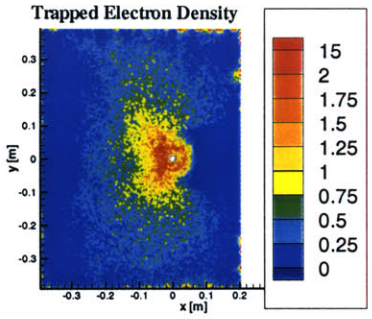

(a) Trapped electron density

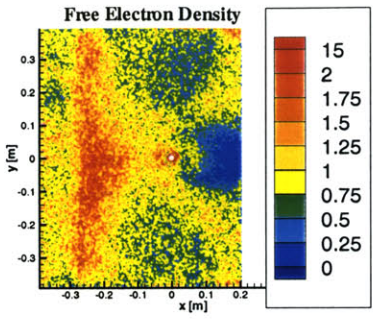

(b) Nontrapped electron density

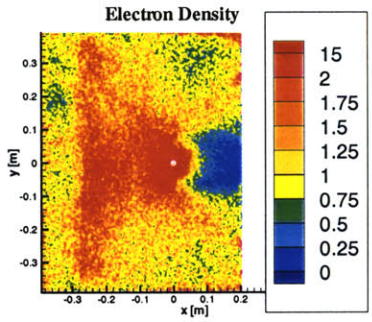

(c) Electron density

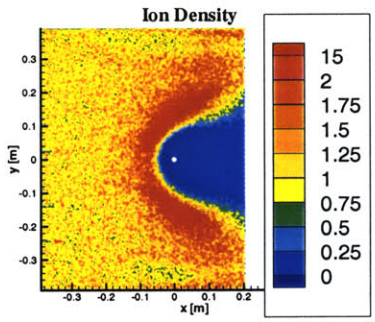

(d) Ion density

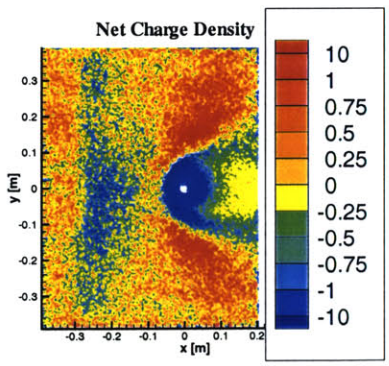

(e) Net Charge density

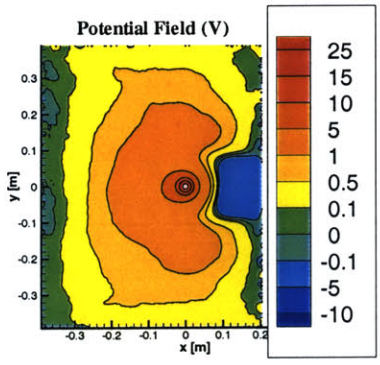

(f) Potential

Figure 4-26: Field quantities in the frozen case

Chapter 5

Results and Pre-Flight Predictions II

The main purpose of the work presented in this thesis is the preflight prediction of the ProSEDS experiment, which is planned to be launched November 2002. Since the tether shall find itself in many different plasma situations, it is necessary to take into account the variety of plasma parameters. In the previous chapter, in order to discuss the physics involved in the current collection, we considered a case of the plasma parameters (Figure 4.1) which show typical numbers that an electrodynamic tether will encounter in LEO. As the electrodynamic tether orbits around the Earth through day and night, the ambient density ranges from $1.0 \times 10^{11} \sim 10^{12}(1/m^3)$. The tether potential will be more than $100(V)$. Electron temperature tends to be $0.2 \sim 0.3(eV)$ above the altitude of $500(km)$. Ion temperature is typically a little lower than the electron temperature [5]. In order to predict the current collection in a plasma situation different from the nominal case, several simulations with different plasma parameters are presented in this chapter so that the prediction of the current collection for different plasma parameters may be performed by interpolating or extrapolating the results. We change one parameter for each case from the nominal case and check the effect of the parameter on the current collection. We also check a few cases where two parameters, the electron temperature and the tether potential, are changed and examine the combined effects of the two parameters. The comparison cases are listed

in Table 4.2.

5.1 Current Collections

Comparison Case	Ratio to OML	Current Collection
Nominal Case	2.6	0.04 $[A/m^2]$
Case 1 ($B = 0.1(G)$)	2.6	0.04 $[A/m^2]$
Case 2 ($B = 0.6(G)$)	2.6	0.04 $[A/m^2]$
Case 3 ($\phi_p = 10(V)$)	2.4	0.024 $[A/m^2]$
Case 4 ($\phi_p = 100(V)$)	0.95	0.0285 $[A/m^2]$
Case 5 ($\frac{d}{d_D} = 0.3$)	2.6	0.4 $[A/m^2]$
Case 6 ($\frac{d}{d_D} = 3$)	1.83	0.0275 $[A/m^2]$
Case 7 ($\frac{d}{d_D} = 10$)	(can not run)	(can not run) $[A/m^2]$
Case 8 ($T_e = 0.05(eV)$)	3.0	0.045 $[A/m^2]$
Case 9 ($T_e = 0.2(eV)$)	2.16	0.0325 $[A/m^2]$
Case 10 ($T_i = 0.05(eV)$)	2.6	0.04 $[A/m^2]$
Case 11 ($T_i = 0.2(eV)$)	2.6	0.04 $[A/m^2]$
Case 12 ($\theta = 60^o$)	1.16	0.0175 $[A/m^2]$
Case 13 ($T_e = 0.05(eV) \& \phi_p = 10(V)$)	2.5	0.025 $[A/m^2]$
Case 14 ($T_e = 0.2(eV) \& \phi_p = 10(V)$)	2.25	0.0225 $[A/m^2]$
Case 15 ($\frac{d}{d_D} = 0.1 \& \phi_p = 100(V)$)	1.333	0.04 $[A/m^2]$

Table 5.1: Current Collection in the comparison cases

In Table 5.1 results from comparison cases are shown. From Cases 1 and 2, we see that the magnetic effect does not change the current collection. As we will see later, Case 1 is performed to check the validity of the 3D calculation of density and flux at the computational domain. Cases 3 and 4 show the dependence of the current collection on the tether potential. Case 4 does not seem to be fully converged, and may not represent reality. However, the relation of electron motions and the current collection can be understood better from the acquired potential profile. Cases 5, 6 and 7 deal with different tether radius. In Case 7, the tether radius is too large for the computation and could not get any resolution. In Cases 8 and 9, electron temperature is changed. Together with the nominal case, it is seen that higher electron temperature results in lower current collection. In Cases 10 and 11, ion temperature is changed.

Unlike electron temperature, ion temperature does not seem to have any effects on the current collection. In Case 12, the ED tether is inclined at an angle of 30 degree to the vertical. This is equivalent to a lower ion ram energy. In Cases 13 and 14, we look at some combined effects of electron temperature and the tether potential. From comparison of these cases with Case 3, it is also seen that the higher electron temperature lowers the current collection. Finally Case 15 is chosen to check the case of high tether potential, since in Case 4 the computation does not seem to provide a correct value. With a small radius of the tether we reduce the size of the computational domain in order to contain the physics correctly inside the domain. In the following sections, we go through each case and the relation between the plasma properties and the current collection is discussed.

5.2 Case 1 : Magnetic Field ($B = 0.1(G)$)

Case 1 deals with a lower magnetic field, $B = 0.1(G)$. This case is checked to see the limit of the three dimensional injection method discussed in Chapter 3. We discussed that, in order to use the 3D injection method, the size of the computational domain has to be large enough so that the magnetic effect on the electrons' motion overwhelms the electrostatic effect by the high tether potential. More specifically,

$$\frac{m_e\sqrt{\frac{2e\phi}{m_e}}}{eB} < L_x. \tag{5.1}$$

In Figure 5-1, instantaneous field quantities of Case 1, with the lower magnetic field ($B = 0.1(G)$) than the nominal case, are shown. The first thing to note is the potential profile (Figure 5-1(f)). The "potential wing" does not spread as wide as that in the nominal case. The magnetic effect is so small that many electrons can reach the tether surface from the ram side directly without completing one gyration. In Figure 5-2(a), a few electron trajectories coming from the ram side are shown. Unlike the nominal case, most electrons are attracted by the electrostatic force by the tether as soon as they enter the computational domain. In this sense, we have to doubt the

validity of the three-dimensional injection of electrons at the computational domain. Current collection is 2.6 times larger than the 2D OML current collection as shown in Figure 5-2(b), which is the same current collection as in the nominal case.

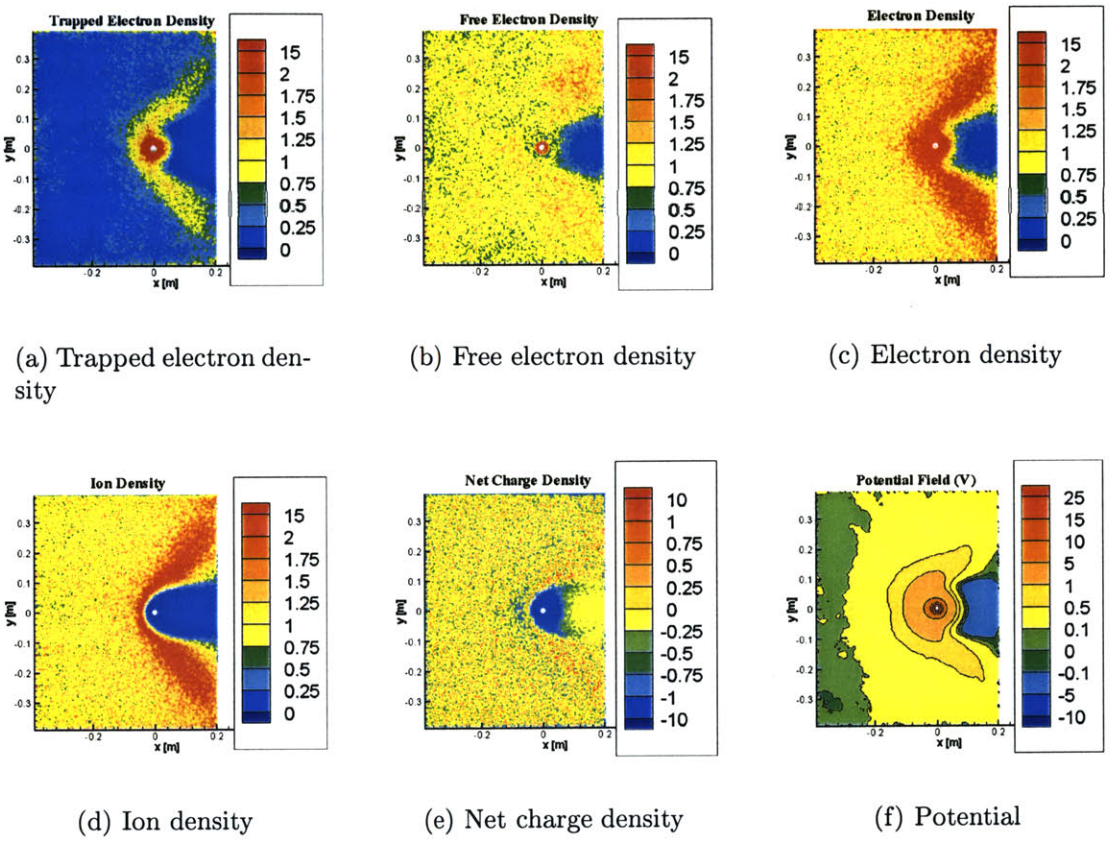

(a) Trapped electron density

(b) Free electron density

(c) Electron density

(d) Ion density

(e) Net charge density

(f) Potential

Figure 5-1: Instantaneous maps of field quantities in Case 1 ($B = 0.1(G)$)

5.3 Case 2 : Magnetic Field ($B = 0.6(G)$)

Case 2 deals with a larger magnetic field, $B = 0.6(G)$. Since the magnetic field is stronger than in the nominal case and the 3D injection method was justified for the nominal case in the previous chapter, we can safely state that the magnetic effect on electrons at the computational boundary is dominant enough for the use of the 3D injection method.

Figure 5-3(a) and (b) show typical electron trajectories from the ram side. The

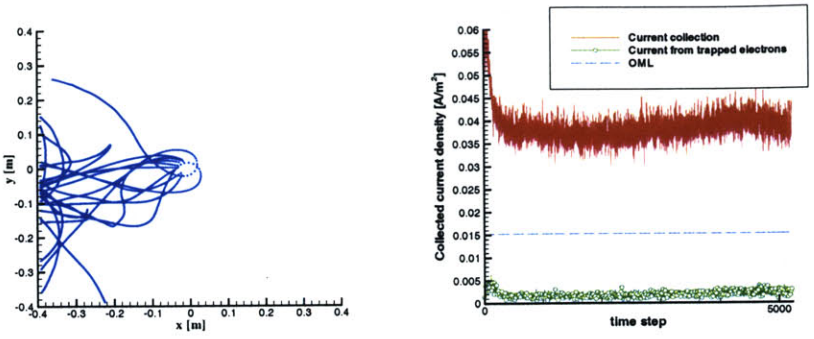

(a) Electron trajectory

(b) Current Collection

Figure 5-2: Electron trajectories and current collection in Case 1 ($B = 0.1(G)$)

trajectory shown in (a) shows an electron that is injected in the ram side and continues to gyrate away through the upper side of the computational boundary. This shows the strong magnetic effect on the electrons in the region. Figure 5-3(b) shows the trajectory of an electron which is captured by the tether located at $(0, 0)$. The electron seems to be controlled by the electrostatic force. However, as shown in Figure 5-3(c), the electron gyrates until it reaches very close to the tether. Therefore the magnetic effect dominates up to the immediate vicinity of the tether. Due to the potential hump and the electron containment, the electron sloshes more frequently as it gets closer to the tether (it is seen in the time history of the y-component of the electron position in Figure 5-3(c)).

Now let us see the effect of the higher magnetic field on macroscopic plasma quantities. Instantaneous field quantities are shown in Figure 5-4. The potential profile in Figure 5-4(f) shows the magnetic wings spreading wider than in the nominal case. This reflects the fact that electrons' motions are restricted along the magnetic field. We can notice that the potential contour line of $\phi = 0.1(V)$ is more straight and closer to the tether than that of the nominal case. This is considered to be due to the smaller Larmor radius, $\sim O\left(\frac{mw_\perp}{eB}\right)$, and the larger Lorentz force, $ew_\perp B$, for the larger magnetic field. In order for an electron in the frontal region of the tether to start feeling the electrostatic effect, it needs to be closer to the tether than in the

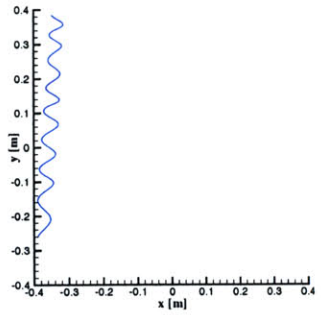

(a) Electron trajectory

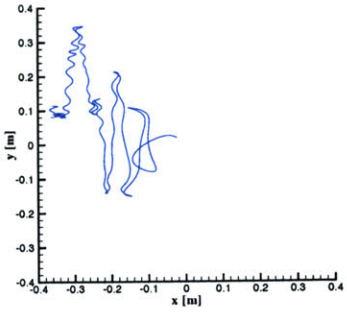

(b) Electron trajectory

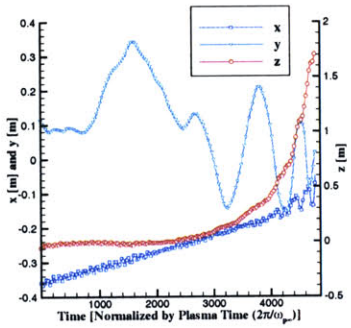

(c) History of the position (x, y, z) of the electron shown in (b)

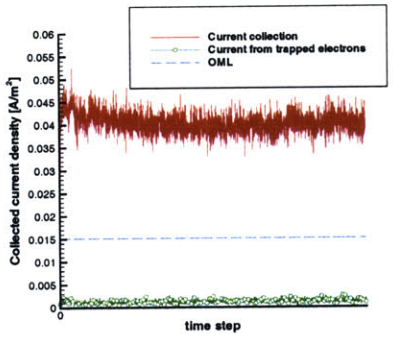

(d) Current collection

Figure 5-3: Electron trajectories and current collection in Case 2 ($B = 0.6(G)$)

nominal case. That is, electron capture by the magnetic wings (the pre-sheath), whose fundamental mechanism is to attract more electrons to obtain the quasi-neutrality, is limited to a smaller region in front. In addition, the larger magnetic field renders stronger the magnetic force, $ew_{\perp}B$, against the electrostatic force, keeping electrons gyrating around the magnetic field line. Therefore the magnetic wings, not being able to obtain enough electrons from the ram side for quasi-neutrality, extend farther along the magnetic field.

Another point to note is the ion density shown in Figure 5-4(d). Because of the widely spread magnetic wings, ion's caustic line also spreads. Ions which are slowed down in front of the tether due to the high potential are deflected to the sides, where

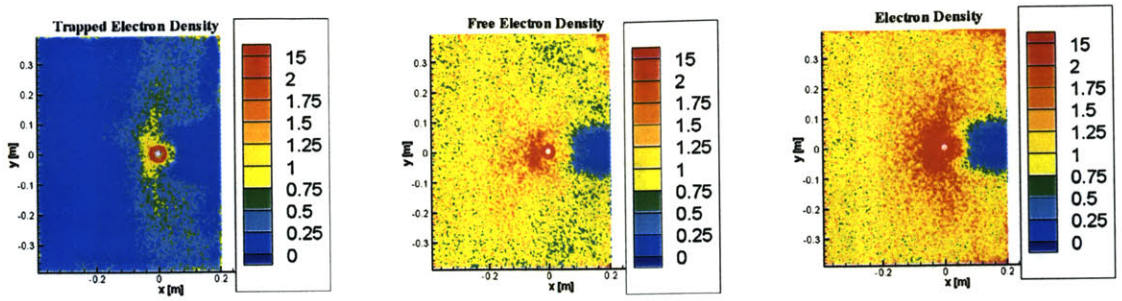

(a) Trapped electron density

(b) Free electron density

(c) Electron density

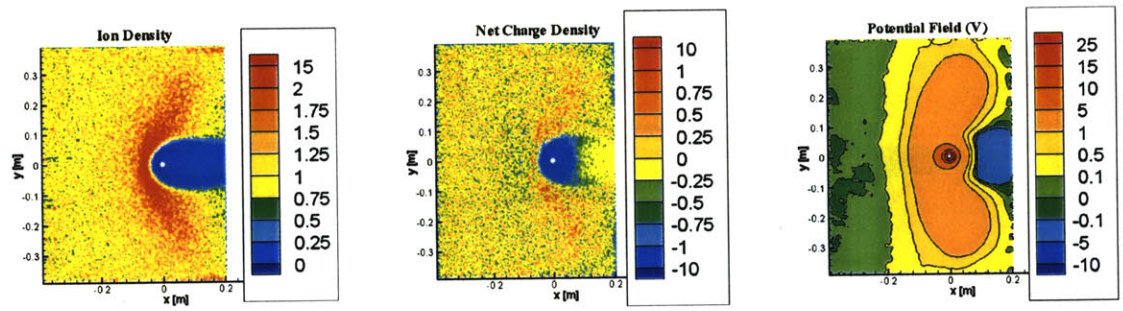

(d) Ion density

(e) Net charge density

(f) Potential

Figure 5-4: Instantaneous maps of field quantities in Case 2 ($B = 0.6(G)$)

they again experience higher potential (magnetic wings) than the nominal case. The ions are then deflected further outside, giving rise to the ion density profile.

The current collection shows the same value as in the nominal case in Figure 5-3(d). From the result of the nominal case and the result here, we may expect that the different magnetic field in this range ($B = 0.3 \sim 0.6(G)$) has little direct impact on the current collection. Of course, this comparison is at a fixed potential bias, but the bias will change when flying through variations of the magnetic field. The effects of potential bias are examined next.

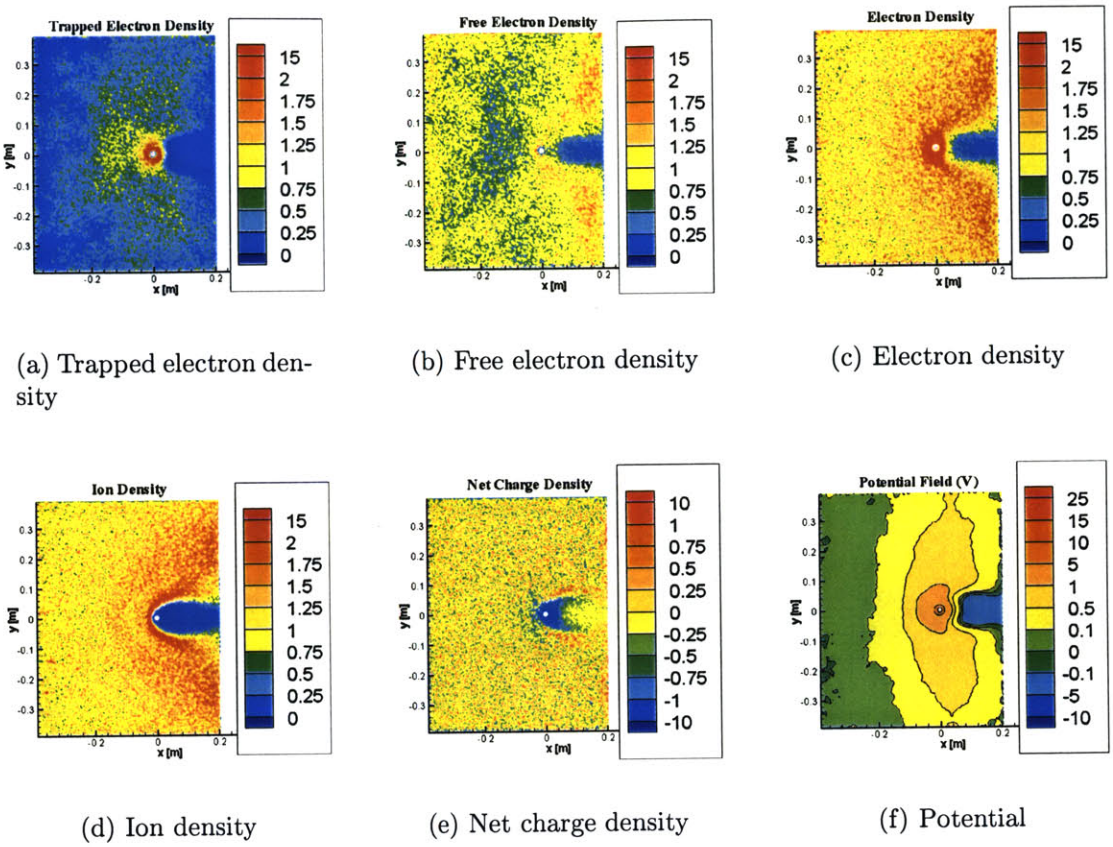

(a) Trapped electron density

(b) Free electron density

(c) Electron density

(d) Ion density

(e) Net charge density

(f) Potential

Figure 5-5: Instantaneous maps of field quantities in Case 3 ($\phi_p = 10(V)$)

5.4 Case 3 : Tether Potential ($\phi_p = 10(V)$)

In Case 3, the tether potential is lowered to $\phi_p = 10(V)$ from the nominal case where we had $\phi_p = 25(V)$. As the tether potential is now just twice as large as the ion ram energy, the ion peak density is closer to the tether. The wake behind the tether is also smaller (Figure 5-5(f)). We can also notice the magnetic wings, which appear because, even though the magnetic field is the same as in the nominal case, the magnetic effect is relatively stronger than the electrostatic effect.

As the tether potential is lowered, but not the magnetic field, the electron's motion is now dominated by the magnetic effect. In Figure 5-6(a) and (b), two electron trajectories are shown. Figure(a) shows an electron with a relatively low energy, showing the electron containment. Figure(b) shows a fast electron trajectory passing near the tether. In both cases, electrons are not captured by the tether. As in the

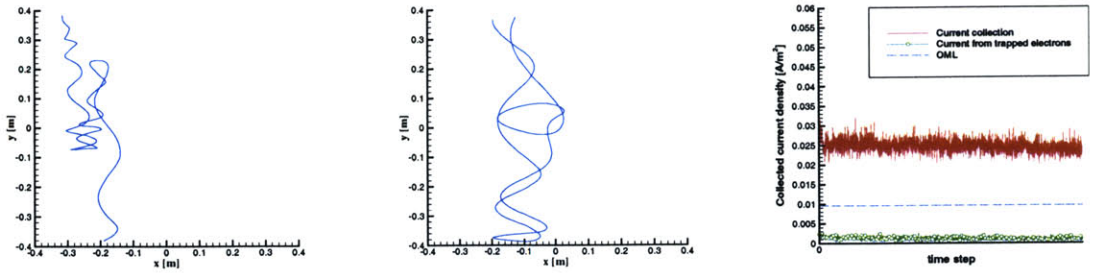

(a) Electron trajectory (b) Electron trajectory (c) Current Collection

Figure 5-6: Electron trajectories and current collection in Case 3 ($\phi_p = 10(V)$)

case of (b), electrons are not so influenced by the electrostatic field as in the nominal case. Electrons do feel the electrostatic force, but the magnetic effect is still strong even in the vicinity of the tether, which helps electrons escape from the electrostatic effect.

The current collection in Figure 5-6(c) is seen to be 2.4 times larger than the 2D OML, a slightly lower ratio than the nominal case. This is thought to be due to the stronger magnetic effect *in the vicinity of* the tether, which helps electrons escape from the potential hump created by the tether potential. In addition, of course, the OML current is itself lower by $\sqrt{10/25}$.

5.5 Case 4 : Tether Potential ($\phi_p = 100(V)$)

In Case 4, the tether potential is raised to $\phi_p = 100(V)$. The current collected did not converge in this case in computation, but stayed around the 2D OML current (Figure 5-7(b)). The high potential on the tether increases the size of the sheath, pushing the ion caustic line, $\sim 5(V)$, farther ahead as seen in Figure 5-8(f). This enlarges the wake region, creating a potential barrier and keeping electrons from approaching from the wake side.

This computation may not be complete due to the lack of space to contain the ion caustic line. At the top and bottom sides of computational boundary, incoming ions are assumed to have a non-deflected Maxwellian distribution, which is obviously

contradictory to the numerical result here. Computations with a larger domain are suggested as future work.

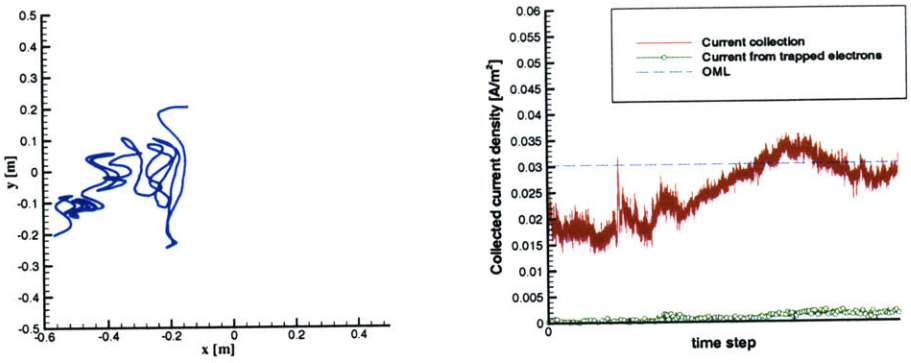

(a) Electron trajectory

(b) Current collection

Figure 5-7: Electron trajectory and current collection in Case 4 ($\phi_p = 100(V)$)

5.6 Case 5 : $\frac{\text{Tether Radius}}{\text{Debye Length}}$ $(\frac{d}{d_D} = 0.3)$

Case 5 deals with a smaller tether radius or larger Debye length. In the 2D OML theory, the nominal case $\frac{d}{d_D} = 1$ is already in the OML regime and the smaller tether radius or a larger Debye length does not change the current as the 2D OML is the upper limit. It is obvious by now that the current collection in the magnetized flowing plasma is more than the 2D OML. The question is then whether $\frac{d}{d_D} = 1$ provides the upper limit of the current collection or not? The answer is seen in Figure 5-9(c). The current collection is $\sim$ 2.6 times larger than the 2D OML, which is the same ratio as the nominal case. The large noise is due to the small total area of the collecting surface of the tether.

In Figure 5-9(a) and (b), a number of electron trajectories from the ram side and from the upper side are shown. Figure 5-9(a) shows electron trajectories from the ram side. The electron containment is also recognized. In general, it is not very different from the nominal case, showing a dominant magnetic effect at the boundary. Figure (b) shows several electron trajectories from the upper side. These electron trajectories

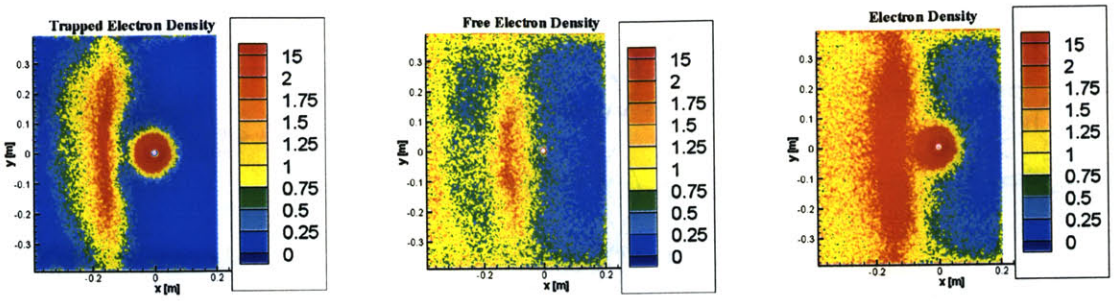

(a) Trapped electron density

(b) Free electron density

(c) Electron density

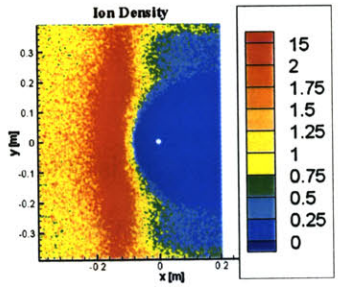

(d) Ion density

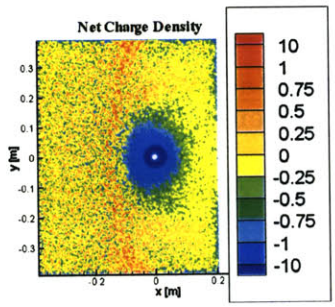

(e) Net charge density

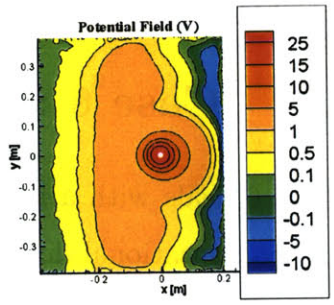

(f) Potential

Figure 5-8: Instantaneous maps of field quantities in Case 4

also indicate that electrons are under the magnetic effect in most of the frontal region. Figure 5-10(f) shows an instantaneous potential profile, which also indicates that the electrostatic effect does not reach farther out in front, compared to the nominal case.

The effect of the small tether radius is seen in the ion density in Figure 5-10(d). The ion peak density and the ion caustic line are in a compact region. Accordingly the magnetic wings are smaller than the nominal case, meaning that the electrostatic effect does not reach as far out. This allows more electrons to pass by the tether as seen in Figure 5-9(b). This lowers the total current collection but the current density is the same as in the nominal case.

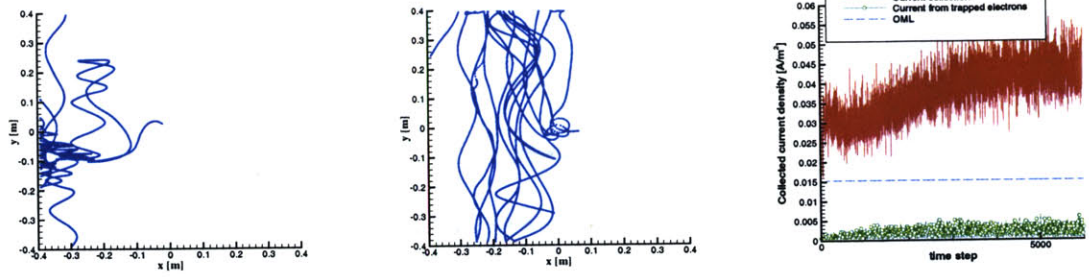

(a) Electron trajectory (b) Electron trajectory (c) Current collection

Figure 5-9: Electron trajectories and current collection in Case 5 ($\frac{d}{d_D} = 0.3$)

5.7 Case 6 : $\frac{\text{Tether Radius}}{\text{Debye Length}}$ $(\frac{d}{d_D} = 3)$

Case 6 deals with a larger tether radius $\frac{d}{d_D} = 3$. From Figure 5-11, it is seen that the computational domain was not large enough to contain the ion caustic line. As in Case 4, ion deflection is so considerable that the no-deflection assumption at the top and bottom sides is contradicted. The current collection in this computation is shown in Figure 5-12, and is reduced to 1.83 times the 2D OML value.

5.8 Case 7 : $\frac{\text{Tether Radius}}{\text{Debye Length}}$ $(\frac{d}{d_D} = 10)$

This case required a large grid system. I ran out of memory and could not run it.

5.9 Case 8 : Electron Temperature $(T_e = 0.05(eV))$

Case 8 deals with a lower electron temperature, $T_e = 0.05(eV)$. Figure 5-13 shows instantaneous maps of field quantities. The direct effect of the lower temperature on plasma quantities appears in the Debye length, $d_D = \sqrt{\frac{\epsilon_0 \kappa T_e}{ne^2}}$, the electron Larmor radius, $r_L = \frac{m_e w_\perp}{eB}$ and the Lorentz force acting on an electron, $F_{Lorentz} = q w_\perp B$. The electron Larmor radius is smaller, as in Case 2. But the Lorentz force also becomes weaker, unlike the case of stronger magnetic field in Case 2. Even though the Larmor radius is small, the electrostatic force, which is now stronger against the magnetic

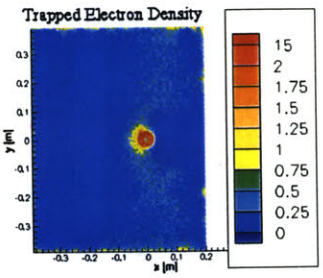

(a) Trapped electron density

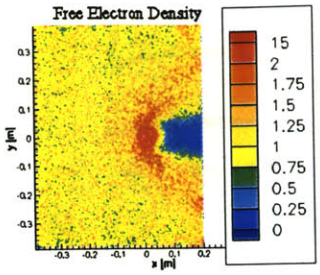

(b) Free electron density

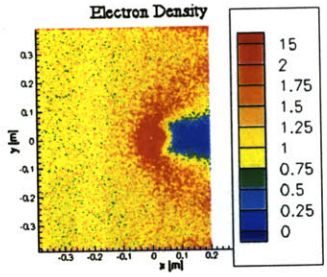

(c) Electron density

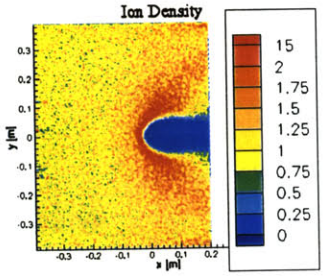

(d) Ion density

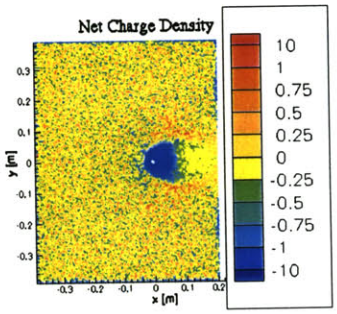

(e) Net charge density

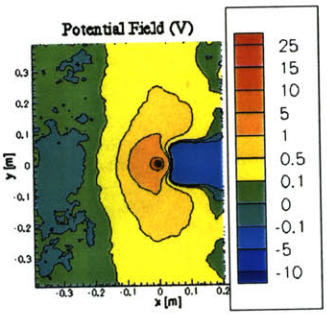

(f) Potential

Figure 5-10: Instantaneous maps of field quantities in Case 5 ($\frac{d}{d_D} = 0.3$)

force than in the nominal case, attracts electrons from the frontal region

Among the three parameters, the Lorentz force has the largest impact on electron trajectories. Figures 5-14(a) and (b) show two typical trajectories of electrons coming from the ram side. Figure 5-14(a) indicates that electrons start being under the influence of the electrostatic force at a more distant point than in the nominal case, approaching toward the tether. In other words, as the thermal speed of the electron is small, the electron containment happens even against a small electric field. Figure 5-14(b) shows an electron trajectory dominated by the electrostatic effect. It sloshes several times before the tether captures it. The sloshing motion in this particular case happens to be in phase with the electron cyclotron motion when it makes "U-turns" (Figure 5-14(d)).

The current collection shown in Figure 5-14(c), is seen to be $\sim$ 3.0 times larger

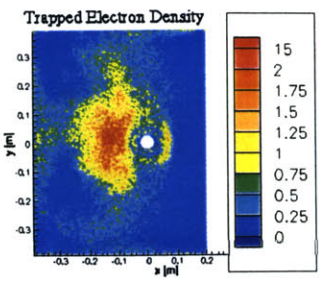

(a) Trapped electron density

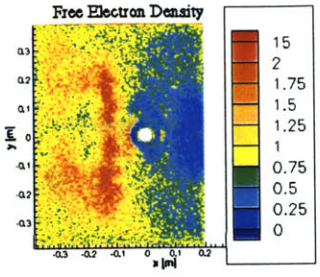

(b) Free electron density

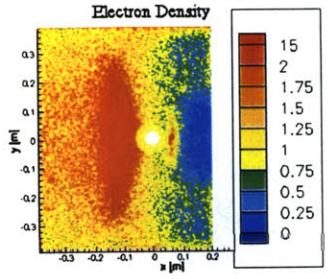

(c) Electron density

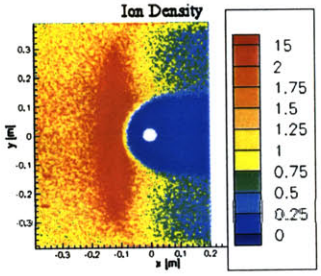

(d) Ion density

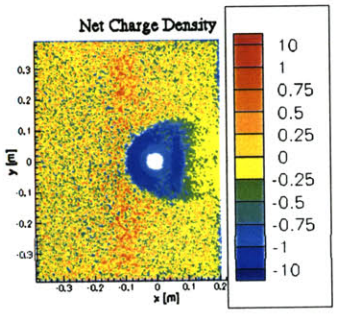

(e) Net charge density

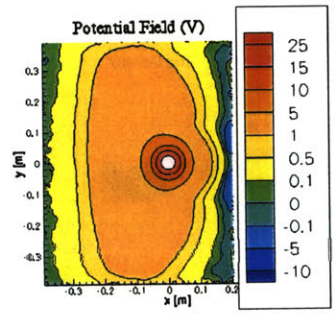

(f) Potential

Figure 5-11: Instantaneous maps of field quantities in Case 6 ($\frac{d}{d_D} = 3$)

than the 2D OML. The reason for this larger current collection may be the relatively large number of contained electrons in the potential hump. As the electron temperature is low, the electron's longitudinal kinetic energy, $\frac{1}{2}m_e w_y^2$, is on average low as well. As discussed in Chap. 4, an electron with a lower longitudinal kinetic energy is more likely to be contained in the potential hump, and therefore more likely to be captured by the tether.

5.10 Case 9 : Electron Temperature ($T_e = 0.2(eV)$)

Case 9 deals with a higher electron temperature. As the electron temperature becomes larger, the electron Larmor radius gets larger. This allows an electron to cover a wider region within one gyration. Therefore, an electron at a more distant point in the ram

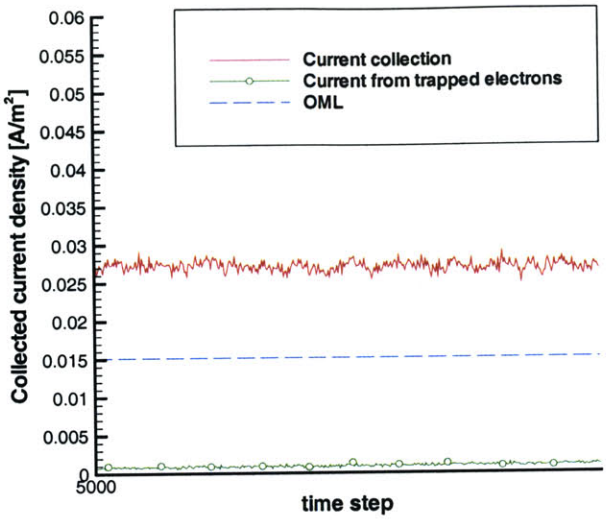

Figure 5-12: Current Collection in Case 6 ($\frac{d}{d_D} = 3$)

region may enter the potential hump, and the potential hump stretches ahead a little bit, trying to attract more electrons from the ram side (Figure 5-15(f)). Note that in case 8 where the electron temperature (and hence the Larmor radius) is smaller, thus smaller Larmor radius, the potential hump mainly stretches to the magnetic wings, not towards the ram side.

The current collection is 2.16 times larger than the 2D OML current (Figure 5-16). Following the same argument given in the last section on Case 8 ($T_e = 0.05(eV)$), we can ascribe the lower current collection to the non-contained electrons, which are attracted to the ion peak density to obtain the quasi-neutrality, but escape outside the potential hump. A certain number of electrons are attracted due to the tether potential, and additional electrons are added because there is the ion peak density in front of the tether. When the electron temperature is low (Case 8), there are relatively more contained electrons coming from the ram side, and most of them are captured by the tether. On the other hand, when the temperature is high as in this case, fewer electrons are contained, and due to the larger thermal motion, electrons are coming from more random directions to the ion peak density. These electrons are

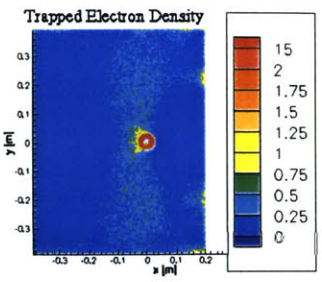

(a) Trapped electron density

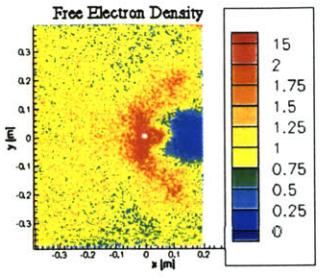

(b) Free electron density

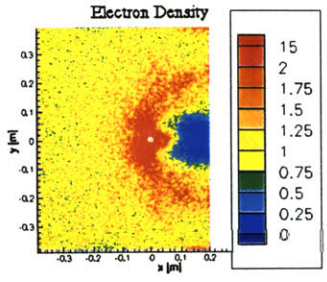

(c) Electron density

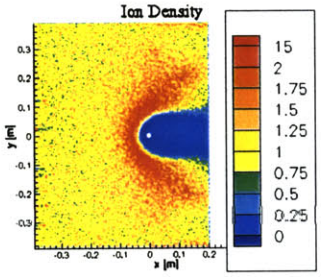

(d) Ion density

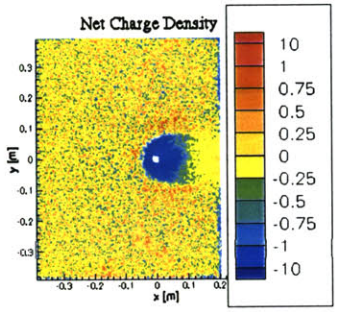

(e) Net charge density

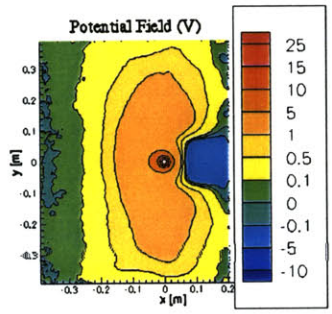

(f) Potential

Figure 5-13: Instantaneous maps of field quantities in Case 8 ($T_e = 0.05(eV)$)

just passing through the ion peak density and are more likely to go away than to get captured by the tether.

5.11 Case 10 : Ion Temperature ($T_i = 0.05(eV)$)

Case 10 deals with a lower ion temperature, $T_i = 0.05(eV)$. The current collection, Figure 5-17 (b), is 2.67 times larger than the 2D OML current collection, which is the same as the nominal case. It is also seen from Figure 5-18 that the plasma profile is not very different from the nominal case. Under the mesothermal condition, the ion distribution is mainly determined by the plasma flow, U_{tether}. The effect of the lower ion temperature should appear in the thickness of the ion peak density and in the size of the wake. The ion peak density is seen in front of the tether where the ion flow "stagnates" at the potential equivalent to the ion ram energy. As the ion

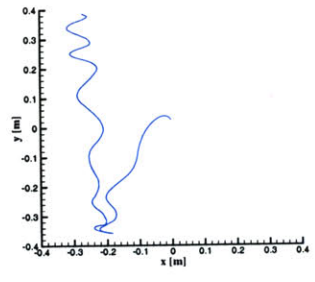

(a) Electron trajectory

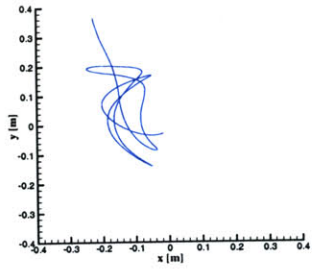

(b) Electron trajectory

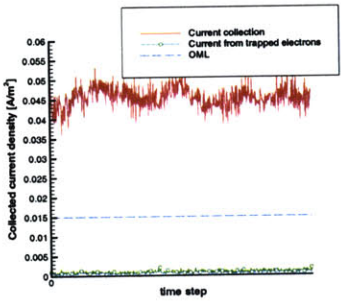

(c) Current collection

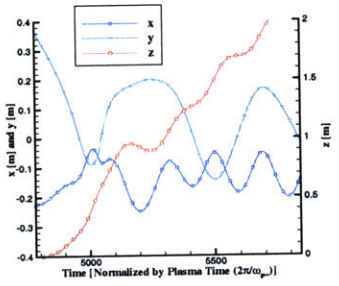

(d) History of the position (x, y, z) of the electron in (b)

Figure 5-14: Electron trajectories and current collection in Case 8 ($T_e = 0.05(eV)$)

velocity distribution has a narrower spread for the lower ion temperature, the ion peak density also has a narrower spread. However, this effect is so small that we do not see the difference in the ion density profile (Figure 5-18(d)). The wake closes itself by the ion thermal motion and the electric field created by the non-quasi-neutrality in the wake, the distance from the tether required to close the wake is longer for the lower ion temperature. As the size of the computational domain is not large enough to contain the whole wake, this effect is not seen in our computation.

A lower ion temperature does not affect the potential profile considerably, and does not affect electron trajectories. Therefore the current collection does not change from the nominal case.

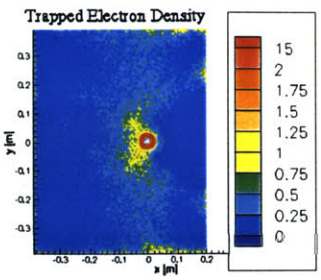

(a) Trapped electron density

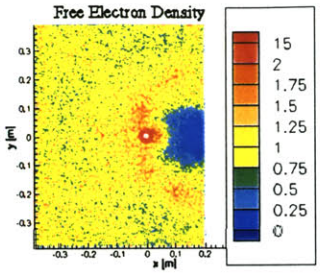

(b) Free electron density

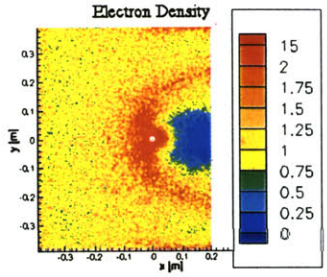

(c) Electron density

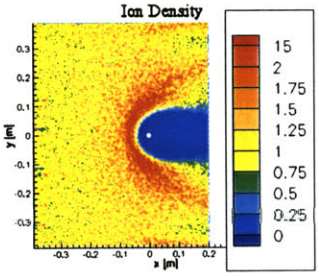

(d) Ion density

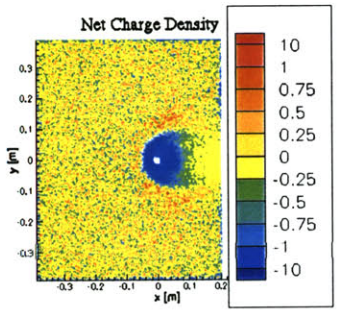

(e) Net charge density

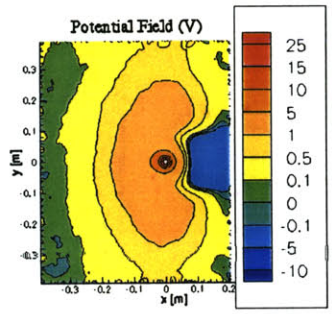

(f) Potential

Figure 5-15: Instantaneous maps of field quantities in Case 9 ($T_e = 0.2(eV)$)

5.12 Case 11 : Ion Temperature ($T_i = 0.2(eV)$)

Case 11 deals with a higher ion temperature, $T_i = 0.2(eV)$. As it was discussed in the previous section for $T_i = 0.05(eV)$, the ion temperature itself does not affect the electron behavior a lot. The current collection is still the same as the nominal case (Figure 5-19(b)), and the electron containment as seen in the nominal case is also seen in Figure 5-19(a). The effect of the higher ion temperature may be recognized in the thickness of the ion peak density in this case. The thickness of the higher ion density region in front of the tether (Figure 5-20(d)) is larger than that of Case 10 (Figure 5-18(d)).

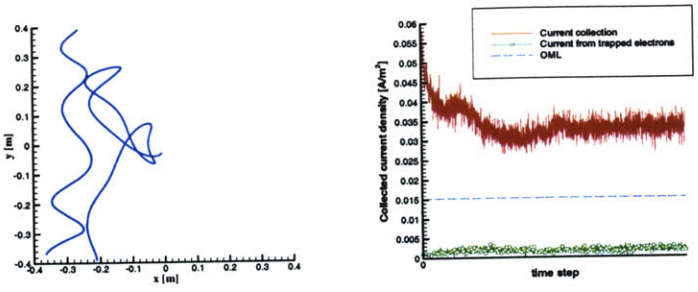

(a) Electron trajectory (b) Current collection

Figure 5-16: Electron trajectories and current collection in Case 9 ($T_e = 0.2(eV)$)

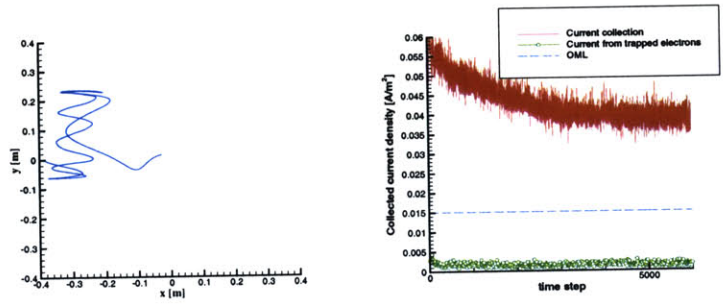

(a) Electron trajectory (b) Current collection

Figure 5-17: Electron trajectories and current collection in Case 10 ($T_i = 0.05(eV)$)

5.13 Case 12 : Tilted Tether ($\theta = 60(\text{deg})$)

When the tether is traveling at an angle to its direction of motion other than the right angle, the projection of plasma behavior to the plane perpendicular to the tether becomes of practical importance. When the angle is $\theta = 60(\text{deg})$, we can consider this problem as $\theta = 90(\text{deg})$ (nominal case) with the ion ram speed of $U \rightarrow U \sin 60$. The major difference in this case from others is the current collection (Figure 5-21(c)), which shows the current collection just above the 2D OML.

From Figure 5-22, we notice that the ion peak density in front of the tether is located farther away from the tether than the nominal case (Fig. (d)). Accordingly the potential hump and the magnetic wings are shifted ahead. Electrons are seen to be contained in the potential hump (Figure 5-21 (a) and (b)). The fact that the

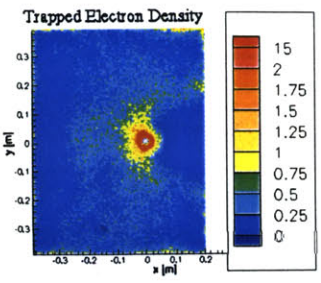

(a) Trapped electron density

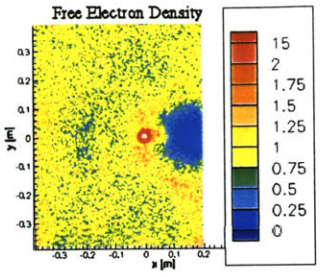

(b) Free electron density

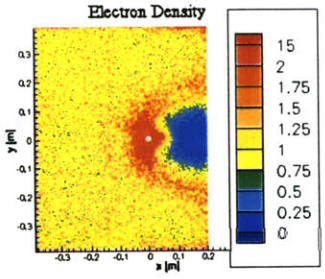

(c) Electron density

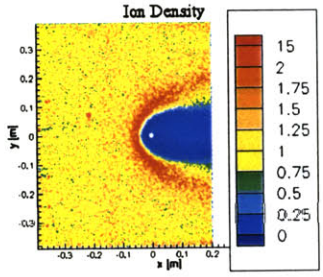

(d) Ion density

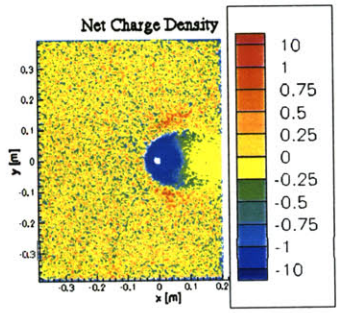

(e) Net charge density

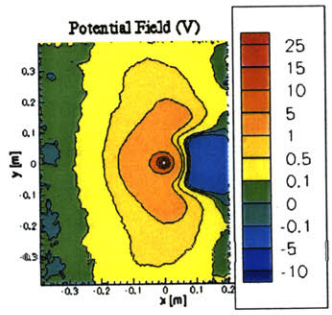

(f) Potential

Figure 5-18: Instantaneous maps of field quantities in Case 10 ($T_i = 0.05(eV)$)

wake increases its size, as the magnetic wings move ahead, and reaches the sides of the tether keeps electrons from approaching from this direction. Therefore, although the current collection is very close to the 2D OML, the mechanism is very different from the 2D OML theory. An electron's motion is governed by the 3D magnetic effect until it enters the sheath where the 2D electrostatic effect dominates. However, the wake covering not only the back of the tether but also the sides creates a potential barrier, preventing electrons from entering the sheath, and thus lowering the current collection.

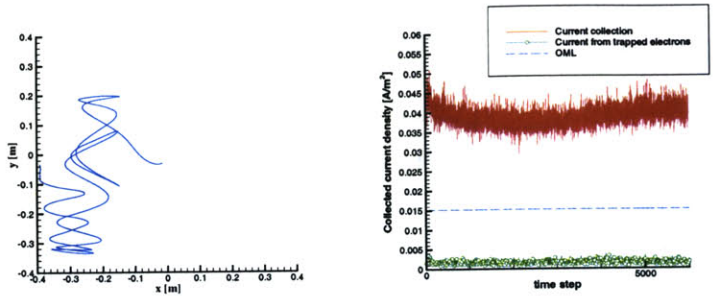

(a) Electron trajectory (b) Current collection

Figure 5-19: Electron trajectories and current collection in Case 11 ($T_i = 0.2(eV)$)

5.14 Case 13 : Electron Temperature ($T_e = 0.05(eV)$) & Tether Potential ($\phi_p = 10(V)$)

Case 13 deals with a lower electron temperature, $T_e = 0.05(eV)$, and a lower tether potential, $\phi_p = 10(V)$. The current collection to the tether is 2.5 times larger than the 2D OML (Figure 5-23). As the temperature decreases, the magnetic effect becomes weaker. And as the tether potential decreases, the electrostatic effect also becomes weaker. The reason for the current collection being lower than the nominal case may be ascribed to the relatively weak electric field around the tether. In the nominal case, when an electron starts being attracted by the electric field due to the tether potential, the electron's gyration is overwhelmed by the electrostatic force in the vicinity of the tether and the electron is captured. In Case 13, due to the low potential on the tether, the electrostatic force does not completely overwhelm the magnetic effect. Therefore, there are some electrons which orbit around the tether due to the electric field, but escape from the orbiting motion by the gyration before they are captured by the tether (Figure 5-23(b)).

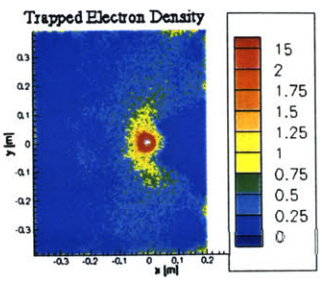

(a) Trapped electron density

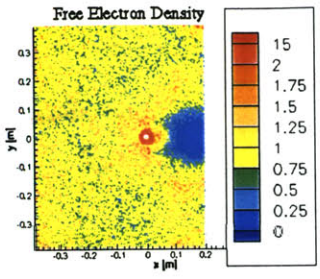

(b) Free electron density

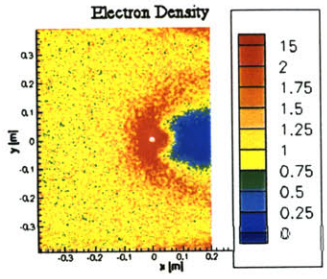

(c) Electron density

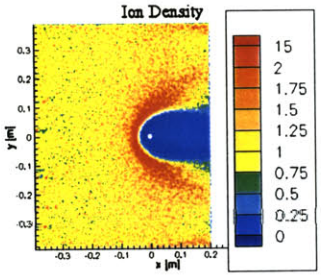

(d) Ion density

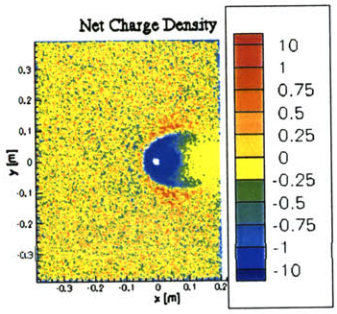

(e) Net charge density

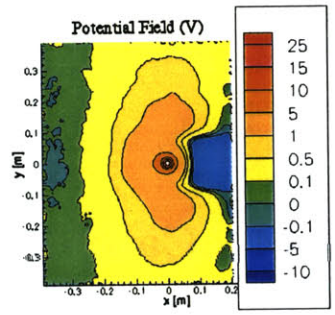

(f) Potential

Figure 5-20: Instantaneous maps of field quantities in Case 11 ($T_i = 0.2(eV)$)

5.15 Case 14 : Electron Temperature ($T_e = 0.2(eV)$) & Tether Potential ($\phi_p = 10(V)$)

Case 14 deals with a higher electron temperature, $T_e = 0.2(eV)$, and a lower tether potential, $\phi_p = 10(V)$. Due to faster electron velocity associated with the larger temperature and the low tether potential, electrons' motions are mostly dominated by the magnetic effect. As in Nominal case, Case 9 and 10, we can see the effect of the electron temperature on the current collection. Comparing Case 3, 13 and 14, it also indicates that the higher electron temperature gives rise to the lower current collection (2.3 times OML, see Figure 5-25). The mechanism of such a trend is considered to be the same. "Hotter" electrons are less likely to be contained in a potential hump, and less electrons are captured by the tether.

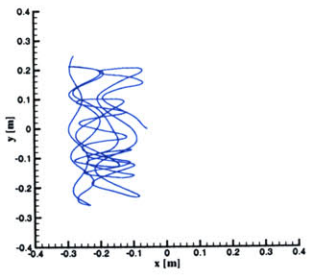

(a) Electron trajectory

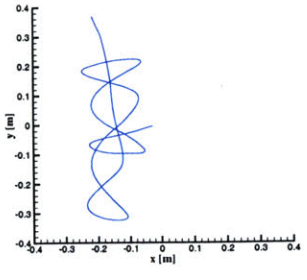

(b) Electron trajectory

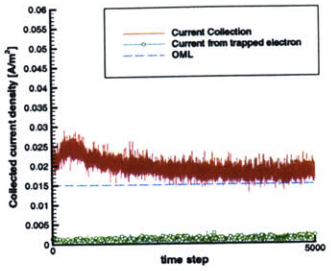

(c) Current collection

Figure 5-21: Electron trajectories and current collection in Case 12 ($\theta = 60(\text{deg})$)

The temperature dependence on the plasma is also seen in the potential profile in Figure 5-26(f). As the Larmor radius is large, the 2D effect becomes stronger. And electrons are attracted from a wider range of direction. Therefore the potential profile does not show magnetic wings, but the potential hump spreads more widely.

5.16 Case 15 : $\frac{\text{Tether Radius}}{\text{Debye Length}}$ $(\frac{d}{d_D} = 0.1)$ & Tether Potential $(\phi_p = 100(V))$

Cases 4, 6 and 12 showed a displacement of the ion caustic line further ahead in the ram side and suffered from the lack of space, both in front and on the sides of the computational domain. Since high voltage cases are more interesting regarding the actual ProSEDS plasma environment, we take a case of high tether potential with a smaller tether radius in order to get more reliable results than the abovementioned cases.

The computation actually took a considerable time for convergence, and the result shown here is believed not to be fully converged yet. Here we show a set of plasma quantities in a early stage of iteration (Fig. 5-27) at about timestep 2500 in Figure 5-29 (before the current collection increases) , and another set from a later iteration (Fig. 5-28) at timestep $>$ 5000 in Figure 5-29. Ion density profiles in both figures indicate that ions are moving very slowly but closing the wake. In Figure 5-27, the

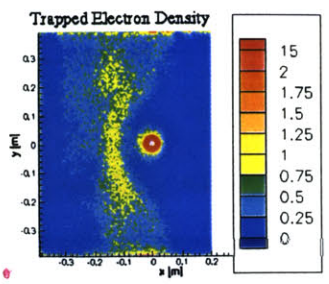

(a) Trapped electron density

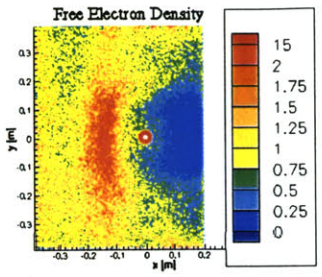

(b) Free electron density

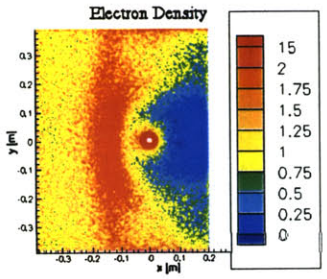

(c) Electron density

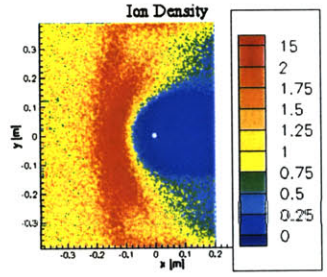

(d) Ion density

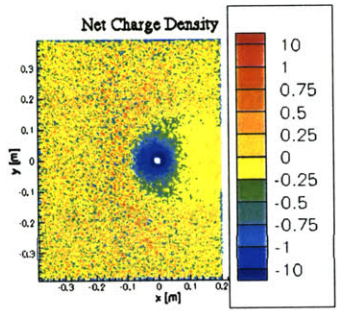

(e) Net charge density

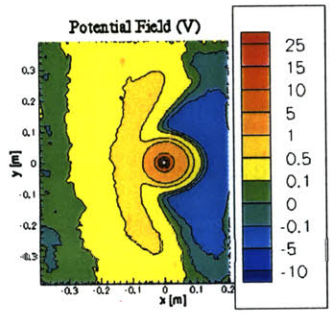

(f) Potential

Figure 5-22: Instantaneous maps of field quantities in Case 12 ($\theta = 60(\text{deg})$)

wake seen in the ion density originates from the tether and has a wide angle. In Figure 5-28, the wide angle wake flows downstream and a narrow wake appears near the tether. This is considered due to the very slow ions passing through the region. Due to this process, the wake region becomes small in the end and the potential barrier halfway around the tether on the wake side as seen in Cases 4, 6 and 12 disappears. Therefore more electrons are accessible to the tether from the back side, giving rise to higher current collection (Figure 5-29). Additional computation would be desirable to further define this case.

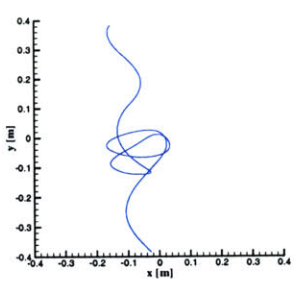

(a) Electron trajectory

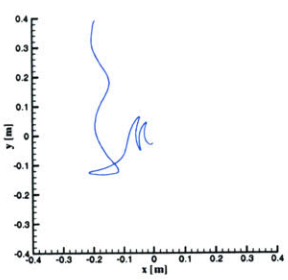

(b) Electron trajectory

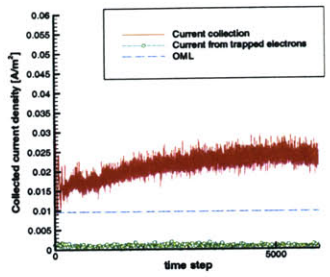

(c) Current collection

Figure 5-23: Electron trajectories and current collection in Case 13 ($T_e = 0.05(eV)$ & $\phi_p = 10(V)$)

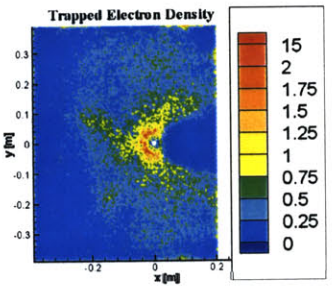

(a) Trapped electron density

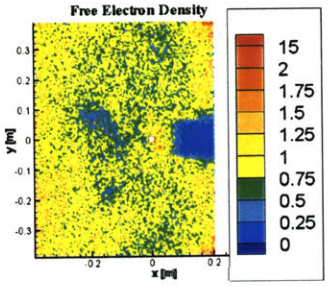

(b) Free electron density

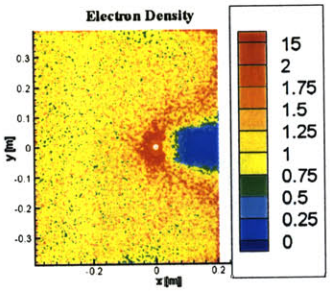

(c) Electron density

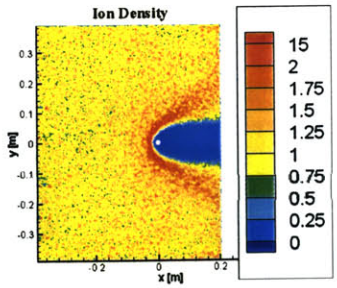

(d) Ion density

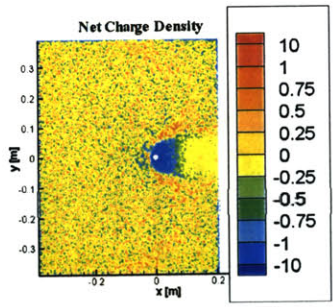

(e) Net charge density

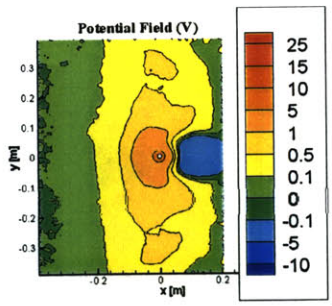

(f) Potential

Figure 5-24: Instantaneous maps of field quantities in Case 13 ($T_e = 0.05(eV)$ & $\phi_p = 10(V)$)

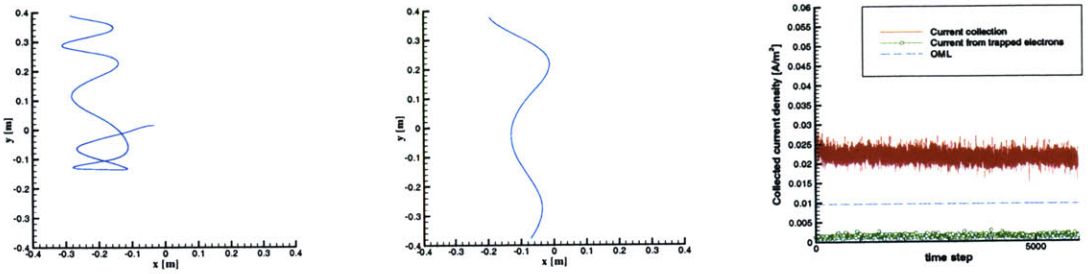

(a) Electron trajectory (b) Electron trajectory (c) Current collection

Figure 5-25: Electron trajectories and current collection in Case 14 ($T_e = 0.2(eV)\&\phi_p = 10(V)$)

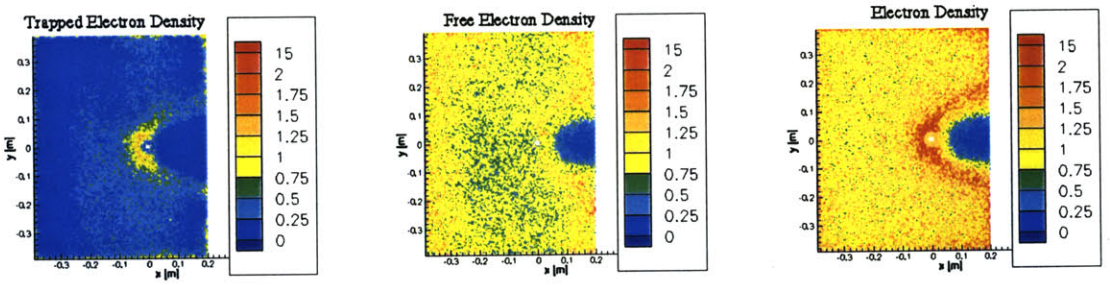

(a) Trapped electron density (b) Free electron density (c) Electron density

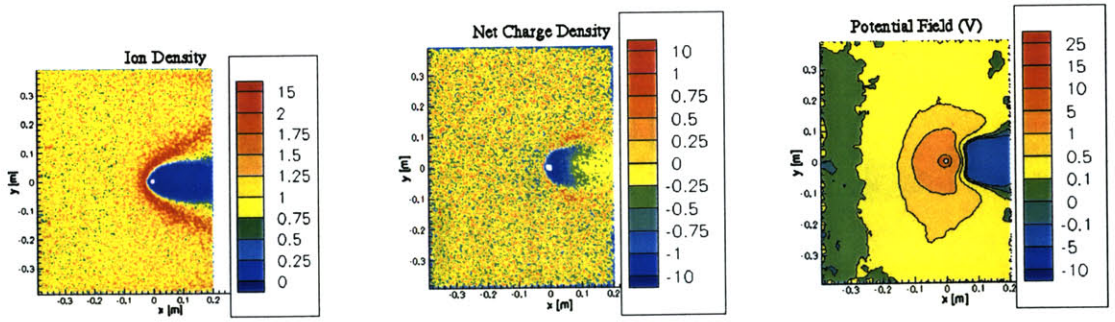

(d) Ion density (e) Net charge density (f) Potential

Figure 5-26: Instantaneous maps of field quantities in Case 14 ($T_e = 0.2(eV)\&\phi_p = 10(V)$)

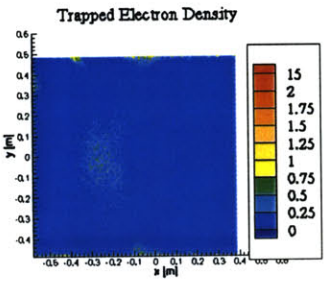

(a) Trapped electron density

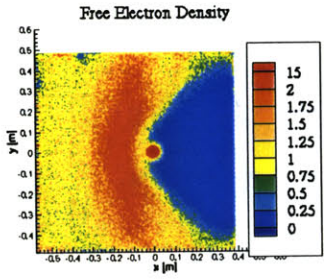

(b) Free electron density

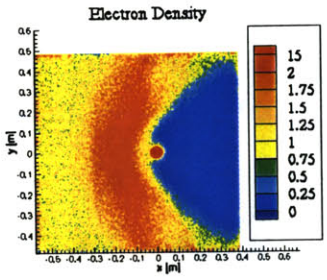

(c) Electron density

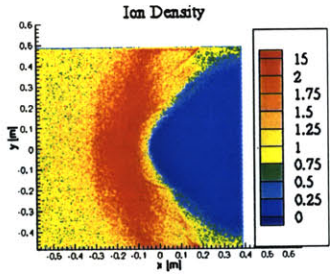

(d) Ion density

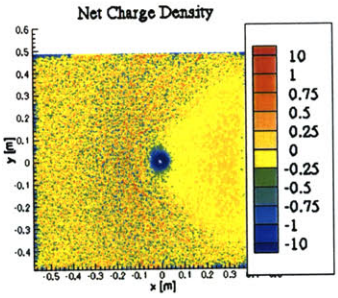

(e) Net charge density

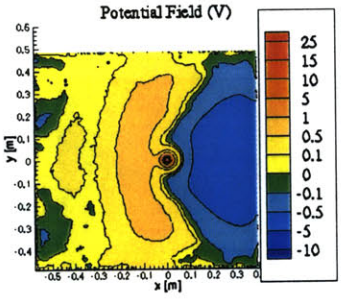

(f) Potential

Figure 5-27: Instantaneous maps of field quantities in Case 15 ($\frac{d}{d_D} = 0.1 \& \phi_p = 100(V)$)

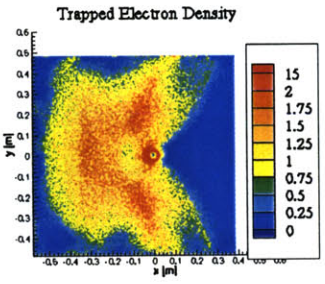

(a) Trapped electron density

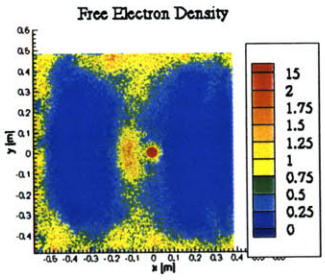

(b) Free electron density

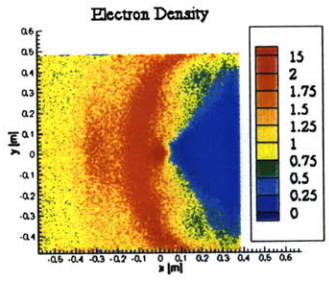

(c) Electron density

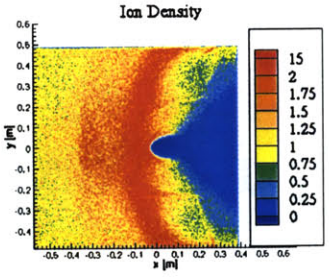

(d) Ion density

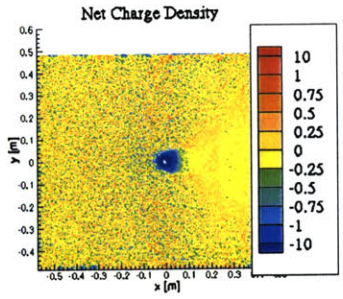

(e) Net charge density

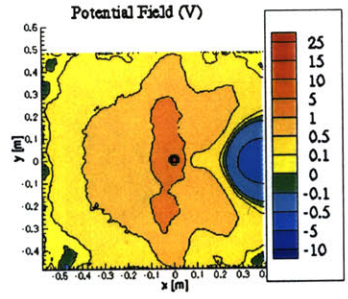

(f) Potential

Figure 5-28: Instantaneous maps of field quantities in later time in Case 15 ($\frac{d}{d_D} = 0.1 \& \phi_p = 100(V)$)

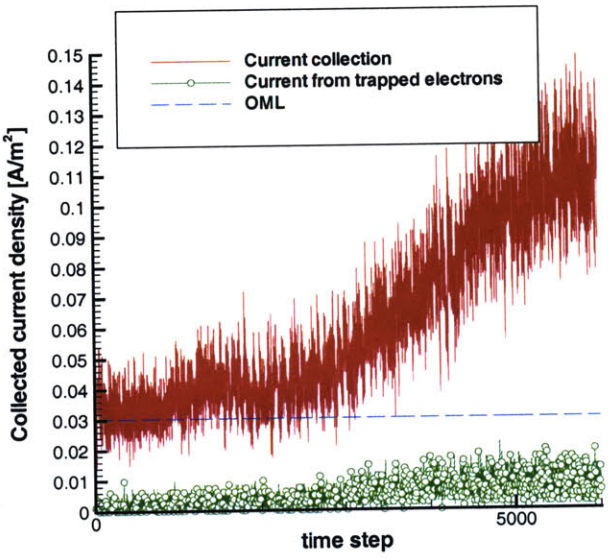

Figure 5-29: Current collection in Case 15 ($\frac{d}{d_D} = 0.1 \& \phi_p = 100(V)$)

Chapter 6

Conclusions and Recommendations

6.1 Summary and contributions

An electrodynamic (ED) tether has been considered as an alternative to conventional chemical or electric propulsions for spacecraft to perform their station-keeping maneuvers. A motion-induced electromotive force (EMF) or a power supply create a local potential difference between the tether and its ambient plasma, enabling the tether to collect electrons from one end. Collected electrons flow inside the tether, producing a current, and are then emitted from the other end of the tether to space. This uni-directional current is the key to the ED tether technology. The current interacts with the geomagnetic field across which the spacecraft is traveling and produces a Lorentz force either in the same or opposite direction of the tether motion, depending on the direction of the current. In order to efficiently increase the collected current, a bare tether which collects electrons through its own thin cylindrical surface has been preferred over an inefficient large spherical collector attached to the end of the tether.

In designing an ED Tether, it is important to estimate the current collection by the positively biased tether, as the amount of current directly affects the force acting on the tether. From the dimensional analysis, the current collection by a bare tether can be modeled as current collection by a positively biased cylindrical probe placed in a flowing magnetized plasma. Since the radius of the tether is smaller than the Larmor

radius and the electron thermal speed is much faster than the flow speed, magnetic and flowing effects were first considered negligible in the original attempts to estimate current collection, making the 2D Orbital-Motion-Limit (OML) theory a reasonable candidate for the current collection estimate. To obtain more reliable estimates in the current collection, a Particle-In-Cell (PIC) method has been developed and the flowing and magnetic effects have been incorporated into the calculation.

In order to improve the quantitative results, the quasi-neutrality condition applied at the computational boundary has been incorporated. The quasi-neutrality condition involves four particles densities; incoming electron and ion densities and outgoing electron and ion densities. The outgoing particle density is calculated numerically, and the incoming particle density is given as an analytical function of the local potential. The local potential is then solved for using the equation of the quasi-neutrality and used as an outside boundary condition. Given the outside boundary potential, electrons and ions are injected inside the computational domain. The accuracy of the condition has been verified elsewhere (author's M.S. thesis).

The method of injection is different depending on whether the plasma of interest is flowing and magnetized or not. Since the plasma is totally collisionless, at an injection point where the local potential is positive, electrons may behave two-dimensionally or three-dimensionally even though the problem of interest, a cylindrical probe, is geometrically two-dimensional. When there is no flow and no magnetic field, only electrons with sufficient energy perpendicular to the tether are injected. When there is flow and magnetic field, the injection of electrons can be three-dimensional (i.e., excluding only those with insufficient total energy), provided that the potential hump, i.e. the region with a positive potential, is large enough for electrons to gyrate, converting kinetic energy along the probe to that in a plane perpendicular to it, and vice versa. The presence of an absorbing probe or an externally applied potential field also modify the size of the region. The electron density resulting from 3D injection, which is larger than that from two dimensional injection, may be explained as follows; as electrons approach from infinity to a local point of positive potential, their acceleration and the geometrical concentration to the point cancel out their effects,

giving rise to the same density as at infinity. When a magnetic field is present and electrons gyrate, the gyration cyclically inter-converts the velocity along the tether and the perpendicular velocity. This cyclical conversion of the velocity components lowers the effect of acceleration in the perpendicular plane, rendering the geometrical effect stronger and giving rise to a higher density.

Several computations are performed with different plasma parameters. We chose one nominal case with typical plasma parameters seen in an ED tether operating in LEO. Other cases are defined by changing one or two parameters from the nominal case so that the effect of the changed parameter on current collection may be understood. The nominal case shows an enhanced current collection over the 2D OML. This result is reproduced with a frozen potential field with a slightly lower current collection (but still higher than the 2D OML). This indicates that the enhanced current collection results mostly from the three dimensional motion of electrons.

Several comparisons cases are run. Current collection is observed to decrease from the nominal case (but still around the 2D OML) in the following cases; (1) when the ion ram energy is lowered, (2) when the tether potential is very high (although there is same question about the convergence of this case) and (3) when the tether radius is increased. Things in common in these cases are the relative position of the ion peak density in front of the tether. Since the ion caustic line is located further ahead of the tether, the wake region behind the tether enlarges itself and creates a potential barrier near the rear part of the tether, keeping electrons from approaching to the tether from that direction.

Electron temperature has also some effects on the current collection. Higher electron temperature results in lower current collection. Electrons are attracted by two things. One is of course the tether potential, and the other is the ion higher density in the frontal area due to the scattering by the tether potential. Since the ion peak density is outside the sheath, the plasma attracts electrons in order to maintain the quasi-neutrality. There are two different types of electrons which are attracted by the potential hump created by the ion peak density. The first one is an electron coming along the magnetic field from outside the hump. Such an electron travels along the

magnetic field and enters the potential hump, accelerating along the magnetic field line. The other one is an electron which enters as the potential hump moves across the magnetic field. In this case, the electron accelerates across the magnetic field, and continues traveling inside the hump. When such an electron reaches the edge of the hump, if it does not have enough kinetic energy along the magnetic field, it reflects back to the potential hump. And the electron continues to stay inside the potential hump, sloshing up and down the magnetic field inside the hump. We call such an electron a "contained" electron as it is not trapped (with negative total energy). As the tether is located inside the potential hump, those contained electrons are very likely to be absorbed by it. When the electron temperature is lowered, there are more contained electrons as they do not have enough kinetic energy along the magnetic field in order to escape from the potential hump at the edge. Therefore more contained electrons contribute to a higher current collection.

Finally, the contributions of this work may be summarized as follows;

1. The quasi-neutrality condition has been formulated and incorporated into the treatment of boundary conditions in a PIC method. This condition removes the non-physical flux control as seen in previous works, and still provides stable calculations.

2. In space probe engineering, a negative bias or a slightly positive bias is the common situation. This work is one of the first to attack the interesting but complicated problem of a highly positive probe in space. Unlike a negatively biased probe, the attracted particles are electrons and the repelled ones are ions, which are so heavy that they break the symmetry of the distribution when the plasma is flowing. This also modifies electron motion and complicates the problem of current collection.

3. The 3D calculation of a local density and flux has been applied to a geometrically 2D problem. It has been considered reasonable to apply a 2D calculation to a geometrically 2D problem such as an ED Tether and the current collection has been considered to be limited by the 2D OML. However, in the presence

of magnetic field and plasma flow, in the steady state, the density and flux are limited by the 3D OML, which is much higher than the 2D OML. The magnetic field renders the motion of electrons partially three-dimensional. And the plasma flow helps fill with electrons the energy space which is vacant in the 2D case.

4. Some preflight predictions of current collection to the ProSEDS bare tether is provided. There is a certain possibility of getting a current collection higher than the 2D OML. As is mentioned later, the current collection seen in our computation may be over-estimated. However, as the non-magnetized case indicates (though the result is not totally valid), the current collection tend to be determined by the ion distribution. Therefore the current collection without the over-estimate would probably provide the same or close result with an aide of plasma fluctuations as seen in the unmagnetized flowing case, Cases 1 and 2.

6.2 Recommendations

The 3D calculation of the incoming density and flux at some part of the top and bottom sides is over-estimated. Electrons which have insufficient kinetic energy along the magnetic field, $\frac{1}{2}m_e w_y^2 < e\phi$, and therefore would not exist in a quiescent case, flow into the potential hump due to its motion. Therefore in order to obtain the 3D density and flux, all the electrons with insufficient kinetic energy along B should come from the front side of the hump, slosh along a magnetic field line and contribute to the 3D density calculation at a point of interest inside the potential hump. But this does not extend to those electrons entering the region through the top or bottom, and 3D injection in these regions should probably be restricted below 3D conditions.

If there is something like a tether inside the potential hump, which absorbs electrons, at points behind the tether the electron density would be lower than that given by the 3D calculation. In our computation, at the top and bottom sides, the magnetic wings extends further outside the computational domain and therefore some outside boundary points there are inside the potential hump. At boundary points ahead of

the tether, $x < 0$ (tether is at $(x, y) = (0, 0)$), the 3D calculation seems valid. However at points behind the tether ($x > 0$), the partial absorption of contained electrons by the tether renders the 3D calculation invalid.

To remove the uncertainty associated with the 3D calculation at the top and bottom sides, it is recommended to extend the computational domain so as to include the potential hump in all cases.

Other recommendations include

Better Poisson Solver : The Poisson solver used in this work is SLOR (Successive Line OverRelaxation) method. It is known that SLOR is desirable for a small system (e.g. 20×20). For the faster convergence for a large system such as this work, ADI (Alternating-Direction Implicit) method or Multigrid Method is recommended.

Use of unstructured grid & Particle Splitting/Rearranging : The practical limit of the PIC method used in a PC computer is placed by its memory. In order to allow larger computational regions, unstructured grid and particle splitting/rearranging should be considered. As seen in the cylindrical structured grid in Figure 3-3, a structured grid often requires unnecessarily small cells. Therefore the use of unstructured grid is expected to optimize the mesh size. In a PIC simulation, particles are distributed non-uniformly throughout the region. For the reasonable computational resolution, we need a certain number of particles in a cell. By using a particle splitting/rearranging method, we can optimize the number of particles used in the computation. For example,in a sheath created by a negatively biased wall the electron "superparticle" density is low. To get a better resolution in the sheath, the electron superparticle is splitted while it is in the sheath. The splitted superparticle will rearrange with another splitted superparticle as they exit from the sheath.

Non-magnetic flowing case : We could not obtain a solution in the non-magnetic flowing case. The main feature of this case is the trapped electron. Trapped electrons are required in order to maintain the quasi-neutrality in the region.

Apparently the plasma oscillation observed in the simulation is numerical. The real mechanism of trapped electron is still unknown. It is recommended that this case is studied more carefully with much larger grid system, since the particle-field interaction which would trap electrons is considered to happen at long wavelengths as the electron temperature is as low as the field potential. For the investigation of the origin of trapped particles, energy conserving mover may be a better choice.

Different geometry and plasma environment : An ED Tether will be put in practice in space in a various situation. In order to investigate such a variation, more comprehensive comparison cases should be worked on. One case which is missing in this work is on the effects of a magnetic field non-perpendicular to the tether. Different tether shapes and/or multiple tethers are also interesting cases.

Appendix A

Mott-Smith & Langmuir (1926)

The conservation of energy and the angular momentum equation are given as

$$\frac{1}{2}m(u_r^2 + v_r^2) = \frac{1}{2}m(u^2 + v^2) + eV \tag{A.1}$$

$$rv_r = av \tag{A.2}$$

where the probe potential V is taken to be positive for an attractive probe with respect to the sheath edge ($r = a$). Solving these equations, we obtain u_r^2 and v_r, velocity components at the surface of the probe,

$$u_r^2 = u^2 - \left(\frac{a^2}{r^2} - 1\right) v^2 + 2\frac{e}{m}V \tag{A.3}$$

$$v_r = \frac{a}{r}v \tag{A.4}$$

Only those ions will be able to reach the collector for which[1]

$$u > 0 \tag{A.5}$$

$$u_r^2 > 0 \tag{A.6}$$

[1]The condition $u > 0$ has to be satisfied not only at the sheath edge and the probe surface, but also everywhere in the region between.

Therefore the current collection is expressible as

$$i = 2\pi alNe \int_{0 \text{ or } u_1}^{\infty} \int_{-v_1}^{v_1} uf(u,v)\, dv\, du \tag{A.7}$$

where the range of integral is defined by equations (A.3) and (A.4) and $f(u,v)$ is the velocity distribution function at infinity. The point to be remarked is that the integral (A.7) is performed at the edge of sheath ($r = a$). That is why the term $2\pi a$ appears in the right-hand-side of equation. Then the assumption that the velocity distribution function is uniform and independent of its position when the plasma is unperturbed, i.e. in the absense of a probe, enable us to use the velocity distribution function at infinity, which is the same as at $r = a$, in the integral (A.7).The limits, v_1, is found by solving the equation $u_r^2 = 0$ from equation (A.3) for v, namely

$$v_1^2 = \frac{r^2}{a^2 - r^2}\left(u^2 + 2\frac{e}{m}V\right) \tag{A.8}$$

In order to take into account the presheath region which practically extends to infinity, we take the limit of $a \to \infty$.

$$\begin{aligned} i_\infty &= \lim_{a\to\infty} i \\ &= \lim_{a\to\infty} 2\pi alNe \int_{0 \text{ or } u_1}^{\infty} \int_{-v_1}^{v_1} uf(u,v)\, dv\, du \end{aligned} \tag{A.9}$$

The straightforward calculation of the limit is

$$\begin{aligned} i_\infty &= \lim_{a\to\infty, v_1\to 0} 2\pi lNe \frac{\int_{0 \text{ or } u_1}^{\infty} \int_{-v_1}^{v_1} uf(u,v)\, dv\, du}{1/a} \\ &\to \frac{0}{0} \end{aligned} \tag{A.10}$$

Thus we need to use the rule of D'Hopital

$$\lim \frac{f(x)}{g(x)} = \lim \frac{f'(x)}{g'(x)} \tag{A.11}$$

and the identity of derivative,

$$\frac{d}{dx}\int_{h(x)}^{g(x)} f(x,y)dy = g'(x)f(x,g(x)) - h'(x)f(x,h(x)) + \int_{h(x)}^{g(x)} \frac{\partial}{\partial x} f(x,y)dy \quad \text{(A.12)}$$

Then equation (A.9) becomes

$$\begin{aligned} i_\infty &= \lim_{a\to\infty} 2\pi lNe \frac{\int_{0\ or\ u_1}^{\infty} 2uf(u,v)\frac{dv_1}{da}du}{-1/a^2} \\ &= \lim_{a\to\infty} 2\pi lNea^2 \int_{0\ or\ u_1}^{\infty} -2uf(u,v)\frac{dv_1}{da}du \end{aligned} \quad \text{(A.13)}$$

which is the same as equation (between (9) and (10)) in the paper of Langmuir and Mott-Smith (but there is a typo in their paper). Taking the derivative of v_1 with respect to a

$$\frac{dv_1}{da} = \frac{d}{da}\sqrt{\frac{r^2(u^2+2\frac{e}{m}V)}{a^2-r^2}} = \sqrt{r^2(u^2+2\frac{e}{m}V)}\frac{-a}{(a^2-r^2)^{3/2}} \quad \text{(A.14)}$$

and taking into account that $v_1 \to 0$ as $a \to \infty$, we can proceed to the limit,

$$\begin{aligned} i_\infty &= \lim_{a\to\infty} 2\pi lNer\frac{a^3}{(a^2-r^2)^{3/2}} \int_{0\ or\ u_1}^{\infty} 2uf(u,v_1(a))\sqrt{u^2+2\frac{e}{m}V}du \\ &= 4\pi rlNe \int_{0\ or\ u_1}^{\infty} u\sqrt{u^2+2\frac{e}{m}V}f(u,0)du \end{aligned} \quad \text{(A.15)}$$

This is the general form of current collection to a cylindrical probe.

Maxwellian distribution of velocities

If T is the temperature of the distribution and κ is Boltzmann's constant, then the distribution function for the velocity components, u, v is

$$f(u,v) = \frac{m}{2\pi\kappa T}\exp(-\frac{m(u^2+v^2)}{2\kappa T}) \quad \text{(A.16)}$$

Here we define the drift current I as

$$I = Ne \int_0^\infty \int_{-\infty}^\infty u f(u,v) dv\, du = Ne\sqrt{\frac{\kappa T}{2\pi m}} \tag{A.17}$$

Substituting equation (A.16) into equation (A.15), we have

$$i_\infty = 4\pi l N e r \int_{0 \text{ or } u_1}^\infty u\sqrt{u^2 + 2\frac{e}{m}V}\frac{m}{2\pi\kappa T}e^{-\frac{m}{2\kappa T}(u^2+0)}du \tag{A.18}$$

This calculation is a little cumbersome, thus Langmuir and Mott-Smith substituted instead into equation (A.7) and take the limit of $a \to \infty$. In so doing, they introduced nondimensional variables such as

$$\begin{aligned} \frac{eV}{\kappa T} &= \eta \\ u\sqrt{\frac{m}{2\kappa T}} &= x \\ v\sqrt{\frac{m}{2\kappa T}} &= y \end{aligned} \tag{A.19}$$

Substituting equations (A.16) and (A.19) into equation (A.7), we obtain

$$i = 8\sqrt{\pi} a l I \int_{0 \text{ or } \sqrt{-\eta}}^\infty \int_0^{r\sqrt{\frac{x^2+\eta}{a^2-r^2}}} x e^{-(x^2+y^2)} dy\, dx \tag{A.20}$$

where

$$v_1\sqrt{\frac{m}{2\kappa T}} = r\sqrt{\frac{x^2+\eta}{a^2-r^2}}$$

An integration by parts reduces to

$$\begin{aligned}
&\int_{0 \text{ or } \sqrt{-\eta}}^{\infty} \int_0^{r\sqrt{\frac{x^2+\eta}{a^2-r^2}}} x e^{-(x^2+y^2)} dy\, dx \\
&= \int_{0 \text{ or } \sqrt{-\eta}}^{\infty} x e^{-x^2} \int_0^{r\sqrt{\frac{x^2+\eta}{a^2-r^2}}} e^{-y^2} dy\, dx \\
&= \left[-\frac{e^{-x^2}}{2} \int_0^{r\sqrt{\frac{x^2+\eta}{a^2-r^2}}} e^{-y^2} dy \right]_{0 \text{ or } \sqrt{-\eta}}^{\infty} + \int_{0 \text{ or } \sqrt{-\eta}}^{\infty} \frac{e^{-x^2}}{2} \frac{r}{\sqrt{a^2-r^2}} \frac{x}{\sqrt{x^2+\eta}} \exp\left(\frac{r^2(x^2+\eta)}{a^2-r^2} \right) dx \\
&= \underbrace{\left[-\frac{e^{-x^2}}{2} \int_0^{r\sqrt{\frac{x^2+\eta}{a^2-r^2}}} e^{-y^2} dy \right]_{0 \text{ or } \sqrt{-\eta}}^{\infty}}_{I} + \underbrace{\frac{r e^{-\frac{r^2\eta}{a^2-r^2}}}{2\sqrt{a^2-r^2}} \int_0^{\infty} \frac{x}{\sqrt{x^2+\eta}} \exp\left\{ -\frac{x^2 a^2}{a^2-r^2} \right\} dx}_{II} \qquad \text{(A.21)}
\end{aligned}$$

When $\eta > 0$,

$$\begin{aligned}
I &= \frac{1}{2} \int_0^{\sqrt{\frac{r^2\eta}{a^2-r^2}}} e^{-y^2} dy \\
&= \frac{\sqrt{\pi}}{4} \left[1 - \text{erf} \sqrt{\frac{r^2\eta}{a^2-r^2}} \right] \qquad \text{(A.22)}
\end{aligned}$$

and, when $\eta < 0$, we have $I = 0$. As for II, we make the following substitution,

$$x^2 + \eta = \frac{a^2 - r^2}{a^2} z^2 \qquad \text{(A.23)}$$

Then we have from equation (A.21)

$$II = \frac{r e^{\eta}}{2a} \int_{\sqrt{\frac{a^2\eta}{a^2-r^2}}}^{\infty} e^{-z^2} dz \qquad \text{(A.24)}$$

Substituting equations (A.22) and (A.24) into equation (A.21), we finally obtain

$$\begin{aligned}
I + II &= \frac{1}{2} \int_0^{\sqrt{\frac{r^2\eta}{a^2-r^2}}} e^{-y^2} dy + \frac{r e^{\eta}}{2a} \int_{\frac{r^2\eta}{a^2-r^2}}^{\infty} e^{-z^2} dz \\
&= \frac{r}{a} \left[\frac{\sqrt{\pi} a}{4r} \left\{ 1 - \text{erf} \left(\sqrt{\frac{r^2\eta}{a^2-r^2}} \right) \right\} + \frac{\sqrt{\pi}}{4} e^{\eta} \text{erfc} \left(\sqrt{\frac{a^2\eta}{a^2-r^2}} \right) \right] \qquad \text{(A.25)}
\end{aligned}$$

From equations (A.20), (A.21) and (A.25), we have

$$i = 2\pi lIr\left[\frac{q}{r}\left\{1 - \mathtt{erf}\left(\sqrt{\frac{r^2\eta}{a^2 - r^2}}\right)\right\} + e^{\eta}\mathtt{erfc}\left(\sqrt{\frac{r^2\eta}{a^2 - r^2}}\right)\right] \tag{A.26}$$

Since

$$\lim_{a\to\infty} \frac{1 - \mathtt{erf}\left(\sqrt{\frac{r^2\eta}{a^2 - r^2}}\right)}{1/a} = \frac{2r}{\sqrt{\pi}}\sqrt{\eta} \tag{A.27}$$

, we have

$$i_{\infty} = 2\pi rlI\left\{\frac{2}{\sqrt{\pi}}\sqrt{\eta} + e^{\eta}\mathtt{erfc}(\sqrt{\eta})\right\} \tag{A.28}$$

When $\eta \gg 1$, $e^{\eta}\mathrm{erfc}(\sqrt{\eta}) \to 0$. The collected current density, after dividing equation (A.28) by unit area, $2\pi rl$, is obtained as

$$i_{\infty} = 2I\sqrt{\frac{\eta}{\pi}} \tag{A.29}$$

$$= \frac{Ne}{\pi}\sqrt{\frac{2eV}{m}} \tag{A.30}$$

which is indeed the same as equation (2.8).

Appendix B

Time-averaged Outside Boundary Conditions

Since our model is electrostatic and solves potential field by Poisson's equation, any large noise at a computational boundary propagates everywhere at an infinite velocity. This large non-physical fluctuation of potential field throughout the domain brings about unreal total energy gains/losses of particles. This is a very critical issue in our model since we categorize electrons as "trapped" and "non-trapped" depending on the sign of total energy.

Now the question may be stated ;how large the noise can be? In an electrostatic plasma, plasma can shield out the potential difference up to its thermal energy, κT_e. Therefore as long as the potential noises at outside boundary are less than $\kappa T_e/q$, we may exclude the non-physical potential wave propagation throughout the domain.

In our model, an outside boundary potential is determined by solving the quasi-neutrality condition. In the first order approximation, it is given as

$$n_e^{in} + n_e^{out} = \frac{n_\infty}{\sqrt{1 - \frac{2q\phi}{m_i U^2}}} \tag{B.1}$$

$$\sim n_\infty (1 + \frac{q\phi}{m_i U^2}) \tag{B.2}$$

This shows that a potential noise as large as $\kappa T_e/q$ corresponds to a density noise,

$n_\infty \frac{\kappa T_e}{m_i U^2} \sim 0.01 \times n_\infty$. In order to keep the potential noise within $\frac{\kappa T_e}{m_i U^2}$, the density noise should be within the error of 1%. In the following, I show how many particles are necessary in order to estimate a distribution function within a 1% error [15].

Suppose we have a collection of N sampled particles with an unknown distribution function $f(w)$. Our concern is with the precision of the distribution function which we rebuild from the sampled particles. This precision may be expressed in terms of a standard deviation of the distribution function. The probability that a subset of n particles has velocity w and the $N-n$ remaining does not have velocity w is

$$\binom{N}{n} f^n(w) \left(1 - f(w)\right)^{N-n} \tag{B.3}$$

where the distribution function $f(w)$ has been normalized so that it gives a probability of getting a velocity w, and $\binom{N}{n} = N!/(N-n)!n!$. This should be the case of whatever $f(w)$ is. The result is simply dependent on the value of $f(w)$. The average of this probability function is $Nf(w)$ and the standard deviation is

$$\sqrt{Nf(w)\left(1 - f(w)\right)} \tag{B.4}$$

Out of N particles we choose, on average $Nf(w)$ of these particles have velocity w with a standard deviation $\sqrt{Nf(w)(1-f(w))}$. That is, the fractional number of particles with velocity w is on average $f(w)$ with a standard deviation

$$\sigma = \sqrt{f(w)\left(1 - f(w)\right)/N} \tag{B.5}$$

The standard deviation σ is the worst when $f(w) = 0.5$. So we can consider it as a worst case. Now how many particles must we choose so that the fractional number of particles is less than 1% of the distribution function $f(w)$? It is simply the solution to

$$\sqrt{f(w)\left(1 - f(w)\right)/N} = 0.01 \tag{B.6}$$

with $f(w) = 0.5$. The answer is $N = 2500$ Therefore, we need to sample at least 2500

particles in order to calculate the outgoing particle density with an error of 1%.

In computation, this number is prohibitedly large. Assuming that one timestep is equal to $0.01/\omega_p$, the number of super-particles going through an outside boundary cell with a dimension of $0.5d_D$ is given as

$$\underbrace{\frac{n_\infty}{4}\sqrt{\frac{8\kappa T_e}{\pi m_e}}}_{\text{Electron Flux}} \times \underbrace{\frac{d_D}{2}}_{\text{Cell Size}} \times \underbrace{\frac{0.01}{\omega_p}}_{\text{Time Step}} \times \underbrace{\frac{1}{N_p}}_{\text{Super-Particle}} \sim 0.1 \tag{B.7}$$

where parameters are taken from Tables 3.1 and 3.2. Therefore, to sample 2,500 particles at each boundary cell, it is required to sample them over 25,000 iterations for $\Delta t = 0.01/\omega_p$. This is still a very large number considering that an average number of iteration for one day is about 2,000. Moreover, the same calculation about outgoing ions leads to 2,500,000 iterations. For now, we use an outgoing electron density averaged over 10,000 iterations and ion density over the unlimited number of time steps. The yet-noisy results are smoothed by Savitzky-Golay Smoothing Filter [16]. When we have an access to a super-computer or a parallel computation with faster CPU's with more memory is available, we shall be readily able to eliminate this averaging process.

Bibliography

[1] M.L.Cosmo and E.C.Lorenzini Tethers In Space Handbook, Third Edition December 1997

[2] Cooke, D. L., and I. Katz, *TSS-1R electron currents: Magnetic limited collection from a heated presheath*, Geo. Res. Let., Vol. 25, No. 5, Pages 753-756, March 1, 1998

[3] Irwin E. Vas, Thomas J. Kelly and Ethan A. Scarl *Space Station Reboost with Electrodynamic Tethers* Journal of Spacecraft and Rockets Vol 37, No2, March-April 2000

[4] Katz, I., et al., *Observation of ionospheric heating in the TSS-1 subsatellite presheath*, J. Geophys. Res., 99, 8961-8969, 1994

[5] Hastings, D. and Garrett, H. *Spacecraft-Environment Interactions*, Cambridge University Press, 1996.

[6] Martínez-Sánchez, M. and Hastings, D. E., *A Systems Study of a 100 kW Tether*, Journal of the Astrinautical Sciences, Vol.35, No.1, pp.75-96, 1987.

[7] J. R. Sanmartín and M. Martínez-Sánchez, *The radiation impedance of orbiting conductors* Journal of Geo. Research, Vol.100, No.A2, 1677-1686, Feb. 1, 1995

[8] J. R. Sanmartín, M. Martínez-Sánchez and E. Ahedo, *Bare Wire Anodes for Electrodynamic Tethers* Journal of Propulsion and Power, Vol.9, No.3, May-June, 353-360, 1993

[9] J. R. Sanmartín, private communication, 2002

[10] S. Langmuir and H. Mott-Smith, *The theory of collection in gaseous discharge* Physical Review, 28, Oct. 1926

[11] H. Goldstein, *Classical Mechanics*, Addison-Wesley Pub. Co., Massachusetts, 1980.

[12] R.D.Estes, J.Sanmartín and M. Martín-Sánchez, *Performance of Bare-Tether Systems Under Varying Magnetic and Plasma Conditions*, Journal of Spacecraft and Rockets, Vol.37, No.2, March-April 2000

[13] J.R.Sanmartín and R.D.Estes, *The orbital-motion-limited regime of cylindrical Langmuir probes*, Physics of Plasmas, Vol. 6, No. 1, Jan. 1999

[14] J. Sanmartín, *The theory fo a probe in a strong magnetic field*, Physics of Fluids 13 103 1970

[15] R. Garner, private communication, 2001.

[16] Numerical Recipes, Chap.14

[17] Numerical Recipes, Chap.7

[18] Laframboise,J. G., Theory of spherical and cylindrical Langmuir probes in a collisionless, Maxwellian plasma at rest, *Rep. 100*, Inst. for Aerosp. Stud., Univ. of Toronto, Toronto, Ontario, Canada, 1966

[19] Laframboise,J. G. and L. W. Parker, *Probe design for orbit-limited current collection*, Phys. Fluids, 16, 629, 1973

[20] Singh, Nagendra, W.C.Leung and B.I.Vashi, *Potential structure near a probe in a flowing magnetoplasma and current collection*, Journal of Geophysical Research, Vol.102, No.A1, Page 195-208, Jan. 1997

[21] Laframboise, J.G. and L. J. Sonmor, *Current Collection by Probes and Electrodes in Space Magnetoplasmas: A Review*, Journal of Geophysical Research, Vol.98, No.A1, Page 337-357, Jan. 1993

[22] Laframboise, J.G., *Current Collection by a positively charged spacecraft: Effects of its magnetic presheath*, Journal of Geophysical Research, Vol.102, No.A2, Page 2417-2432, Feb. 1, 1997

[23] Szuszczewics, E. P., *Controlled electron beam experiments in space and supporting laboratory experiments: a review*, Journal of Atmospheric and Terrestrial Physics, Vol.47, No. 12, Page 1189-1210, 1985.

[24] Parker, L. W., and B. L. Murphy, *Potential buildup on an electron-emitting ionospheric satellite*, J. Geophys. Res., 72, 1631, 1967

[25] Makita, H. and K. Kuriki, *Comparative study of spherical and sylindrical drift probes*, Paper 33 at the 10th International Symposium on Rarefied Gas Dynmaics Aspen Colo July 19-23 1976

[26] Makita, H. and K. Kuriki, *Current Collection by spherical Langmuir probes drifting in a collisionless plasma*, Physics of Fluids 21(8), Page 1279-1286, August 1978

[27] Godard, R., *Systematical Model for cylindrical and spherical collectors in a Flowing Collisionless Plasma* Ph.D. Thesis, York Uninversity, Toronto, Ontario, 1975

[28] Godard, R. and J. G. Laframboise, *Total Current To Cylindrical Collectors In Collisionless Plasma Flow*, Planet. Space Sci., Vol. 31, No. 3, Page 275-283, 1983

[29] Gilchrist, B. E. and S. G. Bilén, *Bare Electrodynamic Tether Ground Simulations in a Dense, High-Speed Plasma Flow*, AIAA 2000-3869, 2000

[30] Laframboise, J. G., and J. Rubinstein, *Theory of a cylindrical probe in a collisionless magnetoplasma*, Phys. Fluids, 19, 1900, 1976

[31] Martínez-Sánchez, private communication, 2001.

[32] Johnson, L. et al., *Propulsive Small Expendable Deployer System Experiment*, Journal of Spacecraft and Rockets, Vol.37, No.2, Page173-176, March-April 2000.

[33] Onishi, T., Electron Current Collection by a Positively Charged Tether Using a Particle-In-Cell Method, Master Thesis, *SERC #4-98*, MIT, Cambridge, Mass., 1998

[34] Onishi, T., M. Martínez-Sánchez and D. L. Cooke, Computation of Current to a Moving Bare Tether, *AIAA 2000-3865*, Huntsville, AL 2000

[35] Sasaki, S. et al., *Tethered Rocket Experiment (CHARGE-2): Initial Results on Electrodynamics*, Radio Sci., 23, 975, 1988

[36] Birdsall, C. K. and A. B. Langdon, *Plasma physics via computer simulation*, Institute of Physics Publishing, Briston and Philadelphia, 1991

[37] Usui, H., Study on the Electrodynamic Interaction Between a Tethered Satellite System and Space Plasma, Ph.D. Thesis, Kyoto Univ. Dec. 1993

[38] Rubinstein, J., and J. G. Laframboise, *Upper-bound current to a cylindrical probe in a collisionless magnetoplasma*, Phys. Fluids, 21, 1655, 1978

[39] Rubinstein, J., and J. G. Laframboise, *Theory of a spherical probe in a collisionless magnetoplasma*, Phys. Fluids, 25, 1174, 1982

[40] Roussel, J.-F., *Modelling of Spacecraft Plasma Environment Interactions*, 7^{th} Spacecraft Charging Technology Conference, Noordwijk, The Netherlands, April 23-27, 2001

5000